Long-distance effects in rare B decays

Dissertation
zur
Erlangung des Doktorgrades (Dr. rer. nat.)
der
Mathematisch-Naturwissenschaftlichen Fakultät
der
Rheinischen Friedrich-Wilhelms-Universität Bonn

vorgelegt von
Stephan Kürten
aus
Bonn

Bonn 2026

Angefertigt mit Genehmigung der Mathematisch-Naturwissenschaftlichen Fakultät der Rheinischen Friedrich-Wilhelms-Universität Bonn

Gutachter/Betreuer:	PD. Dr. Bastian Kubis
Gutachter:	Dr. Danny van Dyk
Tag der Promotion:	11.05.2026
Erscheinungsjahr:	2026

Abstract

The physics underlying the change of quark flavor provides important constraints on physics beyond our current best understanding. These indirect searches for signs of New Physics require the comparison of high-precision predictions with high-precision measurements. In this work, I refine two types of hadronic matrix elements, which are essential ingredients for these indirect searches. My work is grounded in methods that respect the analyticity and unitarity properties of these matrix elements.

After an overview about the used foundations, the first project applies dispersion relations to a set of $B \to \gamma^*$ form factors used in $B^- \to \ell^- \bar{\nu}_\ell \ell'^- \ell'^+$decays. By that, the form factors are related to well-known $B \to V$ form factors exploiting a vector meson dominance model in the isospin contributions for $I = 0$ and $I = 1$. The form factors are defined such that they avoid kinematic singularities by the use of the Bardeen–Tung–Tarrach procedure, which is modified to be applicable to massive gauge bosons instead of photons. Following that, a discussion with recent literature is given. At last, the formalism is subtracted once to match the subtraction constant to measurements and, thus, improve on the predictive abilities of the method.

The second project analyzes $e^+e^- \to$ open charm data in the vicinity of the $\psi(3770)$ resonance, using a fully analytic K-matrix formalism. For that, the phase space parametrization is analytically continued enabling an evaluation of the S-matrix poles on the second Riemann sheet. The pole parameters are used to extract the mass and width of the $\psi(3770)$ resonance and to compute cross section in the analyzed energy region. The results are discussed in comparison to recent literature, where discrepancies to prevailing opinions in the field are found.

Contents

CHAPTER 1

Introduction

The desire to know where our world has started is the everlasting quest of humankind. By observing nature the idea arises that everything might be built from smaller, simpler building blocks. This fundamental idea gives rise to the field of elementary particle physics. The standard model of particle physics (SM) [1–3] is the predominant theory in describing these building blocks of matter, the fermions. The SM classifies fermions in leptons and quarks and describes three out of four forces through which particles are known to interact, mediated by the exchange of bosons. Besides these fermions, the SM gives rise to the force mediators: the gluons mediating the strong, $W^{\pm}$ and Z bosons the weak and photons the electromagnetic interaction. The masses of fermions and mediator particles are explained by the Higgs boson, which was only proposed theoretically [4, 5] until its discovery in 2012 [6, 7]. Although the SM is immensely successful in predicting results of particle physics experiments it is not able to describe several phenomena observed in nature, e.g. it does not include the description of the gravitational force, cannot justify the existence of dark matter and dark energy and is unable to explain the matter-antimatter asymmetry in the universe. Therefore, we know there is physics beyond the standard model (BSM). Common approaches for the search of BSM physics are direct searches in particle collisions at high energies or indirect searches of deviations of the SM predictions at lower energies with ever higher precision in experiments and theory. B-meson decays open access to a variety of final states at energies below the B-meson mass and allow to investigate transitions between the different quarks and leptons, giving rise to the field of flavor physics.

The B meson is the simplest bound state of a b quark and a lighter quark. It is highly accessible in various experiments, e.g. the LHC experiments (LHCb, CMS and ATLAS) as well as the B-factories Belle and BaBar.

In this thesis, we investigate novel approaches to describe purely hadronic effects in B decays, based on analyticity and unitarity, to further raise the precision of BSM analyses based on B-decay data. The results of this thesis are partially published in [8, 9]. The radiative leptonic decay $B^- \to \ell^- \bar{\nu}_\ell \gamma$ is of significant interest [10–12], as it provides access to the leading-twist B-decay light-cone distribution amplitude (LCDA), which serves as valuable hadronic input to several exclusive B decays. Measurements of this decay are predominantly conducted at the Belle II

experiment and less feasible at the LHC experiments, particularly the LHCb experiment. However, the decay $B^- \to \ell^- \bar{\nu}_\ell \ell'^- \ell'^+$ is excellently measurable at both the Belle II and LHCb experiments. To achieve a good description of the $B^- \to \ell^- \bar{\nu}_\ell \ell'^- \ell'^+$ decay, a model of the $B \to \gamma^*$ form factors is crucial and studied in the recent literature [13–16]. In Ch. 3 we model a set of form factors that is consistent with analyticity and unitarity and point out inconsistencies in previous literature.

Furthermore, we analyze data on $e^+e^- \to$ open charm in the region of the $\psi(3770)$ resonance, using a fully-analytic coupled-channel K-matrix approach. Full knowledge of the complete $e^+e^- \to$ open charm spectrum is desirably as crucial input for rare B decays, e.g. $B \to K^* \ell\ell$. By analytic continuation of the phase space factors occurring in the K-matrix model we include the analytic properties of the involved scattering amplitudes. Using several models fitted to the full dataset we use a statistical comparison to identify our nominal fit with the resonance parameters $M_{\psi(3770)} = 3778.8 \pm 0.3\,\text{MeV}$ and $\Gamma_{\psi(3770)} = 25.0 \pm 0.5\,\text{MeV}$. Additionally, we confirm that the decays to D^+D^- and $D^0\bar{D}^0$ are consistent with isospin symmetry, while also providing an upper bound on the branching ratio $\mathcal{B}(\psi(3770) \to \text{non-}D\bar{D}) < 6\%$ at 90% probability.

The outline of this thesis is as follows: in Ch. 2 we focus on the fundamentals used throughout this thesis. After a short introduction to the relation between SM and the discipline of flavor physics we discuss the scattering of two particles and provide introductions to the methods of complex analyticity used within.

In Ch. 3 we discuss the weak effective Lagrangian this project is based on. After deriving the decomposition of the hadronic tensor, we describe how to modify the Bardeen–Tung–Tarrach procedure to apply the procedure to $B^- \to \ell^- \bar{\nu}_\ell \ell'^- \ell'^+$decays. Moreover, details on the applications of the formalism are provided. Some details on the estimation of uncertainties and on the usage of a once-subtracted dispersion relation within the developed formalism is discussed.

In Ch. 4 we provide a detailed introduction to the K-matrix formalism and describe how to extract the physical properties from the K-matrix. The used data and the applied analysis is discussed. The results of this K-matrix analysis are illustrated and possible future improvements are pointed out. How the results can be related to non-local form factors in $b \to s\ell^+\ell^-$ transitions is sketched.

After summarizing the main part of this thesis in Ch. 5 we provide additional details on the kinematics and the computation of the amplitude in $B^- \to \ell^- \bar{\nu}_\ell \ell'^- \ell'^+$decays in the appendix.

CHAPTER 2

Foundations and reviews

In this chapter we give a short review of the standard model (SM) of particle physics. In the history of physics, the SM has been one of the most successful theories. A full review on this theory is far beyond the scope of this thesis, so we point the interested reader to the standard textbooks, e.g. Refs. [17–19]. Here and in the following, we focus on the parts relevant for this work and give an explicit introduction to the topic in the next sections.

2.1 Standard model of particle physics

As a renormalizable quantum field theory, the SM of particle physics is established in a local gauge symmetry under the gauge group

$$SU(3)_C \times SU(2)_L \times U(1)_Y. \tag{2.1}$$

More explicitly, $SU(3)_C$ is the symmetry group of the strong interactions and $SU(2)_L \times U(1)_Y$ is the electroweak symmetry group. The electroweak symmetry group is spontaneously broken by the non-vanishing vacuum expectation value (VEV) of the Higgs boson according to

$$SU(2)_L \times U(1)_Y \to U(1)_Q, \tag{2.2}$$

where Q is the electric charge, which is related to the hypercharge Y and third component of the weak isospin I_3 via the Gell-Mann–Nishijima formula

$$Q = I_3 + \frac{Y}{2}. \tag{2.3}$$

Since the special unitary and unitary groups are Lie groups, they follow a Lie algebra. In case of $SU(N)$, the related Lie algebra is of dimension $N^2 - 1$ and in case of $U(N)$ the dimension of the Lie algebra is N^2. In a local gauge theory, the gauge bosons correspond to the generators of the group. Hence, $SU(3)_C$ includes 8 gluons, $SU(2)_L$ has 3 gauge fields and $U(1)_Y$ has a single gauge field. The fields and their representations in each symmetry group are listed in Table 2.1.

The widely adopted minimal ansatz for a Lagrangian density that incorporates the spontaneous breaking of $SU(2)_L \times U(1)_Y \to U(1)_Q$ is

$$\begin{aligned}\mathcal{L}_{SM} &= i\sum_{\psi}\bar{\psi}\not{D}\psi - \frac{1}{4}\left(W^a_{\mu\nu}W^{\mu\nu}_a + B_{\mu\nu}B^{\mu\nu} + G^b_{\mu\nu}G^{\mu\nu}_b\right)\\ &+ \left(D^\mu H\right)^\dagger\left(D_\mu H\right) - V(H) - \left(\bar{\psi}_L Y H \psi_R + h.c.\right),\end{aligned} \tag{2.4}$$

where ψ is summed over all fermionic fields, $W^a_{\mu\nu}$, $B_{\mu\nu}$ and $G^b_{\mu\nu}$ are fields of the 3 gauge groups, H is the scalar Higgs field and the last term is the Yukawa part, which couples scalar and fermionic fields, along with their respective hypercharge assignments. The fields of the gauge symmetry groups are defined as

$$\begin{aligned}B_{\mu\nu} &= \partial_\mu B_\nu - \partial_\nu B_\mu\,,\\ W^a_{\mu\nu} &= \partial_\mu W^a_\nu - \partial_\nu W^a_\mu - \mathrm{i}g_2\epsilon^{abc}W^b_\mu W^c_\nu\,,\\ G^b_{\mu\nu} &= \partial_\mu G^b_\nu - \partial_\nu G^b_\mu - \mathrm{i}g_s f^{bac}W^a_\mu W^c_\nu\end{aligned} \tag{2.5}$$

with the structure constants ϵ^{abc} of $SU(2)$ and f^{bac} of $SU(3)$. The covariant derivative used is

$$D_\mu = \partial_\mu - \mathrm{i}g_1 Y B_\mu - ig_2\frac{\sigma^a}{2}W^a_\mu - ig_s\frac{\lambda^b}{2}G^b_\mu, \tag{2.6}$$

where σ^a are the Pauli matrices and λ^b the Gell-Mann matrices and g_i are the couplings to the respective symmetry group. The electron charge is given in terms of these couplings as

$$e = \frac{g_1 g_2}{\sqrt{g_1^2 + g_2^2}}. \tag{2.7}$$

Furthermore, one can define the electromagnetic and strong couplings as

$$\alpha_e := \frac{e^2}{4\pi}, \qquad \alpha_s = \frac{g_s^2}{4\pi}, \tag{2.8}$$

where α_e is also known as the *fine-structure constant*. In contrast to the other fields in the SM, as a scalar field, the kinematic terms of the Higgs field in Eq. (2.4) and its potential

$$V(H) = -\mu^2 H^\dagger H + \lambda\left(H^\dagger H\right)^2 \tag{2.9}$$

break the electroweak gauge symmetry group spontaneously by means of its non-vanishing vacuum expectation value

$$\langle H\rangle = \frac{1}{\sqrt{2}}\begin{pmatrix}0\\ v\end{pmatrix}. \tag{2.10}$$

Field	$SU(3)_C$	$SU(2)_L$	Y
B_μ	1	1	0
W^a_μ	1	3	0
G^b_μ	8	1	0
$Q^i_L = (u^i_L, d^i_L)$	3	2	+1/3
$E^i_L = (\nu^i_L, e^i_L)$	1	2	-1
u^i_R	3	1	4/3
d^i_R	3	1	−2/3
e^i_R	1	1	−2
H	1	2	1

Table 2.1: The SM fields and their representations in the respective gauge group. Y is the hypercharge of the field. Q^i_L and E^i_L denote the $SU(2)_L$ doublets of left handed quarks and leptons, respectively. The i denote the family indices of the matter fields.

Due to the symmetry breaking four, gauge bosons are generated, which are two massive charged W bosons, one massive neutral Z boson and one massless photon. Moreover, the SM contains six types of quarks: up (u), down (d), strange (s), charm (c), bottom (b) and top (t); as well as three types of leptons: electron (e), muon (μ) and tau (τ), accompanied by the respective neutrinos (ν_e, ν_μ, ν_τ). The SM, more specifically the weak interaction, differentiates between left-handed and right-handed particles. It couples right-handed particles and left-handed anti-particles only if they are massive. Thus, there are no right-handed neutrinos included, as neutrinos are assumed to be massless in the SM, cf. Table 2.1.

So far, the above are the fundamentals of the SM. The particles associated with the Lagrangian and its symmetries are described but by far not every aspect that can be observed is explained yet. One major point is lacking explanation, for the fact that different types of particles have different masses by orders of magnitudes.[1] Usually, the particles are ordered by their masses, which results in 3 different *families* of particles. The representation of the SM Lagrangian in Eq. (2.4) is in a basis that is diagonal in the fermionic fields and thus does not mix any types of fermions. Since fermions are physical particles, it is convenient to change into a representation, where fermions are mass eigenstates, the so-called *mass basis*. For convenience, we outline the procedure for orthogonalizing the quark fields in the scenario involving only up and down flavors. Additionally,

[1] Moreover, the SM does not include gravity as an interaction and can not explain dark matter effects, both of which are not part of this thesis.

disregarding the lepton flavor, the Yukawa component of the Standard Model Lagrangian Eq. (2.4) is expressed as follows:

$$\begin{aligned}\mathcal{L}_{SM} &\supset \bar{u}_L Y_u \frac{v}{\sqrt{2}} u_R + \bar{d}_L Y_d \frac{v}{\sqrt{2}} d_R \\ &\equiv \bar{u}_L M_u u_R + \bar{d}_L M_d d_R \,,\end{aligned} \tag{2.11}$$

where we used the Higgs VEV Eq. (2.10) and associated $Y_q \frac{v}{\sqrt{2}}$ with a 3×3 quark mass matrix. The mass matrices M_u and M_d can always be diagonalized by performing a biunitary transformation of the quark fields

$$u_R \to U_u u_R, \quad d_R \to U_d d_R, \quad \bar{u}_L \to \bar{u}_L U_u^\dagger, \quad \bar{d}_L \to \bar{d}_L U_d^\dagger \,, \tag{2.12}$$

such that the matrices can be written in the form

$$U_{qL}^\dagger M_q U_{qR} = M_q^{\text{diag}} \,. \tag{2.13}$$

Consequently, the rotation operators define the *Cabibbo–Kobayashi–Maskawa* (CKM) matrix as

$$U_u^\dagger U_d \equiv V_{CKM} = \begin{pmatrix} V_{ud} & V_{us} & V_{ub} \\ V_{cd} & V_{cs} & V_{cb} \\ V_{td} & V_{ts} & V_{tb} \end{pmatrix}, \tag{2.14}$$

which is a unitary complex matrix with *a priori* nine degrees of freedom. In fact, there is a parameterization introduced by Wolfenstein [20], which leaves the CKM matrix with four real parameters

$$\lambda \simeq 0.23, \quad A \simeq 0.8, \quad \rho \simeq 0.1, \quad \eta \simeq 0.3 \,, \tag{2.15}$$

where the parameters ρ and η are related to a complex phase CP-violating phase. Expanded up to order λ^3, the Wolfenstein parametrization reads

$$V_{CKM} = \begin{pmatrix} 1 - \frac{1}{2}\lambda^2 & \lambda & A\lambda^3(\rho - \mathrm{i}\eta) \\ -\lambda & 1 - \frac{1}{2}\lambda^2 & A\lambda^2 \\ A\lambda^3(1 - \rho - \mathrm{i}\eta) & -A\lambda^2 & 1 \end{pmatrix} + O(\lambda^4), \tag{2.16}$$

where one can see that the diagonal entries are almost 1 up to a correction proportional to λ^2. Unitarity of Eq. (2.14) implies the relations

$$\sum_i V_{ij} V_{ik}^* = \delta_{jk}. \tag{2.17}$$

Especially the relation

$$V_{ud} V_{ub}^* + V_{cd} V_{cb}^* + V_{td} V_{tb}^* = 0 \tag{2.18}$$

is of great interest for flavor physics since it is proportional to all the b-quark transitions. The results are summarized and published by the CKM fitter group [21], which regularly shows the

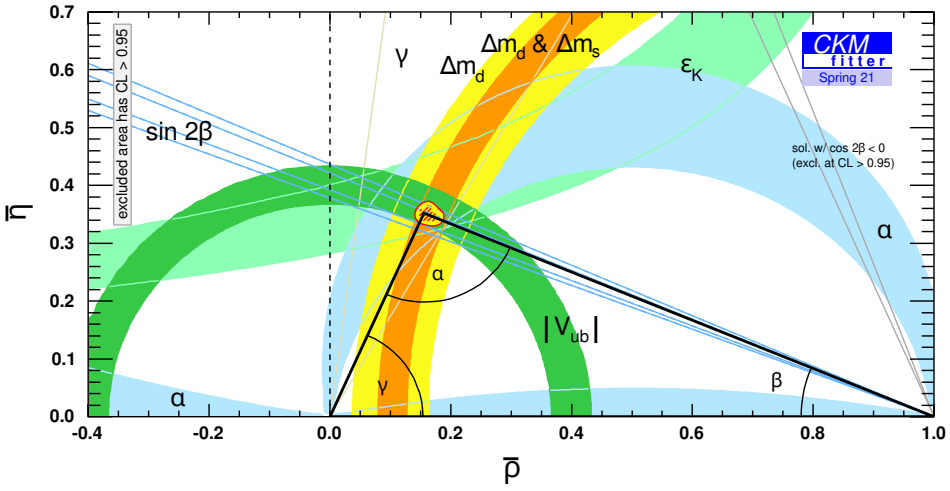

Figure 2.1: Experimental constraints and unitarity triangle in the $\bar{\rho} - \bar{\eta}$ plane. The red hashed region of the global combination corresponds to 68% confidence level [21].

current state of measurements in an unitarity triangle plot Fig. 2.1 in the $\bar{\rho} - \bar{\eta}$ plane, with

$$\bar{\rho} = \rho\left(1 - \frac{\lambda^2}{2}\right), \qquad \bar{\eta} = \eta\left(1 - \frac{\lambda^2}{2}\right), \tag{2.19}$$

where the angles are

$$\alpha := \arg\left[-\frac{V_{td}V_{tb}^*}{V_{ud}V_{ub}^*}\right], \quad \beta := \arg\left[-\frac{V_{cd}V_{cb}^*}{V_{td}V_{tb}^*}\right], \quad \gamma := \arg\left[-\frac{V_{ud}V_{ub}^*}{V_{cd}V_{cb}^*}\right]. \tag{2.20}$$

2.2 Weak effective theory and operator product expansion

Since the electromagnetic and strong interactions conserve flavor, many particles can only decay within weak interactions. A simple and purely leptonic example for such a decay is $\mu \to e\nu_\mu\bar{\nu}_e$, cf. Ref. [22]. At leading order, this decay takes place by only one W boson exchange, cf. Fig. 2.2, its

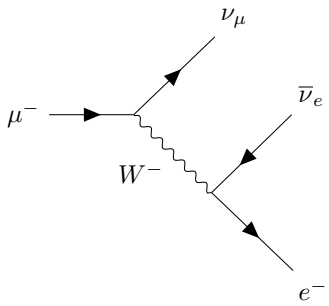

Figure 2.2: Diagram for tree-level muon decay.

amplitude is given by

$$\mathcal{M}(\mu \to e\nu_\mu\bar{\nu}_e) = \left(\frac{g_2}{\sqrt{2}}\right)^2 \left[\bar{u}(p_{\nu_\mu})\gamma_\alpha P_L u(p_\mu)\right]\left[\bar{u}(p_e)\gamma_\beta P_L v(p_{\bar{\nu}_e})\right] \times \frac{g^{\alpha\beta} - \frac{(p_\mu - p_{\nu_\mu})^\alpha (p_\mu - p_{\nu_\mu})^\beta}{M_W^2}}{(p_\mu - p_{\nu_\mu})^2 - M_W^2}, \tag{2.21}$$

where the second line is the W boson propagator in unitary gauge, P_L is the left-handed projector, g_2 is the weak coupling from Eq. (2.4) and p_{ν_μ},p_μ, p_e and $p_{\bar{\nu}_e}$ are the momenta of the muon neutrino, muon, electron and anti-electron neutrino, respectively. The decay of the muon can always be Lorentz transformed in the muon's rest frame. Hence, all interactions take place at energies of the order of the muon mass, meaning that all momenta occuring in Eq. (2.21) are naturally much smaller than the W boson mass, since $m_\mu \ll M_W$. By that, Eq. (2.21) can be simplified, replacing the second line with $-g^{\alpha\beta}/M_W^2$, and gives

$$\mathcal{M}(\mu \to e\nu_\mu\bar{\nu}_e) = -\frac{4G_F}{\sqrt{2}}\left[\bar{u}(p_{\nu_\mu})\gamma_\alpha P_L u(p_\mu)\right]\left[\bar{u}(p_e)\gamma_\alpha P_L v(p_{\bar{\nu}_e})\right], \tag{2.22}$$

where the W boson mass is absorbed in the Fermi constant

$$\frac{G_F}{\sqrt{2}} = \frac{g_2^2}{8M_W^2}. \tag{2.23}$$

The amplitude Eq. (2.22) is also reproduced by computing the matrix element from the effective Hamiltonian

$$\mathcal{H}_W = -\mathcal{L}_W = \frac{4G_F}{\sqrt{2}}\left[\bar{\nu}_\mu\gamma_\alpha P_L\mu\right]\left[\bar{e}\gamma_\alpha P_L\nu_e\right]. \tag{2.24}$$

De facto, we have removed the W boson as a dynamical degree of freedom and, by that, made the weak interaction happening in one spacetime point. Throughout the literature this procedure is also called integrating out the W boson as a heavy degree of freedom from the full theory. An effective

4-fermion interaction is obtained in Eq. (2.24). Thus, we have applied

$$\lim_{x\to y} O_1(x)O_2(y) = \sum_n C_n(x-y)O_n\,, \tag{2.25}$$

where the operators O_1 and O_2 are generalized symbols for currents such as in the square brackets in Eq. (2.24), O_n is the effective 4-fermion vertex obtained by evaluating both currents at the same spacetime point and C_n is called a Wilson coefficient. Similarly, on any scale that is far lower than the W boson mass, it can be integrated out. This is also a good approximation for B-meson decays as used in Ch. 3, since $m_b^2/M_W^2 \approx 1/370 \ll 1$.

2.3 Scattering of two particles in the K-matrix formalism

In quantum field theories every scattering process starts with some particle fields with well defined momenta and quantum numbers. There is some time before any interaction happens and some time when the interaction is in the past. The states before the interaction are called initial states and the states after the interaction are called final states. The S-matrix introduces the concept of — in principle — taking every possible initial and final state into account. In that case, each element of the S-matrix describes the transition amplitude of a certain initial state into a certain final state. The K-matrix is a way to simplify the calculation of S-matrix elements, particularly in the context of resonant scattering. In the following, a particular parametrization of the K-matrix ansatz is introduced, with the derivation based on the description provided in Ref. [23]. In general, the S-matrix is denoted in bra-ket notation as

$$\langle f|\,S\,|i\rangle = \langle f|\,\mathbb{1}\,|i\rangle + 2\mathrm{i}\,\langle f|\,\hat{T}\,|i\rangle\ , \tag{2.26}$$

where the trivial part — without any interaction happening — is separated from the part of actual transitions; the $\hat{T}$-matrix and the factor 2i are conveniently introduced here. Since Eq. (2.26) describes a physical process, the S-matrix oughts to conserve probability, thus fulfilling the relation

$$SS^\dagger = S^\dagger S = \mathbb{1}. \tag{2.27}$$

Using the definition of the S-matrix Eq. (2.26) we can rewrite Eq. (2.27) in terms of only $\hat{T}$,

$$\hat{T} - \hat{T}^\dagger = 2\mathrm{i}\mathrm{Im}(\hat{T}) = 2\mathrm{i}\hat{T}\hat{T}^\dagger = 2\mathrm{i}\hat{T}^\dagger\hat{T}, \tag{2.28}$$

leading directly to the unitarity relation of the transition amplitude

$$\mathrm{Im}(\hat{T}) = \hat{T}\hat{T}^\dagger = \hat{T}^\dagger\hat{T}. \tag{2.29}$$

Multiplying Eq. (2.28) from either side with the inverse operators $\hat{T}^{-1}$ and $(\hat{T}^\dagger)^{-1}$, we obtain

$$(\hat{T}^\dagger)^{-1} - \hat{T}^{-1} = 2\mathrm{i}\mathbb{1}, \tag{2.30}$$

which can be decomposed into

$$(\hat{T}^{-1} + \mathrm{i}\mathbb{1})^{\dagger} = \hat{T}^{-1} + \mathrm{i}\mathbb{1}. \tag{2.31}$$

This can now be identified as the inverse $\hat{K}$-matrix operator

$$\hat{K}^{-1} = \hat{T}^{-1} + \mathrm{i}\mathbb{1}, \tag{2.32}$$

which is a hermitian operator. Further multiplying Eq. (2.32) with $\hat{K}$ and $\hat{T}$ from either side gives

$$\hat{T} = \hat{K} + \mathrm{i}\hat{K}\hat{T} = \hat{K} + \mathrm{i}\hat{T}\hat{K}, \tag{2.33}$$

which also shows that $\hat{K}$ and $\hat{T}$ commute. Solving Eq. (2.33) for $\hat{T}$ gives the amplitude expressed in terms of the $\hat{K}$-matrix,

$$\hat{T} = \hat{K}(\mathbb{1} - \mathrm{i}\hat{K})^{-1} = (\mathbb{1} - \mathrm{i}\hat{K})^{-1}\hat{K}. \tag{2.34}$$

The expression Eq. (2.34) is not yet a Lorentz-invariant amplitude. To render everything Lorentz invariant, one needs to replace the amplitude with its Lorentz-invariant part in Eq. (2.26),

$$\hat{T} \to \sqrt{\rho} T \sqrt{\rho}, \tag{2.35}$$

where T is now the Lorentz-invariant amplitude and ρ is a $n \times n$ matrix,

$$\rho = \begin{pmatrix} \rho_1 & 0 & \dots \\ 0 & \rho_2 & \dots \\ \dots & \dots & \ddots \end{pmatrix}. \tag{2.36}$$

The ρ_i are phase-space factors[2] of each corresponding decay channel and can be modeled by

$$\rho_i(s) = \Theta(s - 4m_i^2)\frac{1}{16\pi}\sqrt{1 - \frac{4m_i^2}{s}}, \tag{2.37}$$

with m_i as the mass of the channel. Using the replacement Eq. (2.35) one obtains from the unitarity of the S-matrix

$$T - T^{\dagger} = 2\mathrm{i}\mathrm{Im}(T) = 2\mathrm{i}T\rho T^{\dagger} = 2\mathrm{i}T^{\dagger}\rho T \tag{2.38}$$

and immediately the Lorentz-invariant unitarity relation

$$\mathrm{Im}(T) = T\rho T^{\dagger} = T^{\dagger}\rho T. \tag{2.39}$$

Defining the Lorentz-invariant K-matrix equivalent to Eq. (2.38),

$$K^{-1} = T^{-1} + \mathrm{i}\rho \tag{2.40}$$

[2] The phase-space factor shown here is purely imaginary above threshold and — as a simplified model — not at all analytic. The analyticity of the phase space can be introduced by replacing $\mathrm{i}\rho$ by the fully complex analytic Chew–Mandelstam functions as introduced in Eq. (2.42).

leads with the same procedure as before to the general ansatz of describing an amplitude in terms of the K-matrix

$$T = K(\mathbb{1} - \mathrm{i}\rho K)^{-1} = (\mathbb{1} - \mathrm{i}K\rho)^{-1}K. \tag{2.41}$$

Since Eq. (2.37) is not an analytic function and is not applicable for particles with different masses, we need to replace the purely imaginary factor $\mathrm{i}\rho$ by an analytic equivalent. One commonly used ansatz are the Mandelstam functions [24, 25], which can be computed as the discontinuity of a self-energy diagram of two particles. For two scalar particles in an S-wave configuration, the Mandelstam function reads

$$\Sigma(s) = \frac{1}{16\pi^2}\left[\frac{2q(s,m_1,m_2)}{\sqrt{s}}\log\left(\frac{m_1^2+m_2^2-s+2\sqrt{s}q(s,m_1,m_2)}{2m_1m_2}\right)\right.$$
$$\left. - (m_1^2-m_2^2)\left(\frac{1}{s}-\frac{1}{(m_1+m_2)^2}\right)\log\left(\frac{m_1}{m_2}\right)\right], \tag{2.42}$$

with

$$q(s,m_1,m_2) = \frac{\lambda^{1/2}(s,m_1^2,m_2^2)}{2\sqrt{s}}. \tag{2.43}$$

Here, the Mandelstam function Eq. (2.42) is equal to $\mathrm{i}\rho$ on the real axis above threshold and $m_1 = m_2$.

2.4 Analytic continuation of the amplitude

The physical amplitude T is a holomorphic function and fulfills the Schwarz reflection principle, i.e.

$$T(s)^* = T(s^*)\,. \tag{2.44}$$

As long as the K-matrix parametrization of the amplitude is holomorphic, from the Schwarz reflection principle with

$$T(s)^* = K(s)^*\left(1 + i\rho(s)^*K(s)^*\right)^{-1} \tag{2.45}$$

and

$$T(s^*) = K(s^*)\left(1 - i\rho(s^*)K(s^*)\right)^{-1} \tag{2.46}$$

the following equalities can be deduced

$$K(s)^* = K(s^*) \quad \text{and} \quad \rho(s)^* = -\rho(s^*)\,. \tag{2.47}$$

Moreover, considering that $T(s)$ has a branch cut starting at a branch point s_{thr} along the positive real axis, then the first two Riemann sheets of the amplitude $T(s)$ are obtained using

$$T^{\text{I}}(s+i\epsilon) = T^{\text{II}}(s-i\epsilon)\,, \tag{2.48}$$

for $\epsilon \to 0$ and $s > s_{\text{thr}}$, where the roman numerals I and II indicate the first and second Riemann sheet, respectively. The inverse relation $T^{\text{I}}(s - i\epsilon) = T^{\text{II}}(s + i\epsilon)$ is viable for ranges of s, where only one branch point is relevant to the involved Riemann sheets of the continuation, for example in case of a single branch point. From the unitarity of the S-matrix one obtains through Eq. (2.38)

$$T^{\text{I}}(s + i\epsilon)\rho^{\text{I}}(s + \text{i}\epsilon)\left[T^{\text{I}}(s + i\epsilon)\right]^{\dagger} = \text{Im}\Big(T^{\text{I}}(s + i\epsilon)\Big) = \frac{1}{2\text{i}}\left(T^{\text{I}}(s + i\epsilon) - \left[T^{\text{I}}(s + i\epsilon)\right]^{\dagger}\right), \quad (2.49)$$

where $\rho^{\text{I}}(s + \text{i}\epsilon)$ is the phase space factor evaluated on the first Riemann sheet. Using the Schwarz reflection principle for T and Eq. (2.48)

$$T^{\text{II}}(s - \text{i}\epsilon) - T^{\text{I}}(s - \text{i}\epsilon) = 2\text{i}T^{\text{II}}(s - \text{i}\epsilon)\rho^{\text{I}}(s + \text{i}\epsilon)T^{\text{I}}(s - \text{i}\epsilon)\,, \quad (2.50)$$

can be achieved, which further can be arranged into

$$T^{\text{II}}(s - \text{i}\epsilon) = T^{\text{I}}(s - \text{i}\epsilon)\Big(1 - 2\text{i}\rho^{\text{I}}(s + \text{i}\epsilon)T^{\text{I}}(s - \text{i}\epsilon)\Big)^{-1}\,. \quad (2.51)$$

Last but not least, also the phase space needs to be analytically continued to the second Riemann sheet. This needs to be done carefully, since the correct Riemann sheet needs to be chosen. For the simplest case of only one branch point the phase space needs to be continued above that branch point. For a more involved case of two or more branch points the closest Riemann sheet above the branch point of consideration but below the next branch point needs to be chosen, which leads to a continuation prescription for the phase space functions according to Eq. (2.47). This is used extensively in Ch. 4. Nevertheless, using Eq. (2.47) we can achieve from Eq. (2.51)

$$T^{\text{II}}(s - \text{i}\epsilon) = T^{\text{I}}(s - \text{i}\epsilon)\Big(1 + 2\text{i}\rho^{\text{II}}(s - \text{i}\epsilon)T^{\text{I}}(s - \text{i}\epsilon)\Big)^{-1}\,, \quad (2.52)$$

which fully describes the amplitude on the second Riemann sheet.

2.5 Ward identities

Ward identities are an important implication of gauge invariance. In short, the statement is that if a physical amplitude involving a photon is contracted with the photon's 4-momentum instead of its polarization vector, the amplitude vanishes. In formulae, this is

$$q_\mu \mathcal{M}^\mu = 0\,, \quad (2.53)$$

where q_μ is the photons momentum. This is extensively used in Ch. 3 and we will sketch one version of a proof of Ward identities in the following, cf. Ref. [17].

We start by investigating the correlation function of two fermionic fields $\psi(x_1)\bar{\psi}(x_2)$ under a

global $U(1)$ symmetry $\psi \to e^{i\alpha}\psi$:

$$I_{12} = \langle \psi(x_1)\bar{\psi}(x_2)\rangle = \int \mathcal{D}\psi\mathcal{D}\bar{\psi}\exp\left(i\int d^4x\left[\bar{\psi}(i\not{\partial} - m)\psi + \dots\right]\right)\psi(x_1)\bar{\psi}(x_2)\,, \tag{2.54}$$

where the ... imply further locally symmetric terms, for example potential terms. When introducing a local degree of freedom, such as the local gauge phase of $U(1)_Q$:

$$\psi(x) \to e^{-i\alpha(x)}\psi(x)\,, \qquad \bar{\psi}(x) \to e^{i\alpha(x)}\bar{\psi}(x)\,, \tag{2.55}$$

the Lagrangian is *a priori* not invariant, since the derivative is not covariant. Expanding in $\alpha(x)$ to first order, we obtain

$$\begin{aligned} 0 = &\int \mathcal{D}\psi\mathcal{D}\bar{\psi}e^{iS}\left[i\int d^4x\bar{\psi}(x)\gamma^\mu\psi(x)\partial_\mu\alpha(x)\right]\psi(x_1)\bar{\psi}(x_2) \\ &+ \int \mathcal{D}\psi\mathcal{D}\bar{\psi}e^{iS}\left[-i\alpha(x_1)\psi(x_1)\bar{\psi}(x_2) + i\alpha(x_2)\psi(x_1)\bar{\psi}(x_2)\right]\,, \end{aligned} \tag{2.56}$$

which must hold for arbitrary $\alpha(x)$ and immediately leads to the Dyson–Schwinger equation

$$\partial_\mu\langle j^\mu(x)\psi(x_1)\bar{\psi}(x_2)\rangle = -\delta(x-x_1)\langle\psi(x_1)\bar{\psi}(x_2)\rangle + \delta(x-x_2)\langle\psi(x_1)\bar{\psi}(x_2)\rangle\,. \tag{2.57}$$

where $j^\mu = \bar{\psi}(x)\gamma^\mu\psi(x)$ is the QED current. Conveniently, the Fourier transform of the matrix element of the current with fermionic fields reads

$$\mathcal{M}^\mu(p,q_1,q_2) = \int d^4x d^4x_1 d^4x_2 e^{ipx}e^{iq_1x_1}e^{-iq_2x_2}\langle j^\mu(x)\psi(x_1)\bar{\psi}(x_2)\rangle\,. \tag{2.58}$$

Moreover, with the definitions

$$\mathcal{M}_0(q_1,q_2) = \int d^4x_1 d^4x_2 e^{iq_1x_1}e^{-iq_2x_2}\langle\psi(x_1)\bar{\psi}(x_2)\rangle \tag{2.59}$$

and

$$\mathcal{M}_0(q_1+p,q_2) = \int d^4x d^4x_1 d^4x_2 e^{ipx}e^{iq_1x_1}e^{-iq_2x_2}\delta^4(x-x_1)\langle\psi(x_1)\bar{\psi}(x_2)\rangle\,, \tag{2.60}$$

we can rewrite the matrix element as

$$ip_\mu\mathcal{M}^\mu(p,q_1,q_2) = \mathcal{M}_0(q_1+p,q_2) - \mathcal{M}_0(q_1,q_2-p)\,, \tag{2.61}$$

which is the more general version of the Ward identity, the so-called Ward–Takahashi identity [26–28]. Diagrammatically, Eq. (2.61) can be interpreted as shown in Fig. 2.3. Generalizing this to

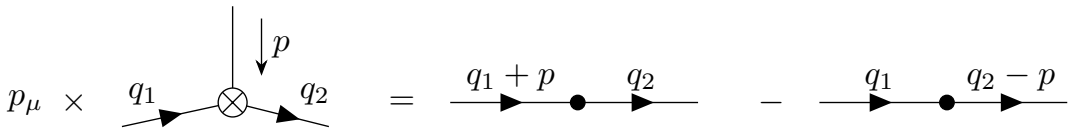

Figure 2.3: Diagrammatical depiction of the Ward–Takahashi identity.

f fermions and b currents, we can define

$$\begin{aligned} &M^{\mu\nu_1\dots\nu_b}(p, p_1 \dots p_b, q_1 \dots q_f) \\ &= \int \mathrm{d}^4x \mathrm{d}^4x_1 \mathrm{d}^4y_1 \dots e^{\mathrm{i}px} e^{\mathrm{i}p_1x_1} e^{-\mathrm{i}q_1y_1} \dots \langle j^\mu(x) j^{\nu_1}(x_1) \dots \bar{\psi}(y_1) \dots \rangle \end{aligned} \tag{2.62}$$

and as before, we can define

$$M^{\nu_1\dots\nu_b}(p_1 \dots p_b, q_1 \dots q_f) = \int \mathrm{d}^4x \mathrm{d}^4x_1 \mathrm{d}^4y_1 \dots e^{\mathrm{i}p_1x_1} e^{-\mathrm{i}q_1y_1} \dots \langle j^{\nu_1}(x_1) \dots \bar{\psi}(y_1) \dots \rangle \,. \tag{2.63}$$

With that, the generalized Ward–Takahashi identity is

$$\begin{aligned} \mathrm{i}p_\mu M^{\mu\nu_1\dots\nu_b}(p, p_1 \dots p_b, q_1 \dots q_f) &= \sum_{\text{out}} Q_i M^{\nu_1\dots\nu_b}(p_1 \dots q_i - p \dots q_f) \\ &\quad - \sum_{\text{in}} Q_i M^{\nu_1\dots\nu_b}(p_1 \dots q_i + p \dots q_f) \,, \end{aligned} \tag{2.64}$$

where Q_i is the charge of the i-th fermion field. To derive the *normal* Ward identity, we now need to use the LSZ reduction formula together with the Dyson-Schwinger equations. Consider an S-matrix element with two polarizations ϵ and ϵ_k

$$\begin{aligned} &\langle \epsilon \dots \epsilon_k \dots |S| \dots \rangle = \\ &= \epsilon^\mu \epsilon_k^\alpha \left[\mathrm{i}^n \int \mathrm{d}^4x e^{\mathrm{i}px} \left(\partial^2 g_{\mu\nu} - \left(1 - \frac{1}{\xi}\right) \partial_\mu \partial_\nu \right) \right. \\ &\left. \times \int \mathrm{d}^4x_k e^{\mathrm{i}p_k x_k} \left(\partial^2 g_{\alpha\beta} - \left(1 - \frac{1}{\xi}\right) \partial_\alpha \partial_\beta \right)_k \int \dots \right] \langle A^\nu(x) \dots A^\beta(x_k) \dots \rangle \,, \end{aligned} \tag{2.65}$$

where $\partial^2 g_{\mu\nu} - (1 - \frac{1}{\xi})\partial_\mu\partial_\nu$ is the photon kinematic term in covariant gauge and the ... stand for other particles in the scattering process.[3] Using the Dyson–Schwinger equations for the photon, we

[3] The actual gauge scheme of the photon is not important in the following.

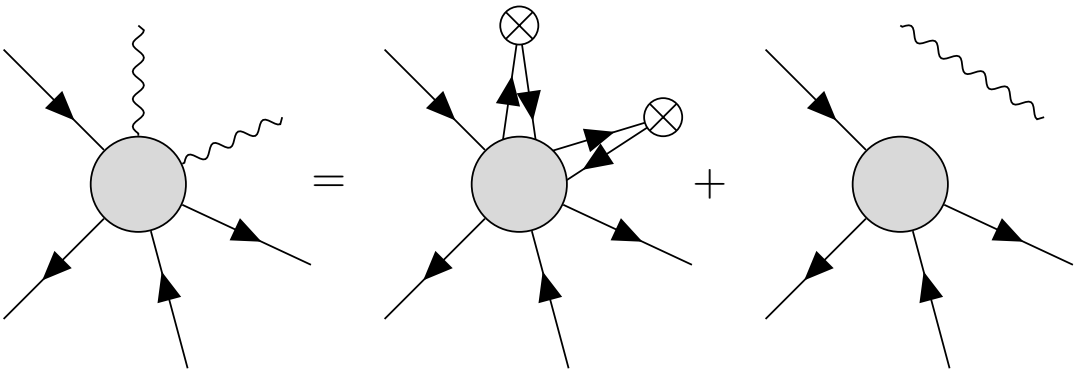

Figure 2.4: Diagrammatical representation of Eq. (2.66). The first diagram represents the replacement of photons by currents. The second diagram is disconnected and does not contribute to the S-matrix.

get

$$\begin{aligned}
&\left(\partial^2 g_{\alpha\beta} - (1-\frac{1}{\xi})\partial_\alpha\partial_\beta\right)_k \left(\partial^2 g_{\mu\nu} - (1-\frac{1}{\xi})\partial_\mu\partial_\nu\right) \langle A^\nu(x)\dots A^\beta(x_k)\dots\rangle \\
&= \left(\partial^2 g_{\alpha\beta} - (1-\frac{1}{\xi})\partial_\alpha\partial_\beta\right)_k \left[\langle j_\mu(x)\dots A^\beta(x_k)\dots\rangle - \mathrm{i}\delta^4(x-x_k) g_\mu^\beta \langle\dots\rangle\right] \\
&= \langle j_\mu(x)\dots j_\alpha(x_k)\dots\rangle + \left(\partial^2 g_{\mu\alpha} - (1-\frac{1}{\xi})\partial_\mu\partial_\alpha\right)_k \partial^2 D_F(x,x_k)\langle\dots\rangle\,, \qquad (2.66)
\end{aligned}$$

where $-\mathrm{i}\delta^4(x-x_k)$ is replaced by $\partial^2 D_F(x,x_k)$. Since the third diagram of Fig. 2.4 is a disconnected Feynman diagram, its contribution to the S-matrix vanishes. If we now replace the polarization ϵ_μ by the associated momentum p_μ in Eq. (2.65) and use Eq. (2.66), we obtain

$$\begin{aligned}
\langle p\dots\epsilon_k\dots|S|\dots\rangle &= \\
&= \Big[\mathrm{i}^n \int \mathrm{d}^4x e^{\mathrm{i}px} \int \mathrm{d}^4x_k e^{\mathrm{i}p_k x_k} \int \mathrm{d}^4x_k e^{\mathrm{i}q_1 y_1} \\
&\quad \times (\mathrm{i}\partial\!\!\!/_{y_1} - m_1)\dots\Big]\partial_\mu\langle j^\nu(x)\dots j^\alpha(x_k)\dots\psi(y_1)\dots\rangle \\
&= [(q\!\!\!/_1 - m_1)\dots]\mathrm{i}p_\mu M^{\mu\alpha_1\dots\alpha_b}(p,p_1\dots p_b,q_1\dots q_f)\,, \qquad (2.67)
\end{aligned}$$

where $M^{\mu\alpha_1\dots\alpha_b}$ is given by Eq. (2.62). Using the Ward-Takahashi identity, Eq. (2.64), this becomes

$$\langle p\dots\epsilon_k\dots|S|\dots\rangle = \pm e[(q\!\!\!/_1 - m_1)\dots]\sum_j Q_j M^{\alpha_1\dots\alpha_b}(p_1\dots q_j \pm p\dots q_f)\,, \qquad (2.68)$$

where j runs over all the external fermions, as shown diagrammatically in Fig. 2.5. To obtain the diagrams in Fig. 2.5, we replace the external photons by currents. For the photon with the polarization of interest, ϵ_μ, we instead replace the polarization by its momentum p_μ and add this to

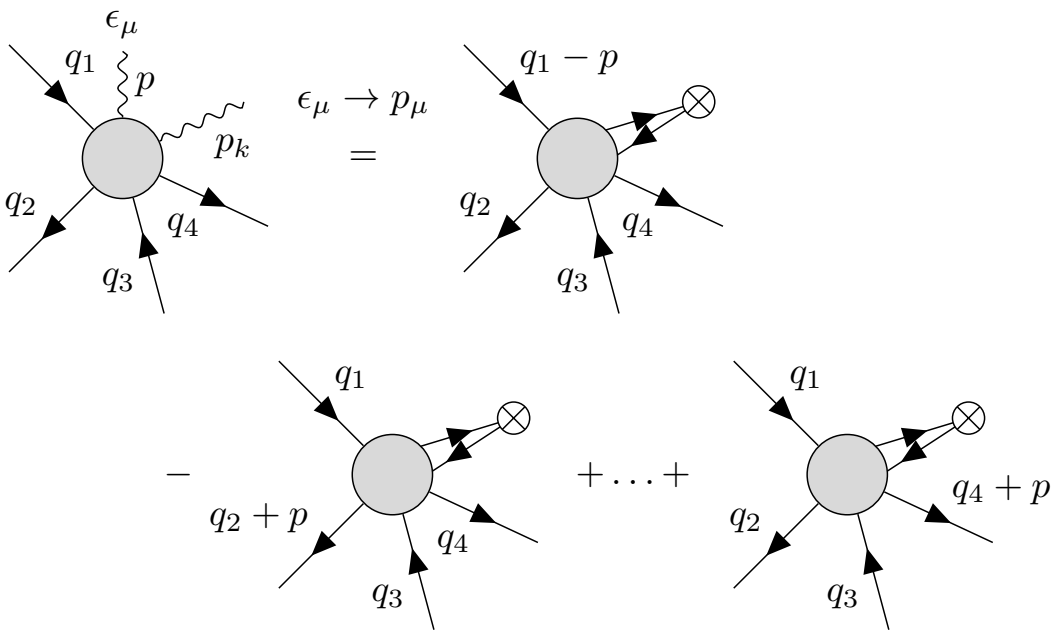

Figure 2.5: Diagrammatical representation of Eq. (2.68).

each external fermion momentum. We now have implemented in each term in the sum in Eq. (2.68) a pole at $(q_i \pm p)^2 = m_i^2$ instead of the natural pole at $q_i^2 = m_i^2$. This will vanish when multiplied by the factor $\not{q}_i - m_i = \frac{q_i^2 - m_i^2}{\not{q}_i + m_i}$ since q_i is an on-shell momentum with $q_i^2 = m_i^2$. Since all the terms in the sum vanish by that argument, the Ward identity Eq. (2.53) is proven. This also holds in general for off-shell momenta of the photon.

2.6 Parametrizing form factors — the Bardeen–Tung–Tarrach procedure

When dealing with tensor-valued hadronic matrix elements, it is crucial to find a parametrization using a set of a-priori unknown scalar functions. This approach is known as Lorentz decomposition. However, one must be cautious during this process, as improper parametrization can lead to violations of the Ward identity — a key principle that ensures the consistency of gauge theories. In the following, we present a straightforward way to implement the result of Sec. 2.5, that physical amplitudes involving photons vanish upon contraction with the photon's momentum instead of contraction with the photon's polarization vector. The Bardeen–Tung–Tarrach (BTT) procedure was developed in Refs. [29, 30] and used in a variety of modern literature, e.g., in the description of hadronic light-by-light scattering [31, 32]. The main point of the BTT procedure is to obtain a set of independent gauge-invariant and Lorentz-covariant tensors that are free of kinematical singularities and zeros, following a few rather simple steps:

- contract a gauge projector in the Lorentz index of all possible structures. Contract that

momentum in this Lorentz index, which shall reflect the Ward identity upon contraction with that very momentum;

- produce superpositions of all structures obtained that way to minimize the number of poles and double poles as far as possible without obtaining the same linear combination in any of the structures. For the superpositions, use coefficients with the relevant factors without introducing further poles;

- multiply all structures left with double poles — or start with the highest order of poles, in general — in $k \cdot q$ by a factor of $k \cdot q$;

- repeat the step of building superpositions to reduce the number of poles as far as possible;

- multiply the leftover poles by another factor of $k \cdot q$.

One can start by investigating a tensor of 2 independent momenta. A tensor of V−A nature can be generally expanded in Lorentz invariant structures as

$$T^{\mu\nu} = F_1 g^{\mu\nu} + F_2 \epsilon^{\mu\nu\alpha\beta} k_\alpha q_\beta + F_3 k^\mu q^\nu + F_4 q^\mu k^\nu + F_5 k^\mu k^\nu + F_6 q^\mu q^\nu \,, \tag{2.69}$$

where the F_i are structure functions of both momenta. For the Levi-Civita symbol, we use the sign convention $\epsilon^{0123} = +1$. In the following, we refer to the set of structures of Eq. (2.69) as

$$\left\{T_i^{\mu\nu}\right\} = \left\{g^{\mu\nu}, \epsilon^{\mu\nu\alpha\beta} k_\alpha q_\beta, k^\mu q^\nu, q^\mu k^\nu, k^\mu k^\nu, q^\mu q^\nu\right\} \,. \tag{2.70}$$

A gauge projector according to the BTT procedure could be

$$\mathcal{I}_{\mu\nu}(k,q) = g^{\mu\nu} - \frac{k^\mu q^\nu}{q \cdot k} \,. \tag{2.71}$$

To obtain a tensor that implements gauge invariance as $q_\mu T^{\mu\nu} = k_\nu T^{\mu\nu} = 0$, a contraction with the gauge projector as

$$\left\{\tilde{T}_i^{\mu\nu}\right\} = \mathcal{I}^\mu{}_\alpha \left\{T_i^{\alpha\beta}\right\} \mathcal{I}_\beta{}^\nu \tag{2.72}$$

is necessary. This results in the following set of gauge-invariant structures:

$$\left\{\tilde{T}_i^{\mu\nu}\right\} = \left\{g^{\mu\nu} - \frac{k^\mu q^\nu}{q \cdot k}, \epsilon^{\mu\nu\alpha\beta} k_\alpha q_\beta, 0, q^\mu k^\nu + \frac{q^2 k^2 k^\mu q^\nu}{(q \cdot k)^2} - \frac{q^2 k^\mu k^\nu}{q \cdot k} - \frac{k^2 q^\mu q^\nu}{q \cdot k}, 0, 0\right\} \,. \tag{2.73}$$

Since no superpositions to reduce the number of poles can be built here, $\tilde{T}_3^{\mu\nu}$ is multiplied by a factor of $q \cdot k$. As a result, in the next step, the superposition of $\tilde{T}_1^{\mu\nu}$ and $\tilde{T}_3^{\mu\nu}$ can be built, for

example as

$$\left\{\tilde{T'}_i^{\mu\nu}\right\} = \Big\{k^2q^2g^{\mu\nu} + k\cdot q q^\mu k^\nu - q^2k^\mu k^\nu - k^2q^\mu q^\nu, \epsilon^{\mu\nu\alpha\beta}k_\alpha q_\beta, 0, \\ k\cdot q q^\mu k^\nu + \frac{q^2k^2k^\mu q^\nu}{q\cdot k} - q^2k^\mu k^\nu - k^2q^\mu q^\nu, 0, 0\Big\}. \tag{2.74}$$

By multiplying structure $\tilde{T'}_3^{\mu\nu}$ once more by a factor of $q\cdot k$, structures free of kinematical singularities and zeros are obtained as

$$\{\hat{T}_i^{\mu\nu}\} = \Big\{k^2q^2g^{\mu\nu} + k\cdot q q^\mu k^\nu - q^2k^\mu k^\nu - k^2q^\mu q^\nu, \epsilon^{\mu\nu\alpha\beta}k_\alpha q_\beta, 0, \\ (k\cdot q)^2q^\mu k^\nu + q^2k^2k^\mu q^\nu - q\cdot k q^2k^\mu k^\nu - k^2q^\mu q^\nu, 0, 0\Big\}. \tag{2.75}$$

2.7 Dispersion relations

After performing a Lorentz decomposition of the tensor-valued matrix elements, we still do not know much about the scalar-valued functions that we introduced. However, hadronic dispersion relations provide a framework for relating these functions to established hadronic quantities. Specifically, hadronic dispersion relations are used to relate our form factor basis, used in Ch. 3, to the vector-meson form factors of Ref. [33]. Here, we explain the basics required to obtain these relations. In general, physical amplitudes are complex analytic functions on the whole complex plane except for branch cuts and poles. Let f be a holomorphic function $f(w) : \mathbb{C} \to \mathbb{C}$ and γ be some contour containing a point s, then Cauchy's integral formula reads

$$f(s) = \frac{1}{2\pi i}\oint_\gamma \frac{f(s')}{s'-s}\mathrm{d}s', \tag{2.76}$$

where the integration contour is oriented counterclockwise; an example for such an integration path is depicted in Fig. 2.6(a). Since such a contour integral is invariant under deformation of the integration path — as long as we avoid poles and branch cuts — we can deform the integration path at will, as depicted in Fig. 2.6(b). For the case of only a positive branch cut, the integral can be decomposed into an integration infinitesimally above and below the branch cut, resulting in a discontinuity

$$\mathrm{Disc} f(s) = f(s+\mathrm{i}\epsilon) - f(s-\mathrm{i}\epsilon) \tag{2.77}$$

and an arbitrarily large circle

$$f(s\pm\mathrm{i}\epsilon) = \frac{1}{2\pi i}\int_{s_\mathrm{thr}}^{\Lambda}\frac{\mathrm{Disc} f(s')}{s'-(s\pm\mathrm{i}\epsilon)}\mathrm{d}s' + \frac{1}{2\pi i}\int_{s'=|\Lambda|}\frac{f(s')}{s'-s}\mathrm{d}s', \tag{2.78}$$

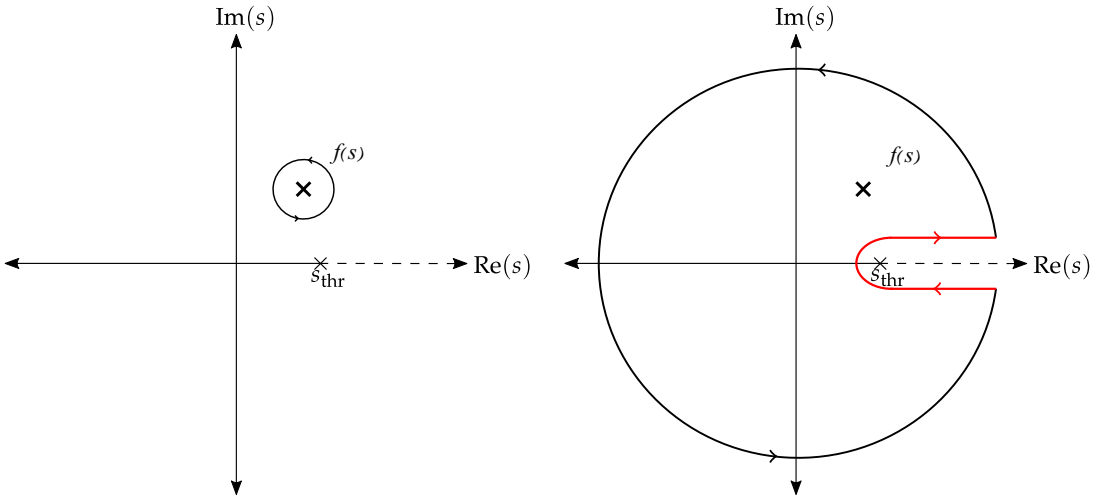

(a) Circle shaped integration contour around some point s. (b) Expanded integration contour avoiding the branch cut.

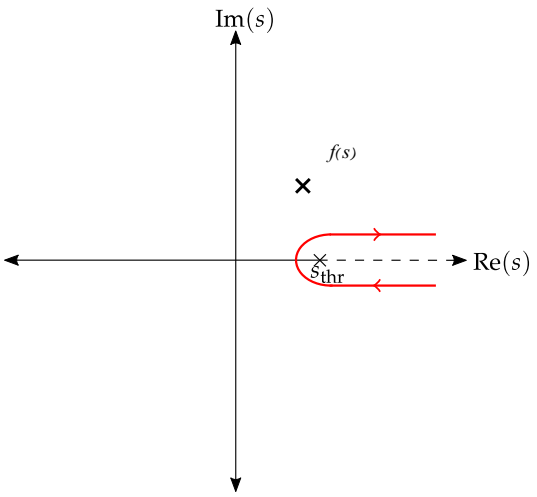

(c) When $f(s)$ vanishes fast enough on the large circle we can neglect its contribution and are left with the discontinuity along the branch cut.

Figure 2.6: Integration contour and its deformation in the complex plane to derive the dispersion-relation formula.

where Λ is the radius of this large circle. If $f(s)$ vanishes sufficiently fast for $|\Lambda| \to \infty$, the second term in Eq. (2.78) is negligible, which results in

$$f(s) = \frac{1}{2\pi i} \int_{s_{\text{thr}}}^{\infty} \frac{\text{Disc} f(s')}{s' - s} \mathrm{d}s', \tag{2.79}$$

as shown in Fig. 2.6(c). For the case that $f(s)$ does not vanish sufficiently fast for $|\Lambda| \to \infty$ one can introduce subtractions. One intuitive way to introduce subtractions is to expand the denominator in Eq. (2.79) using the identity

$$\begin{aligned} \frac{1}{s' - s} &= \frac{1}{s' - s} - \frac{1}{s' - s_0} + \frac{1}{s' - s_0} \\ &= \frac{s' - s_0}{(s' - s)(s' - s_0)} - \frac{s' - s}{(s' - s_0)(s' - s)} + \frac{1}{s' - s_0} \\ &= \frac{1}{s' - s_0} + \frac{s - s_0}{(s' - s)(s' - s_0)}, \end{aligned} \tag{2.80}$$

where s_0 is some arbitrarily chosen subtraction point. Using Eq. (2.80) in Eq. (2.79) leads to

$$f(s) = \frac{1}{2\pi \mathrm{i}} \int_{s_{\text{thr}}}^{\infty} \frac{\text{Disc} f(s')}{s' - s_0} \mathrm{d}s' + \frac{s - s_0}{2\pi \mathrm{i}} \int_{s_{\text{thr}}}^{\infty} \frac{\text{Disc} f(s')}{(s' - s)(s' - s_0)} \mathrm{d}s', \tag{2.81}$$

where the first term is independent of s and called a subtraction constant. In general, this procedure can be applied arbitrarily often, resulting in a N-times subtracted dispersion relation

$$f(s) = P_{N-1}(s) + \frac{(s - s_0)...(s - s_N)}{2\pi \mathrm{i}} \int_{s_{\text{thr}}}^{\infty} \frac{\text{Disc} f(s')}{(s' - s)(s' - s_0)...(s' - s_N)} \mathrm{d}s', \tag{2.82}$$

where $P_{N-1}(s)$ is called the *subtraction polynomial* and s_n is the n-th subtraction point. Evaluating Eq. (2.81) at the subtraction point s_0 we can identify the subtraction constant of the once subtracted dispersion relation with the function of the left-hand side (LHS) at the subtraction point.

2.8 Bayesian inference

Bayesian inference [34–37] represents one of the two principal approaches for deriving information from experimental data. In this section, we will present the foundational concepts and notations that will be employed in the subsequent chapters of this thesis. The probability that an abstract event A happens while an event B has happened, known as the conditional probability, is defined as

$$P(A|B) = \frac{P(A \cap B)}{P(B)}. \tag{2.83}$$

Here, the numerator $P(A \cap B)$ is the probability that events A and B both happened and the denominator $P(B)$ is the probability that event B happened. Given that the set of events A consists

of disjoint subsets A_i, the probability for the occurrence of B is

$$P(B) = \sum_i P(B|A_i)P(A_i). \tag{2.84}$$

Plugging both together and using the commutativity of $A \cap B = B \cap A$ yields the discrete Bayesian theorem

$$P(A|B) = \frac{P(B|A)P(A)}{\sum_i P(B|A_i)P(A_i)}. \tag{2.85}$$

For a set of parameters θ for a given model M and some data D, Bayes' theorem is

$$P(\theta|D, M) = \frac{P(D|\theta, M)P(\theta, M)}{Z}, \tag{2.86}$$

where the evidence Z for a continuous parameter is given as

$$Z = \int d\theta\, P(D|\theta, M)P(\theta, M). \tag{2.87}$$

In Eq. (2.86), $P(\theta, M)$ is called the prior density and $P(D|\theta, M)$ is the likelihood, when the data D is dependent on θ and the model M. The left-hand side $P(\theta|D, M)$ is the posterior probability density function, describing how likely the parameters θ are with respect to the given data and model. One of the goals of most analyses is to compare different models with one another, which is done using Bayes' theorem by comparing the odds of the posterior of two different models M_1 and M_2,

$$\frac{P(M_1|D)}{P(M_2|D)} = B_{12} \times \frac{P(M_1)}{P(M_2)}, \tag{2.88}$$

where B_{12} is Bayes' factor, built from the ratio of evidences of both models

$$B_{12} = \frac{P(D|M_1)}{P(D|M_2)} = \frac{Z_1}{Z_2} = \frac{\int d\theta P(D|\theta, M_1)P(\theta, M_1)}{\int d\theta P(D|\theta, M_2)P(\theta, M_2)}. \tag{2.89}$$

Here, a larger value of Bayes' factor implies that the Model M_1 is favored over Model M_2 for describing the dataset D. This is extensively used in the conclusions of Ch. 4. Moreover, a more intuitive interpretation of the Bayes' factor is given by Jeffreys [38]. The different levels of evidence according to Jeffreys are:

- $B_{12} < 1$: Strongly disfavored (evidence against M_1).
- $B_{12} = 1$: No evidence for or against either hypothesis.
- $1 < B_{12} < 3$: Barely worth mentioning (weak evidence in favor of M_1).
- $3 \leq B_{12} < 10$: Moderate evidence in favor of M_1.
- $10 \leq B_{12} < 30$: Strong evidence in favor of M_1.

- $B_{12} \geq 30$: Very strong evidence in favor of M_1.

CHAPTER 3

Dispersion relations for $B^- \to \ell^- \bar{\nu}_\ell \ell'^- \ell'^+$ form factors form factors

3.1 Prologue

The contents of this chapter are partially published in

- S. Kürten, M. Zanke, B. Kubis, and D. van Dyk, "*Dispersion relations for $B^- \to \ell^- \bar{\nu}_\ell \ell'^- \ell'^+$ form factors*", Phys. Rev. D **107**, (2023) 053006, DOI: https://doi.org/10.1103/PhysRevD.107.053006.[1]

Flavor physics is a promising field in the quest for discovering new physics. The task to reduce uncertainties is twofold. On the one hand, improvements on the frameworks lead to more detailed analyses. On the other hand, building models to access more data naturally reduces uncertainties of the extracted model parameters. Often disrespected principles in this field are unitarity and analyticity, which is an important ansatz to improve analyses on.

Here, we use dispersion relations to improve on the analytic properties of the form factor decomposition of the amplitude by relating the well-studied $B \to \gamma$ form factors to the highly discussed $B \to \gamma^*$ form factors. Thus, enabling an improvement of our analyses while simultaneously enabling the analyses to use more data. The $B \to \gamma^*$ form factors are crucial input in the analysis of $B^- \to \ell^- \bar{\nu}_\ell \ell'^- \ell'^+$ decays. To access more data sets, a valid parametrization of $B \to \gamma^*$ form factors is necessary, since, for the limit of vanishing photon momenta, these are equivalent to the on-shell case of $B \to \gamma$ form factors; used in the description of $B^- \to \ell^- \bar{\nu}_\ell \gamma$ decays.

This chapter is about the application of dispersion relations to $B \to \gamma^*$ form factors to relate these to the well-known on-shell $B \to V$ form factors within a vector-meson-dominance (VMD) model. A following discussion about the parametrization of the former $B \to \gamma^*$ form factors is within the main part of this chapter. The relation between on-shell and off-shell transition form factors is of paramount importance to access all the available data provided by experiments around the globe; especially data from the B-factory Belle at KEK as well as the LHCb experiment at

[1] see Ref. [8]

CERN. In this chapter, first, the fundamentals necessary for the computation of the amplitude are given. After that, the decomposition of the amplitude is discussed, where the amplitude is split into an initial-state-radiation and final-state-radiation part. The latter is discussed with special care to not produce unphysical divergences in the final amplitude. Furthermore, the specific application of dispersion relations to the form factors is discussed, where the Bardeen–Tung–Tarrach (BTT) procedure [29, 30] is applied to obtain a form factor basis free of kinematic singularities. Several incompatible parametrizations to decompose the amplitude are used, cf. Table 3.1. The most important ones are discussed and compared to the method presented here. Inconsistencies between the parametrizations are pointed out in Sec. 3.5. Both the author of this thesis and Marvin Zanke developed the formalism presented here independently of each other and cross-checked their results. Marvin Zanke focused more on the stringent application of the BTT procedure. The viability of the application of dispersion relations in the photon momentum are based on the operator product expansion (OPE) computation of Ref. [39], which was successfully carried out by the author of this thesis. Marvin Zanke contributed valuable cross-checks. The numerical evaluation of the results in Sec. 3.8 was performed independently by both the author of this thesis and Marvin Zanke. The numerical results were cross-checked and agree within their statistical uncertainties. In order to include the non-linear transformation of sampling a physical amplitude, the author of this thesis used a Monte-Carlo approach for the estimation of uncertainties as is detailed in Sec. 3.9. Furthermore, the author of this thesis developed a formalism with a once subtracted dispersion relation in the $B \to \gamma^*$ form factors. A subtracted dispersion relation in the relation of the $B \to \gamma^*$ form factors to the $B \to V$ form factors enables the formalism to use measurements as additional inputs and thus improve the predictive power of the numerical evaluation. The EOS software package [40] was extended by the author of this thesis with an implementation of the developed formalism and its once subtracted version, providing a valuable basis for the broader scientific community to make use of the results.

3.2 Introduction

The radiative leptonic decay $B^- \to \ell^- \bar{\nu}_\ell \gamma$ is widely considered to be the best source of information on the leading twist B-meson light-cone distribution amplitude (LCDA) by providing more insight of the inner structure of the B meson [10, 12, 41]. The B-factory experiment Belle II at KEK in Japan is one of the best experiments to measure this decay worldwide. At the LHCb experiment at CERN this decay is not as easily measured. However, the amount of data produced in LHCb is very large and completely independent of the Belle II data. Therefore, it is of major interest to use both data. The four-lepton decays of the B meson, $B^- \to \ell^- \bar{\nu}_\ell \ell'^- \ell'^+$ with $\ell' \neq \ell$, $\ell^{(\prime)} = e, \mu$, are great candidates to measure at both the LHCb and Belle II experiments. These decays involve the $B \to \gamma^*$ form factors, which have been discussed in recent literature [13–16]. However the extraction of the important LCDA parameters is blocked by the need of a good description of the virtual photon in the timelike region. Here, a dispersive approach for the $B \to \gamma^*$ form factors is presented, which is based on the fundamental principles of analyticity and unitarity. Dispersive analyses are usually applied to low-energy processes, such as the pion vector form factor; cf. Ref [42–49]. In this chapter, the methods for these low-energy processes are applied

to the $B \to \gamma^*$ transition form factors. The analyses presented here enable also the application in the spacelike region, where the sensitivity of LCDA parameters would be less polluted by soft contributions [12]. The $B \to \gamma^*$ form factors are split into their isoscalar and isovector components. The isovector component is dominated at small photon momentum transfer by the $\rho(770) \equiv \rho$ resonance. Similarly, the isoscalar component is dominated by the $\omega(782) \equiv \omega$ resonance in this region of the phase space. The individual components are related through hadronic dispersion relations to the respective $B \to \rho$ and $B \to \omega$ form factors [33]. Therefore, a VMD ansatz is applied, which can be extended to more involved methods in future work. To use the dispersion relation the form factors ought to be free of kinematic singularities, which is achieved by the Bardeen–Tung–Tarrach (BTT) procedure [29, 30]. The BTT procedure needs to be modified for the application in weak transitions. By splitting the amplitude in a part describing the initial-state radiation (ISR) and the final-state radiation (FSR) only the sum of both terms needs to be gauge invariant. Moreover, the separation of the amplitude in those two terms turns out to be ambiguous, where also the definiteness of angular momentum and parity quantum numbers should be taken care of. To avoid any inconsistencies with lepton masses, the mass $m_{\ell'}$ is explicitly treated as non-zero in the formulae throughout this chapter and the limit to zero is taken at the last possible point in this analysis.

3.3 The hadronic tensor in $B^- \to \ell^- \bar{\nu}_\ell \ell'^- \ell'^+$

We start by using the effective Lagrangian for B-meson decays

$$\mathcal{L}^{\text{eff}} = \frac{4G_F}{\sqrt{2}} V_{ub} \sum_i C_i O_i + \text{h.c.}\,, \tag{3.1}$$

where G_F is the Fermi constant, determined from muon decays, and V_{ub} is the CKM matrix element for $b \to u$ transitions. The basis of dimension six operators is

$$\begin{aligned} O_{V,L(R)} &\equiv \left[\bar{u}\gamma^\mu P_{L(R)} b\right] \left[\bar{\ell}\gamma_\mu P_L \nu_\ell\right]\,, \quad O_{S,L(R)} \equiv \left[\bar{u} P_{L(R)} b\right] \left[\bar{\ell} P_L \nu_\ell\right]\,, \\ O_T &\equiv \left[\bar{u}\sigma^{\mu\nu} b\right] \left[\bar{\ell}\sigma_{\mu\nu} P_L \nu_\ell\right]\,, \end{aligned} \tag{3.2}$$

where $P_{L(R)} = (1 \mp \gamma_5)/2$ are the left- and right-handed chiral projectors. For a SM description, as done throughout this thesis, $C_{V,L} = 1 + O(\alpha_e)$ and $C_{V,R} = C_{S,L(R)} = C_T = 0$ is used, where α_e is the fine-structure constant. To clarify our notation, we will initially examine the decomposition of the hadronic tensors associated with the intermediate decay of the B meson into an off-shell photon. The expression for the amplitude corresponding to this decay is given by:

$$\mathcal{M}(B^- \to \ell^- \bar{\nu}_\ell \gamma^*) = \frac{4G_F V_{ub}}{\sqrt{2}} \langle \ell^- \bar{\nu}_\ell \gamma^* | O_{V,L} | B^- \rangle\,. \tag{3.3}$$

For the further discussion, we introduce the operator as a product of local currents

$$O_{V,L} = \frac{1}{4} J_{\text{H}\nu}(0) J^\nu_{\text{W}}(0)\,, \tag{3.4}$$

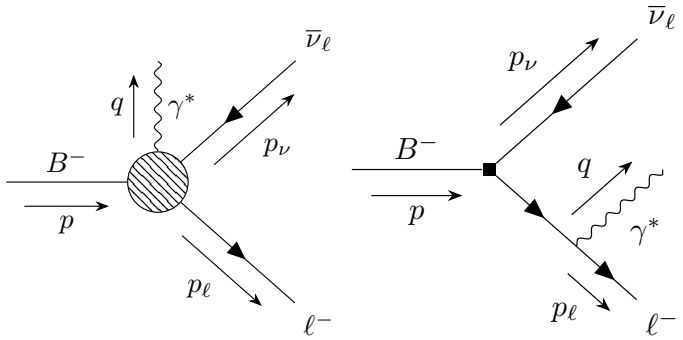

Figure 3.1: *Left*: Diagram depicting the ISR contribution to $B^- \to \ell^- \bar{\nu}_\ell \ell'^- \ell'^+$, where the shaded area accounts for all possible intermediate states like a B-meson or $\pi\pi$ state. *Right*: Diagram depicting the FSR contribution to $B^- \to \ell^- \bar{\nu}_\ell \ell'^- \ell'^+$, where the photon is radiated off of the charged final-state lepton.

where $J^\mu_{\mathrm{H}} = \bar{u}\gamma^\mu(1-\gamma_5)b$ and $J^\mu_{\mathrm{W}} = \bar{\ell}\gamma^\mu(1-\gamma_5)\nu_\ell$. Contributions to the amplitude of Eq. (3.3) are twofold. The off-shell photon can be radiated off the charged constituents of the B meson or off the charged lepton. Here, we speak of the initial-state radiation (ISR) and the final-state radiation (FSR), respectively. Diagrammatically, the ISR and FSR in the weak effective theory (WET) are depicted in Fig. 3.1.

The matrix element in Eq. (3.3) can be decomposed as

$$\begin{aligned}
\langle \ell^- \bar{\nu}_\ell \gamma^* | J_{\mathrm{H}\nu}(0) J^\nu_{\mathrm{W}}(0) | B^- \rangle &= e\epsilon^*_\mu \Big[\langle \ell^- \bar{\nu}_\ell | J_{\mathrm{W}\nu}(0) | 0 \rangle \int \mathrm{d}^4x e^{\mathrm{i}qx} \langle 0 | \mathrm{T}\{ J^\mu_{\mathrm{EM}}(x) J^\nu_{\mathrm{H}}(0) \} | B^- \rangle \\
&\quad + \langle 0 | J_{\mathrm{H}\nu}(0) | B^- \rangle \int \mathrm{d}^4x e^{\mathrm{i}qx} \langle \ell^- \bar{\nu}_\ell | \mathrm{T}\{ J^\mu_{\mathrm{EM}}(x) J^\nu_{\mathrm{W}}(0) \} | 0 \rangle \Big] \\
&= e\epsilon^*_\mu \Big[Q_B L_\nu T_H^{\mu\nu}(k,q) \\
&\quad - \mathrm{i} f_B p_\nu \int \mathrm{d}^4x e^{\mathrm{i}qx} \langle \ell^- \bar{\nu}_\ell | \mathrm{T}\{ J^\mu_{\mathrm{EM}}(x) J^\nu_{\mathrm{W}}(0) \} | 0 \rangle \Big] \\
&= e\epsilon^*_\mu \big[Q_B L_\nu T_H^{\mu\nu}(k,q) + Q_\ell T^\mu_{\mathrm{FSR}}(p_\ell, p_\nu, q) \big] ,
\end{aligned} \tag{3.5}$$

where $\epsilon^*_\mu \equiv \epsilon^*_\mu(q;\lambda)$ is the polarization vector of the photon with its momentum q and polarization λ, e is the elementary charge and the B-meson decay constant is defined via the B-meson-to-vacuum axial-vector matrix element as shown in Eq. (B.10). The electromagnetic current is

$$J^\mu_{\mathrm{EM}}(x) = \bar{q}(x) Q \gamma^\mu q(x) + \sum_\ell Q_\ell \bar{\ell}(x) \gamma^\mu \ell(x), \tag{3.6}$$

where $q(x) = (u(x), d(x), s(x), c(x), b(x))^\intercal$ and $Q = \mathrm{diag}[2/3, -1/3, -1/3, 2/3, -1/3]$ is the quark charge matrix. Moreover, we introduce the abbreviation

$$L_\nu = \langle \ell^- \bar{\nu}_\ell | J_{\mathrm{W}\nu}(0) | 0 \rangle \tag{3.7}$$

in Eq. (3.3) for the purely leptonic matrix element. Throughout this section, we keep the factors

$Q_B = Q_\ell = -1$ explicit in our equations, to clarify the resulting sign. The hadronic tensor is defined as

$$Q_B T_H^{\mu\nu}(k,q) = \int \mathrm{d}^4x e^{\mathrm{i}qx} \langle 0|\mathrm{T}\{J^\mu_{\mathrm{EM}}(x) J^\nu_{\mathrm{H}}(0)\}|B^-\rangle \tag{3.8}$$

and the FSR tensor as

$$Q_\ell T^\mu_{\mathrm{FSR}}(p_\ell, p_\nu, q) = -\mathrm{i} f_B p_\nu \int \mathrm{d}^4x e^{\mathrm{i}qx} \langle \ell^- \bar{\nu}_\ell|\mathrm{T}\{J^\mu_{\mathrm{EM}}(x) J^\nu_{\mathrm{W}}(0)\}|0\rangle \ . \tag{3.9}$$

The hadronic tensor $T_H^{\mu\nu}(k,q)$ describes the non-perturbative interactions and is parametrized by linearly independent Lorentz structures and form factors, cf. Sec. 3.4. In contrast, the FSR tensor $T^\mu_{\mathrm{FSR}}(p_\ell, p_\nu, q)$ is fully perturbative and the derivation of Eq. (3.10) and Eq. (3.11) is discussed in more detail in App. B. Here, we discuss the effects of neglecting the mass of the charged lepton from the W boson m_ℓ. When neglecting the mass m_ℓ the FSR tensor is given by the B meson decay constant and the leptonic matrix element as

$$T^\mu_{\mathrm{FSR}}(p_\ell, p_\nu, q) = f_B L^\mu \ . \tag{3.10}$$

For non-vanishing m_ℓ the expression reads

$$T^\mu_{\mathrm{FSR}}(p_\ell, p_\nu, q) = f_B \left[L^\mu + m_\ell \bar{u}_\ell \frac{2p_\ell^\mu + \gamma^\mu \not{q}}{(p_\ell + q)^2 - m_\ell^2} (1-\gamma_5) v_{\bar{\nu}} \right] , \tag{3.11}$$

which leads to a crucial difference in the complexity of the Lorentz structures to the massless case while discussing the decomposition of both cases. While for the massless case, the tensors in the last line of Eq. (3.5) factorize trivially by using Eq. (3.10), as

$$\langle \ell^- \bar{\nu}_\ell \gamma^*|J_{\mathrm{H}\nu}(0) J^\nu_{\mathrm{W}}(0)|B^-\rangle = e Q_B \epsilon^*_\mu \left[T_H^{\mu\nu}(k,q) + T^{\mu\nu}_{\mathrm{FSR}}(p_\ell, p_\nu, q) \right] L_\nu \, , \tag{3.12}$$

this does not work when including the mass term in Eq. (3.11). Only by using the Chisholm identity [50]

$$\mathrm{i}\epsilon^{\mu\nu\rho\sigma}\gamma_\sigma\gamma_5 = \gamma^\mu\gamma^\nu\gamma^\rho - g^{\mu\nu}\gamma^\rho + g^{\mu\rho}\gamma\nu - g^{\nu\rho}\gamma^\mu \, , \tag{3.13}$$

we can obtain the form

$$T^{\mu\nu}_{\mathrm{FSR}}(p_\ell, p_\nu, q) = f_B \left[g^{\mu\nu} + \frac{2p_\ell^\mu p_\ell^\nu + p_\ell^\mu q^\nu + q^\mu p_\ell^\nu - (p_\ell \cdot q) g^{\mu\nu} + \mathrm{i}\epsilon^{\mu\nu\rho\sigma} p_{\ell\rho} q_\sigma}{(p_\ell + q)^2 - m_\ell^2} \right] \tag{3.14}$$

and the same factorization as in Eq. (3.12). Since the Ward identity applies to the full amplitude, as described in Sec. 2.5, we obtain the constraint

$$q_\mu \left[T_H^{\mu\nu}(k,q) + T^{\mu\nu}_{\mathrm{FSR}}(p_\ell, p_\nu, q) \right] L_\nu = 0 \, . \tag{3.15}$$

However, the hadronic and FSR tensors are not gauge invariant on their own, thus leaving a

remainder upon contraction with the photon momentum q_μ

$$\begin{aligned} q_\mu T_H^{\mu\nu}(k,q) &= -f_B (k+q)^\nu \,, \\ q_\mu T_{\text{FSR}}^{\mu\nu}(p_\ell, p_\nu, q) &= f_B (k+q)^\nu \,. \end{aligned} \tag{3.16}$$

This leads to the idea of further decomposing the hadronic tensor — in analogy to differential equations — in a homogeneous and an inhomogeneous part

$$\begin{aligned} q_\mu T_{H,\text{hom.}}^{\mu\nu}(k,q) &= 0 \\ q_\mu T_{H,\text{inhom.}}^{\mu\nu}(k,q) &= -f_B (k+q)^\nu \,. \end{aligned} \tag{3.17}$$

For further investigation of this project, it is useful to make the pseudoscalar contribution to the hadronic tensor explicit, which leads to the relation

$$k_\nu T_{H,\text{hom.}}^{\mu\nu}(k,q) = T_P^\mu(k,q) + f_B (k+q)^\mu - k_\nu T_{H,\text{inhom.}}^{\mu\nu}(k,q) \,, \tag{3.18}$$

where the pseudoscalar tensor is defined as

$$Q_B T_P^\mu(k,q) = (m_b + m_u) \int \mathrm{d}^4 x e^{\mathrm{i}qx} \, \langle 0 | \mathrm{T}\{ J_{\text{EM}}^\mu(x) J_P(0) \} | B^- \rangle \,, \tag{3.19}$$

with the pseudoscalar current $J_P(x) = \bar{u}(x)\gamma_5 b(x)$. Similar to Eq. (3.16), the pseudoscalar tensor is not gauge invariant as the contraction with the photon momentum q_μ gives

$$q_\mu T_P^\mu(k,q) = -f_B m_B^2 \,. \tag{3.20}$$

Therefore, analogous to Eq. (3.17), we introduce

$$\begin{aligned} q_\mu T_{P,\text{hom.}}^{\mu}(k,q) &= 0 \,, \\ q_\mu T_{P,\text{inhom.}}^{\mu}(k,q) &= -f_B m_B^2 \,. \end{aligned} \tag{3.21}$$

Additionally, we introduce the constraint that

$$k_\nu T_{H,\text{hom.}}^{\mu\nu}(k,q) \stackrel{!}{=} T_{P,\text{hom.}}^{\mu}(k,q) \,, \tag{3.22}$$

which represents the pseudoscalar nature of the propagating B meson in the weak momentum k as shown in Fig. 3.2. Using Eq. (3.18), we can deduce

$$T_{P,\text{inhom.}}^{\mu}(k,q) + f_B (k+q)^\mu - k_\nu T_{H,\text{inhom.}}^{\mu\nu}(k,q) = 0 \,, \tag{3.23}$$

which turns out to relate the axial-vector like form factor with the pseudoscalar form factor, which is commonly used in weak decays [33]. The complete discussion of the tensor structures in this

section is analogously valid for the $B^- \to \ell^- \bar{\nu}_\ell \ell'^- \ell'^+$ amplitude and leads to

$$\begin{aligned}\mathcal{M}(B^- \to \ell^- \bar{\nu}_\ell \ell'^- \ell'^+) &= \frac{4G_F V_{ub}}{\sqrt{2}} \langle \ell^- \bar{\nu}_\ell \ell'^- \ell'^+ | O_{V,L} | B^- \rangle \\ &= \frac{4G_F V_{ub}}{\sqrt{2}} \frac{e^2}{q^2} Q_B \left[T_H^{\mu\nu}(k,q) + T_{\text{FSR}}^{\mu\nu}(p_\ell, p_\nu, q) \right] l_\mu L_\nu \,, \end{aligned} \tag{3.24}$$

where we have introduced the leptonic current $l_\mu = \bar{u}_{\ell'} \gamma_\mu v_{\bar{\ell}'}$. For identical lepton flavors, $\ell = \ell'$, the amplitude is far more involved [13, 51] due to contributions by the crossed diagrams and beyond the scope of this thesis.

3.4 Modified Bardeen–Tung–Tarrach procedure

In this part, we want to motivate the decomposition for the hadronic tensor. The homogeneous part of the hadronic tensor fulfills gauge invariance as in Eq. (3.17). To obtain a correct form factor decomposition for $B^- \to \ell^- \bar{\nu}_\ell \ell'^- \ell'^+$ we also impose

$$k_\nu T_{H,\text{hom.}}^{\mu\nu}(k,q) = T_{P,\text{hom.}}^{\mu}(k,q) \,. \tag{3.25}$$

Moreover, we can make an ansatz for $T_{H,\text{hom.}}^{\mu\nu}(k,q)$ by separating the pseudoscalar contribution via

$$T_{H,\text{hom.}}^{\mu\nu}(k,q) = \tilde{T}_{H,\text{hom.}}^{\mu\nu}(k,q) + T_{P,\text{hom.}}^{\mu}(k,q) \frac{k^\nu}{k^2} \,, \tag{3.26}$$

where $T_{P,\text{hom.}}^{\mu}(k,q)$ is necessarily multiplied by an additional factor carrying a second uncontracted Lorentz index. We choose the factor k^ν/k^2 here, since this implements a pole purely in the kinematic variable of the momentum transfer of the propagating B meson in Fig. 3.1. Nevertheless, such a pole can not end up in the final — and physical — decomposition without being countered by either multiplying it with a zero for $k^2 \to 0$ or subtracting a counter term originating from $\tilde{T}_{H,\text{hom.}}^{\mu\nu}(k,q)$. Here, we implement the latter method by using the standard BTT procedure, Sec. 2.6, for the pseudoscalar part and modify this method further to implement the k^2 pole in $\tilde{T}_{H,\text{hom.}}^{\mu\nu}(k,q)$. For the pseudoscalar tensor, the only possible Lorentz structures are

$$\left\{ L_{P,\text{hom.},i}^{\mu} \right\} = \left\{ k^\mu, q^\mu \right\} \,. \tag{3.27}$$

By contracting the gauge projector

$$\mathcal{I}^{\mu\nu} = g^{\mu\nu} - \frac{k^\mu q^\nu}{k \cdot q} \tag{3.28}$$

with the structures Eq. (3.27) as

$$\left\{ \tilde{L}_{P,\text{hom.},i}^{\mu} \right\} = \mathcal{I}_\alpha^\mu \left\{ L_{P,\text{hom.},i}^{\alpha} \right\} \,, \tag{3.29}$$

we obtain new gauge-invariant structures

$$\left\{\tilde{L}^{\mu}_{P,\text{hom.},i}\right\} = \left\{0, q^\mu - \frac{q^2}{k\cdot q}k^\mu\right\} . \tag{3.30}$$

Here, according to the standard BTT procedure, we need to remove the kinematical pole by multiplying a factor of $k \cdot q$, leading to the single non-vanishing structure

$$\hat{L}^{\mu}_{P,\text{hom.}} = (k\cdot q)q^\mu - q^2 k^\mu . \tag{3.31}$$

For $\tilde{T}^{\mu\nu}_{H,\text{hom.}}(k,q)$, a tensor with two uncontracted Lorentz indices, dependent on two momenta, and a vector and axial-vector part, the possible Lorentz structures are

$$\left\{\tilde{T}^{\mu\nu}_{H,\text{hom.}}(k,q)\right\} = \left\{g^{\mu\nu}, k^\mu k^\nu, k^\mu q^\nu, q^\mu k^\nu, q^\mu q^\nu, \epsilon^{\mu\nu\rho\sigma}k_\rho q_\sigma\right\} . \tag{3.32}$$

In this case, we use two gauge projectors; additionally to Eq. (3.28), we use

$$\tilde{\mathcal{I}}^{\mu\nu} = g^{\mu\nu} - \frac{k^\mu k^\nu}{k^2} \tag{3.33}$$

and perform the contraction as

$$\left\{\tilde{L}^{\mu}_{H,\text{hom.},i}\right\} = \mathcal{I}^{\mu}{}_{\alpha}\left\{L^{\alpha\beta}_{H,\text{hom.},i}\right\}\tilde{\mathcal{I}}_{\beta}{}^{\nu} . \tag{3.34}$$

The contractions in Eq. (3.34) implement poles in k^2 and $k \cdot q$,

$$\left\{\tilde{L}^{\mu}_{H,\text{hom.},i}\right\} = \left\{g^{\mu\nu} - \frac{k^\mu q^\nu}{k\cdot q}, 0, 0, 0, \frac{q^2}{k^2}k^\mu k^\nu - \frac{q^2}{k\cdot q}k^\mu q^\nu + q^\mu q^\nu, \epsilon^{\mu\nu\rho\sigma}k_\rho q_\sigma\right\} , \tag{3.35}$$

where we perform the usual BTT procedure only partially to keep the pole in k^2 in one structure. The BTT procedure is performed and results in

$$\begin{aligned}\left\{\hat{L}^{\mu\nu}_{H,\text{hom.},i}\right\} &= \left\{k\cdot q\tilde{L}^{\mu}_{H,\text{hom.},1}, \tilde{L}^{\mu}_{H,\text{hom.},5} - q^2\tilde{L}^{\mu}_{H,\text{hom.},1}, \tilde{L}^{\mu}_{H,\text{hom.},6}\right\} \\ &= \left\{k\cdot q g^{\mu\nu} - k^\mu q^\nu, \frac{q^2}{k^2}k^\mu k^\nu - \frac{k\cdot q}{k^2}q^\mu k^\nu + q^\mu q^\nu - q^2 g^{\mu\nu}, \epsilon^{\mu\nu\rho\sigma}k_\rho q_\sigma\right\} .\end{aligned} \tag{3.36}$$

Putting Eq. (3.31), Eq. (3.36) and Eq. (3.26) together, we obtain the full parametrization of $T^{\mu\nu}_{H,\text{hom.}}(k,q)$, which is then given in terms of the $B \to \gamma^*$ form factors by

$$\begin{aligned} m_B \cdot T^{\mu\nu}_{H,\text{hom.}}(k,q) = &\left[k\cdot q g^{\mu\nu} - k^\mu q^\nu\right] \mathcal{F}_1(k^2,q^2) \\ &+ \left[\frac{q^2}{k^2}k^\mu k^\nu - \frac{k\cdot q}{k^2}q^\mu k^\nu + q^\mu q^\nu - q^2 g^{\mu\nu}\right] \mathcal{F}_2(k^2,q^2) \\ &+ \left[\frac{k\cdot q}{k^2}q^\mu k^\nu - \frac{q^2}{k^2}k^\mu k^\nu\right] \mathcal{F}_3(k^2,q^2) + \mathrm{i}\epsilon^{\mu\nu\rho\sigma}k_\rho q_\sigma \mathcal{F}_4(k^2,q^2)\,, \end{aligned} \tag{3.37}$$

where we multiplied an additional factor of m_B to render the form factors $\mathcal{F}_i(k^2,q^2)$ dimensionless. Moreover, the form factors $\mathcal{F}_1(k^2,q^2)$ and $\mathcal{F}_2(k^2,q^2)$ carry axial-vector, $\mathcal{F}_3(k^2,q^2)$ carries pseudoscalar and $\mathcal{F}_4(k^2,q^2)$ vector quantum numbers. While $\mathcal{F}_1(k^2,q^2)$ and $\mathcal{F}_4(k^2,q^2)$ contribute to transverse polarized photon states — therefore being the only form factors contributing to the on-shell amplitude, $q^2 \to 0$ — the form factor $\mathcal{F}_2(k^2,q^2)$ represents the longitudinal and $\mathcal{F}_3(k^2,q^2)$ the time-like polarization. To keep the amplitude finite for $k^2 = 0$, the relation

$$\mathcal{F}_2(0,q^2) = \mathcal{F}_3(0,q^2) \tag{3.38}$$

needs to hold for all values of q^2.

3.5 Parametrization of the inhomogeneities

By Eq. (3.17), we can constrain the inhomogeneous part to

$$T^{\mu\nu}_{H,\text{inhom.}}(k,q) = -f_B\left[a g^{\mu\nu} + b\frac{k^\mu k^\nu}{k\cdot q} + c\frac{k^\mu q^\nu}{k\cdot q} + (1-b)\frac{q^\mu k^\nu}{q^2} + (1-a-c)\frac{q^\mu q^\nu}{q^2}\right], \tag{3.39}$$

where a, b and c are functions of k^2 and q^2. In Eq. (3.39), we make the most general ansatz for the inhomogeneous part by taking every possible Lorentz structure and multiplying this structure with a general prefactor. The Levi-Civita symbol is missing here, because the inhomogeneous part can only consist of axial-vector quantum numbers and the Levi-Civita symbol results in vector quantum numbers. Similarly, we make an ansatz for the inhomogeneous part of the pseudoscalar contribution as

$$T^{\mu\nu}_{P,\text{inhom.}}(k,q) = -f_B m_B^2\left[d\frac{k^\mu}{k\cdot q} + (1-d)\frac{q^\mu}{q^2}\right], \tag{3.40}$$

where d is a function of k^2 and q^2. Using Eq. (3.23), we find the relation

$$d = \frac{(1+a+c)k\cdot q + bk^2}{m_B^2}\,, \tag{3.41}$$

Label	a	b	c	$T^{\mu\nu}_{H,\text{inhom.}}(k,q)$	d	$T^{\mu}_{P,\text{inhom.}}(k,q)$	Ref.
$\mathcal{A}$	1	$\frac{2(k\cdot q)}{2(k\cdot q)+q^2}$	0	$-f_B\left[g^{\mu\nu}+\frac{(2k^\mu+q^\mu)k^\nu}{2(k\cdot q)+q^2}\right]$	$\frac{2(k\cdot q)}{2(k\cdot q)+q^2}$	$-f_B m_B^2 \frac{2k^\mu+q^\mu}{2(k\cdot q)+q^2}$	[39, 52–54]
$\mathcal{B}$	0	$\frac{k\cdot q}{k\cdot q+q^2}$	$\frac{k\cdot q}{k\cdot q+q^2}$	$-f_B\frac{(k+q)^\mu(k+q)^\nu}{k\cdot q+q^2}$	$\frac{k\cdot q}{k\cdot q+q^2}$	$-f_B m_B^2 \frac{k^\mu+q^\mu}{k\cdot q+q^2}$	[10, 55]
$\mathcal{C}$	0	1	1	$-f_B\frac{k^\mu(k+q)^\nu}{k\cdot q}$	$\frac{2(k\cdot q)+k^2}{2(k\cdot q)+k^2+q^2}$	$-f_B\left[m_B^2\frac{k^\mu}{k\cdot q}-\frac{q^2k^\mu-(k\cdot q)q^\mu}{k\cdot q}\right]$	[13]
$\mathcal{D}$	0	0	0	$-f_B\frac{q^\mu(k+q)^\nu}{q^2}$	$\frac{k\cdot q}{2(k\cdot q)+k^2+q^2}$	$-f_B\left[m_B^2\frac{q^\mu}{q^2}-\frac{(k\cdot q)q^\mu-q^2k^\mu}{q^2}\right]$	[14]

Table 3.1: Different combinations of parameters for the ansatz of the inhomogeneous tensor in Eq. (3.39) and Eq. (3.40). We label those choices of combinations from $\mathcal{A}$ to $\mathcal{D}$ and give the references that used the respective ansatz.

which is determined by the free parameters of Eq. (3.39). In total, 4 combinations of parameters were standing out, partially by the use in literature, and are summarized and labeled in Table 3.1. With the goal to use the parametrization within a dispersion relation in Sec. 3.6, the structures need to be free of singularities in q^2 but can still contain singularities in the variable k^2. Peculiar about choice $\mathcal{A}$ is the fact that it implements a denominator of the form

$$2(k\cdot q)+q^2 = m_B^2 - k^2\,, \tag{3.42}$$

where the right-hand side (RHS) is equivalent to the pole structure of the B-meson propagator. That matches actual contributions from the dashed region in Fig. 3.1, which are depicted in detail in Fig. 3.2. In contrast, the choices $\mathcal{B}$ and C implement a similar pole but with an additional q^2 dependence, which can not be associated to any intermediate state as in $\mathcal{A}$. The structures in choice $\mathcal{D}$ are orthogonal to all BTT structures, which keeps this choice directly free of kinematic poles. Nevertheless, choice $\mathcal{D}$ is of unphysical nature since it leads to terms $\propto 1/q^4$ in the squared amplitude, where the behavior of the amplitude must be $\propto 1/q^2$ as this represents the natural photon pole for $q^2 \to 0$. Moreover, choice $\mathcal{D}$ leads to a supposedly collinear enhancement, which can be best discussed by the spin-summed squared $B^- \to \gamma^* \ell^- \bar{\nu}_\ell$ amplitude

$$\begin{aligned}|\overline{\mathcal{M}}(B^- \to \ell^- \bar{\nu}_\ell \gamma^*(\lambda))|^2 = \frac{e^2 G_F^2 |V_{ub}|^2}{2} \epsilon^*_\mu(q;\lambda)\epsilon_\alpha(q;\lambda)\left[T_H^{\mu\nu}+T_{\text{FSR}}^{\mu\nu}\right]\left[T_H^{\alpha\beta}+T_{\text{FSR}}^{\alpha\beta}\right]^\dagger \\ \times \sum_{\text{all spins}} L_\nu L_\beta^\dagger\,,\end{aligned} \tag{3.43}$$

where λ represents the polarization of the off-shell photon. However, for choice $\mathcal{D}$, one finds that the matrix element diverges $\propto 1/q^2$. With a different parametrization of the homogeneous part, Ref. [14] uses choice $\mathcal{D}$ along with an inconsistent treatment of the lepton mass in the FSR term. Using the parametrization of the homogeneous tensor from Ref. [14] and our parametrization of the FSR term, which treats the lepton masses consistently, resolves the divergence $\propto f_B^2$. This strongly implies that the so-called collinear enhancement is an unphysical behavior. As yet another

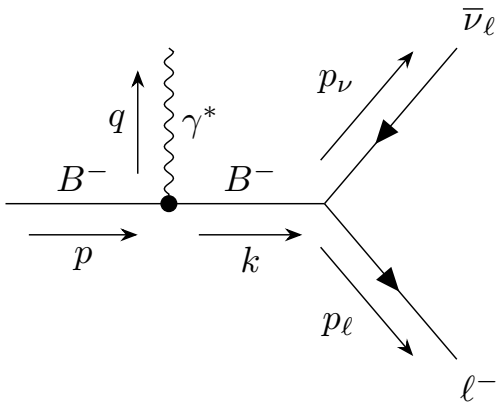

Figure 3.2: B-meson pole diagram. This diagram is a reason for the pole structure in $T^{\mu\nu}_{H,\text{inhom.}}(k,q)$ and is a partial contribution of Fig. 3.1.

argument that choice $\mathcal{A}$ is the correct choice amongst the ones listed in Table 3.1, a calculation of a similar hadronic matrix element in kaon decays by means of ChPT [53, 54] shows that choice $\mathcal{A}$ is indeed free of kinematic singularities up to order $O(p^4)$, where p is the kaon 4-momentum in Refs. [53, 54]. In contrast to this, transforming between choice $\mathcal{A}$ and any other choice in Table 3.1 introduces kinematic singularities in the respective homogeneous part of this choice. Moreover, Eq. (3.39) is the most general ansatz. Taking the following well-considered assumptions, we can generalize Eq. (3.39) in a more compact way. We assume that

- there is a unique choice of the coefficients in Eq. (3.39) that leaves the form factors free of kinematic singularities;
- there cannot be any kinematic singularities, e.g. $k \cdot q$ or q^2;
- there is a dynamic B-meson pole in the form factor $\mathcal{F}_3(k^2, q^2)$.

Together with the homogeneous part, Eq. (3.36), these assumptions lead to

$$T^{\mu\nu}_{H,\text{inhom.}}(k,q) = -f_B \left[\hat{a} g^{\mu\nu} + \frac{(2k^\mu + q^\mu)k^\nu + (1-\hat{a})(2k^\mu + q^\mu)q^\nu}{2k\cdot q + q^2} \right], \tag{3.44}$$

where $\hat{a}$ is a general real-valued coefficient that is independent of any of the momenta. For the pseudoscalar tensor, this gives

$$T^{\mu\nu}_{P,\text{inhom.}}(k,q) = -f_B \left[m_B^2 \frac{2k^\mu + q^\mu}{2k\cdot q + q^2} - (1-\hat{a}) \frac{q^2 k^\mu - k\cdot q q^\mu}{2k\cdot q + q^2} \right]. \tag{3.45}$$

Assuming that $\hat{a}$ fulfills the aforementioned requirements, one can set $\hat{a} = 1$. In that case it can be shown that a transformation to any other value for $\hat{a}$ would introduce a dynamic pseudoscalar B-meson pole in the axial-vector form factors $\mathcal{F}_1(k^2, q^2)$ and $\mathcal{F}_2(k^2, q^2)$. Since $\hat{a} = 1$ reproduces

choice $\mathcal{A}$ it further emphasizes this choice to be the best for our analysis. In total, we now have a basis of six linearly independent Lorentz structures as

$$T_H^{\mu\nu}(k,q) = T_{H,\text{hom.}}^{\mu\nu}(k,q) - f_B \left[g^{\mu\nu} + \frac{(2k^\mu + q^\mu)k^\nu}{2k\cdot q + q^2} \right] . \tag{3.46}$$

One can define a set of structures $\mathcal{P}_{\mu\nu_i}$, which fulfill

$$\mathcal{P}_{\mu\nu_i} T_H^{\mu\nu}(k,q) = \begin{cases} \mathcal{F}_i(k^2,q^2), & i = 1,\ldots,4\,, \\ f_B/m_B, & i = 5,6\,, \end{cases} \tag{3.47}$$

where we give the explicit formulae in App. B.2.

3.6 Application of dispersion relations

For our analysis, we split the $B \to \gamma^*$ form factors (cf. Eq. (3.37)) into their respective isospin contributions $I = 0$ and $I = 1$. We make a dispersive ansatz as described in Sec. 2.7 and assume that the discontinuities are dominated by the $\omega(782) \equiv \omega$ and $\rho(770) \equiv \rho$ states, respectively. The ϕ meson would also contribute to the isoscalar form factors but is suppressed by the Okubo–Zweig–Iizuka (OZI) mechanism [56–59], rendering its contribution is negligible. Using dispersion relations, we can relate each individual form factor $\mathcal{F}_i(k^2,q^2)$ of our set of $B \to \gamma^*$ form factors to the well-established $B \to V$ form factors [33] of $V = \omega, \rho$:

$$\begin{aligned} &\text{Disc}_{q^2}\left[Q_B \mathcal{F}_i(k^2,q^2) \right] = \text{Disc}_{q^2}\left[Q_B \mathcal{P}_{\mu\nu_i} T_H^{\mu\nu}(k,q) \right] \\ &= \mathcal{P}_{\mu\nu_i} \left[\mathrm{i} \sum_n \int \mathrm{d}\tau_n (2\pi)^4 \delta^{(4)}(q - P_n) \langle 0|J_{\text{EM}}^\mu(0)|n\rangle \langle n|J_{\text{H}}^\nu(0)|B^-\rangle \right] , \end{aligned} \tag{3.48}$$

where the n-body phase space volume is

$$\mathrm{d}\tau_n = \prod_j \frac{\mathrm{d}^3 p_j}{(2\pi)^3 2p_j^0} = \prod_j \frac{\mathrm{d}^4 p_j}{(2\pi)^4} 2\pi\delta(p_j^2 - M_j^2)\theta(p_j^0)\,, \tag{3.49}$$

with $P_n = \sum_j p_j$ being the total momentum of the intermediate state. Assuming VMD we use

$$\int \mathrm{d}\tau_n (2\pi)^4 \delta^{(4)}(q - P_n) f(P_n) = 2\pi\delta(q^2 - M_n^2) f(q)\,, \tag{3.50}$$

such that the discontinuity is given as

$$\text{Disc}_{q^2}\left[Q_B \mathcal{F}_i^I(k^2,q^2) \right] = \mathcal{P}_{\mu\nu_i} \left[2\pi\mathrm{i} \sum_\lambda \delta(q^2 - M_V^2) \langle 0|J_{\text{EM}}^\mu(0)|V(q,\lambda)\rangle \langle V(q,\lambda)|J_{\text{H}}^\nu(0)|B^-\rangle \right] . \tag{3.51}$$

For the $B \to V$ matrix elements in Eq. (3.51), we use the parametrization of Ref. [33]

$$\begin{aligned}
\langle 0|J^{\mu}_{\mathrm{EM}}(0)|V(q,\lambda)\rangle &= \frac{\eta^{\mu}}{c_V} d_V M_V f_V \,, \\
\langle V(q,\lambda)|J^{\nu}_{\mathrm{H}}(0)|B^-\rangle &= \frac{\eta^{*}_{\alpha}}{c_V}\Big[P_1^{\nu\alpha}(k,q)V^{B\to V}(k^2) + P_2^{\nu\alpha}(k,q)A_1^{B\to V}(k^2) \\
&\quad + P_3^{\nu\alpha}(k,q)A_3^{B\to V}(k^2) + P_P^{\nu\alpha}(k,q)A_0^{B\to V}(k^2)\Big] \,,
\end{aligned} \tag{3.52}$$

where $\eta^{\mu} \equiv \eta^{\mu}(q;\lambda)$ is the polarization vector, M_V the mass and f_V the decay constant of the intermediate vector meson. The factor d_V accounts for the quark composition of the ω and ρ meson, with $d_\omega = Q_u + Q_d = 1/3$ and $d_\rho = Q_u - Q_d = 1$, respectively. A factor c_V is introduced to account for the wave function of the ω and ρ meson, with $c_\omega = c_\rho = \sqrt{2}$. Finally, the form factors $V^{B\to V}(k^2)$, $A_1^{B\to V}(k^2)$, $A_3^{B\to V}(k^2)$ and $A_0^{B\to V}(k^2)$ are given in the traditional basis, which is purely heuristical. The Lorentz structures in Eq. (3.52) are

$$\begin{aligned}
P_1^{\nu\alpha}(k,q) &= \frac{2\mathrm{i}}{m_B + M_V}\epsilon^{\nu\alpha\beta\gamma} q_\beta k_\gamma \,, \\
P_2^{\nu\alpha}(k,q) &= -\frac{1}{m_B - M_V}\left[(m_B^2 - M_V^2)g^{\nu\alpha} - (k^\nu + 2q^\nu)k^\alpha\right] \,, \\
P_3^{\nu\alpha}(k,q) &= \frac{2M_V}{k^2}\left[k^\nu - \frac{k^2}{m_B^2 - M_V^2}(k^\nu + 2q^\nu)\right]k^\alpha \,, \\
P_4^{\nu\alpha}(k,q) &= -\frac{2M_V}{k^2}k^\nu k^\alpha \,,
\end{aligned} \tag{3.53}$$

where the phases are already converted to our parametrization in comparison to Ref. [33]. With the relation [33, 60]

$$A_{12}^{B\to V}(k^2) \frac{k^2(m_B + M_V)(m_B^2 - k^2 + 3M_V^2)A_1^{B\to V}(k^2) + 2M_V\lambda_V(k^2, m_B^2, M_V^2)A_3^{B\to V}(k^2)}{16 m_B M_V^2 (m_B + M_V)(m_B - M_V)} \,, \tag{3.54}$$

where $\lambda_V(k^2, m_B^2, M_V^2)$ is the Källén triangle function, $\lambda(x,y,z) = x^2 + y^2 + z^2 - 2(xy + xz + yz)$.[2] In the following, we use the short-hand notation $\lambda_V(k^2) \equiv \lambda_V(k^2, m_B^2, M_V^2)$. Furthermore, we can express the traditional form factor basis in terms of form factors that have well defined helicities. These form factors fulfill the relation

$$A_0(0) = \frac{8 m_B M_V A_{12}(0)}{m_B^2 - M_V^2} \tag{3.55}$$

[2] For a derivation of the Källén triangle function see Eq. (A.21)

$F^{B\to V}(k^2)$	J^P	m_{J^P}	$\alpha_0^{F,\omega}$	$\alpha_1^{F,\omega}$	$\alpha_2^{F,\omega}$	$\alpha_0^{F,\rho}$	$\alpha_1^{F,\rho}$	$\alpha_2^{F,\rho}$
$A_0^{B\to V}(k^2)$	0^-	m_B	0.328(48)	−0.83(30)	1.4(1.2)	0.356(42)	−0.83(20)	1.3(1.0)
$A_1^{B\to V}(k^2)$	1^+	m_{B_1}	0.243(31)	0.34(24)	0.09(57)	0.262(26)	0.39(14)	0.16(41)
$A_{12}^{B\to V}(k^2)$	1^+	m_{B_1}	0.270(40)	0.66(26)	0.28(98)	0.297(35)	0.76(20)	0.46(76)
$V^{B\to V}(k^2)$	1^-	m_{B^*}	0.304(38)	−0.83(29)	1.7(1.2)	0.327(31)	−0.86(18)	1.80(97)

Table 3.2: Values of the expansion coefficients of Eq. (3.58). We also show the parameters of the resonance factor in Eq. (3.58), where for m_{J^P}, the PDG values [61] of the respective mass are used. The values of the $\alpha_i^{F,V}$ are rounded to two significant digits. For the exact numerical values as well as details on the correlations and covariances, we refer to Ref. [33]. Here, the errors are numerically propagated by Gaussian sampling within the uncertainties given in Ref. [33].

exactly. For the matching process between our form factor basis and the form factors of Ref. [33], we expand every form factor in a conformal variable

$$z_V(t) = \frac{\sqrt{t_+ - t} - \sqrt{t_+ - t_0}}{\sqrt{t_+ - t} + \sqrt{t_+ - t_0}}, \tag{3.56}$$

for $V = \omega, \rho$, respectively. In Eq. (3.56), t_0 is chosen in a way to minimize the function value over the complete range of t, resulting in

$$t_0 = \left(1 - \sqrt{1 - \frac{t_-}{t_+}}\right) t_+, \tag{3.57}$$

where $t_\pm = (m_B \pm M_V)^2$. The expansion of the form factors of Ref. [33] is then given by

$$F^{B\to V}(k^2) = R_{J^P}(k^2) \sum_{j\geq 0} \alpha_j^{F,V} [z_V(k^2) - z_V(0)]^j, \tag{3.58}$$

where the expansion coefficients $\alpha_j^{F,V}$ are summarized in Table 3.2. The coefficient functions $R_{J^P}(k^2) = (1 - k^2/m_{J^P}^2)^{-1}$ are pole factors implementing the dominant subthreshold poles in the $B \to V$ transitions. The quantum numbers of the $R_{J^P}(k^2)$ for angular momentum and parity J^P can be read off in the second column of Table 3.2. Our form factors can be matched via a dispersion relation

$$Q_B \mathcal{F}_i^I(k^2, q^2) = \frac{1}{2\pi \mathrm{i}} \int_{s_{\text{thr}}}^{\infty} \mathrm{d}s \frac{\mathrm{Disc}_s \left[Q_B \mathcal{F}_i^I(k^2, s)\right]}{s - q^2}, \tag{3.59}$$

where $s_{\text{thr}} = 9M_\pi^2; 4M_\pi^2$ for $I = 0; 1$, respectively. No subtractions are needed here, as the integrand falls off sufficiently fast for $q^2 \to \infty$, as shown in Sec. 3.7. Though, it is of major interest to subtract these dispersion relations once, as shown in Sec. 3.10. Using the polarization sum for the ω and ρ,

$$\sum_\lambda \eta_\mu(q;\lambda)\eta_\nu^*(q;\lambda) = -g_{\mu\nu} + \frac{q_\mu q_\nu}{M_V^2}\,, \tag{3.60}$$

into the dispersion relation one obtains the $B \to \gamma^*$ form factors in the VMD model

$$\begin{aligned}
Q_B\mathcal{F}_1^I &= m_B M_V f_V d_V \frac{16 m_B M_V^2 A_{12}^{B\to V}(k^2) - (m_B + M_V)(m_B^2 - k^2 - M_V^2)A_1^{B\to V}(k^2)}{\lambda_V(k^2)(q^2 - M_V^2)}\,,\\
Q_B\mathcal{F}_2^I &= 2m_B M_V f_V d_V \frac{4m_B(m_B^2 - k^2 - M_V^2)A_{12}^{B\to V}(k^2) - (m_B + M_V)k^2 A_1^{B\to V}(k^2)}{\lambda_V(k^2)(q^2 - M_V^2)}\,,\\
Q_B\mathcal{F}_3^I &= m_B f_V d_V \frac{A_0^{B\to V}(k^2)}{q^2 - M_V^2}\,,\\
Q_B\mathcal{F}_4^I &= m_B M_V f_V d_V \frac{V^{B\to V}(k^2)}{(m_B + M_V)(q^2 - M_V^2)}\,.
\end{aligned} \tag{3.61}$$

Expanding the LHS of Eq. (3.61) using

$$Q_B\mathcal{F}_i^I = R_{J^P}(k^2)\sum_{j\geq 0}\beta_j^V(q^2)[z_V(k^2) - z_V(0)]^j\,, \tag{3.62}$$

where $R_{J^P}(k^2)$ is the same factor as used in Eq. (3.58), we can match both expansions order by order for each form factor. The expansion factors in Eq. (3.62) are defined as

$$\beta_j^V(q^2) = N_{i,j}^V P_V^{\text{BW}}(q^2)\,, \tag{3.63}$$

with

$$P_\omega^{\text{BW}}(q^2) = \frac{M_\omega^2}{M_\omega^2 - q^2 - \mathrm{i}M_\omega\Gamma_\omega}\,, \qquad P_\rho^{\text{BW}}(q^2) = \frac{M_\rho^2}{M_\rho^2 - q^2 - \mathrm{i}\sqrt{q^2}\Gamma_\rho}\,, \tag{3.64}$$

where we use a constant width above threshold for the ω meson and

$$\Gamma_\rho(q^2) = \theta(q^2 - 4M_\pi^2)\frac{\gamma_{\rho\to\pi\pi}(q^2)}{\gamma_{\rho\to\pi\pi}(M_\rho^2)}\,, \qquad \gamma_{\rho\to\pi\pi}(q^2) = \frac{(q^2 - 4M_\pi^2)^{3/2}}{q^2} \tag{3.65}$$

for the ρ meson. Fully matching both form factor bases, all $N_{i,j}^V$ can be determined, which are summarized in table Table 3.3. Our form factors are expressed in terms of the $B \to V$ form factors

$\mathcal{F}_i$	J^P	m_{J^P}	$N^\omega_{i,0}$	$N^\omega_{i,1}$	$N^\omega_{i,2}$	$N^\rho_{i,0}$	$N^\rho_{i,1}$	$N^\rho_{i,2}$
$\mathcal{F}_1$	1^+	m_{B_1}	0.0156(30)	−0.033(19)	0.003(85)	0.0557(88)	−0.115(48)	0.01(24)
$\mathcal{F}_2$	1^+	m_{B_1}	−0.186(27)	0.39(14)	−0.17(52)	−0.676(79)	1.34(41)	−0.6(1.5)
$\mathcal{F}_3$	0^-	m_B	−0.186(27)	0.47(17)	−0.80(71)	−0.676(79)	1.58(39)	−2.5(2.0)
$\mathcal{F}_4$	1^-	m_{B^*}	−0.0222(28)	0.061(21)	−0.125(91)	−0.0795(75)	0.209(44)	−0.44(23)

Table 3.3: Values of the normalizations, defined in Eq. (3.63), of our form factors $\mathcal{F}_i(k^2, q^2)$. We also show the parameters of the resonance factor in Eq. (3.62), where for m_{J^P} the PDG values [61] of the respective mass are used. The values of the $N^V_{i,j}$ are rounded to two significant digits. Here, the uncertainties are numerically propagated by Gaussian sampling through and within the uncertainties given in Ref. [33] of the parameters given in Table 3.2.

as

$$\begin{aligned} Q_B \mathcal{F}_i(k^2, q^2) &= Q_B \left[\mathcal{F}_i^{I=0}(k^2, q^2) + \mathcal{F}_i^{I=1}(k^2, q^2) \right] \\ &= R_{J^P}(k^2) \sum_{\substack{V=\omega,\rho \\ j\geq 0}} N^V_{i,j} P_V^{\mathrm{BW}}(q^2) [z_V(k^2) - z_V(0)]^j \,. \end{aligned} \tag{3.66}$$

3.7 Scaling of form factors

Here, we discuss the asymptotic behavior of our form factor decomposition for $q^2 \to \infty$. A necessity for applying the dispersion integral in Eq. (3.59) is that the discontinuity behaves as $\propto 1/q^2$ for large q^2, as already mentioned in the review in Sec. 2.7. We sketch that the form factors $\mathcal{F}_i^I$ as well as their discontinuities drop off at least as $\propto 1/q^2$ based on the results of an OPE calculation from Ref. [39]. To show the asymptotic behavior in our case it suffices to compute the leading-order diagrams, which are shown in Fig. 3.3. We use the interpolating B-meson current $J_B = \bar{u}(x)\gamma_5 b(x)$, which fulfills $\langle 0|J_B(0)|B^-\rangle = -\mathrm{i} m_B^2 f_B/(m_b + m_u)$, to obtain

$$\begin{aligned} X^I_{\mu\nu}(k, q) = e \int \frac{\mathrm{d}^4 l}{(2\pi)^4} \mathrm{Tr} \Bigg[&- \gamma_5 \frac{\mathrm{i}(\not{l} - \not{q} + m_u)}{(l-q)^2 - m_u^2} Q_u^I \gamma_\mu \frac{\mathrm{i}(\not{l} + m_u)}{l^2 - m_u^2} \gamma_\nu (1 - \gamma_5) \frac{\mathrm{i}(\not{l} + \not{k} + m_b)}{(l+k)^2 - m_b^2} \\ &- \gamma_5 \frac{\mathrm{i}(\not{l} - \not{k} + m_u)}{(l-k)^2 - m_u^2} \gamma_\nu (1 - \gamma_5) \frac{\mathrm{i}(\not{l} + m_b)}{l^2 - m_b^2} Q_b^I \gamma_\mu \frac{\mathrm{i}(\not{l} + \not{q} + m_b)}{(l+q)^2 - m_b^2} \Bigg], \end{aligned} \tag{3.67}$$

where l is the loop momentum and the photon momentum, q, is of large negative values; $q^2 < 0$. The charges of the different isospin states are given in Table 3.4. We find the projection of our form factor basis in the VMD model Eq. (3.61) by applying the projectors $\mathcal{P}_i^{\mu\nu}(k, q)$, defined in

$Q_u^{I=0}$	$Q_b^{I=0}$	$Q_u^{I=1}$	$Q_b^{I=1}$
$1/6$	$-1/3$	$1/2$	0

Table 3.4: Isospin charges used in Eq. (3.67).

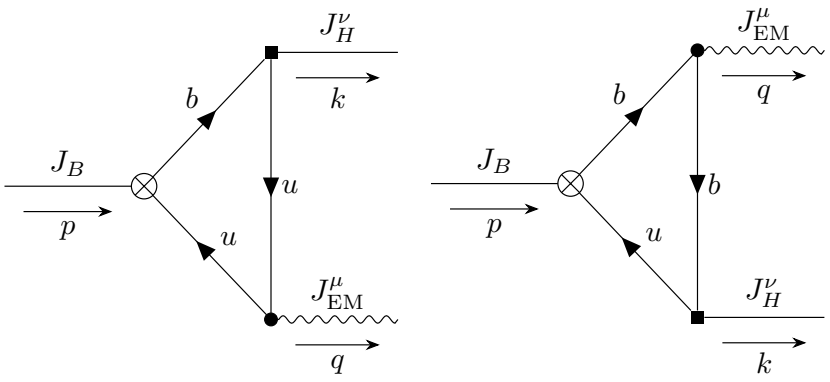

Figure 3.3: Leading-order diagrams used for the OPE computation. Higher-order diagrams do not contribute to the scaling in $1/q^2$.

Eq. (3.47), to Eq. (3.67)

$$\text{Disc}_{q^2} F_i^{I,\text{OPE}} \propto \text{Disc}_{q^2} \left[\mathcal{P}_i^{\mu\nu}(k,q) X_{\mu\nu}^I(k,q) \right] , \tag{3.68}$$

where we can compute the asymptotic behavior by using Eq. (3.67). We find that

$$\text{Disc}_{q^2} F_i^{I,\text{OPE}} \sim \frac{1}{q^2} , \tag{3.69}$$

which implies that no subtractions are necessary to apply the dispersion integral in Eq. (3.59). Moreover, we find that the form factors also scale as

$$F_i^{I,\text{OPE}} \sim \frac{1}{q^2} , \tag{3.70}$$

such that the monopole-like ansatz for our VMD framework is justified. Nevertheless, it is interesting to subtract the dispersion relation Eq. (3.59) once. One subtraction reduces the high-energy sensitivity, but enables the formalism to include one more parameter, which can be fixed by data. This is further discussed in Sec. 3.10, where the subtracted formalism is derived.

3.8 Numerical Predictions for $B^- \to \ell^- \bar{\nu}_\ell \ell'^- \ell'^+$

Here, we calculate the observables for the decay $B^- \to \ell^- \bar{\nu}_\ell \ell'^- \ell'^+$. The total decay width is given as

$$\mathrm{d}\Gamma = \frac{1}{2m_B} |\overline{\mathcal{M}}|^2 \mathrm{d}\Phi_4(p; p_\ell, p_\nu, q_1, q_2)\,, \tag{3.71}$$

where $|\overline{\mathcal{M}}|^2$ is the spin-summed and squared matrix element as given in Eq. (3.24). The 4-particle phase space $\mathrm{d}\Phi_4(p; p_\ell, p_\nu, q_1, q_2)$ is derived in App. A.3, where p is the momentum of the B meson, p_ℓ and p_ν are the momenta of the leptons originating from the W boson and q_1 and q_2 are the momenta of the leptons originating from the photon. The fully-differential decay rate is

$$\frac{\mathrm{d}^5\Gamma}{\mathrm{d}k^2 \mathrm{d}q^2 \mathrm{d}\cos\theta_W \mathrm{d}\cos\theta_\gamma \mathrm{d}\phi} = \frac{\sqrt{1 - \frac{4m_{\ell'}^2}{q^2}} \left(1 - \frac{m_\ell^2}{k^2}\right) \lambda^{1/2}\left(m_B^2, q^2, k^2\right)}{2^{15} m_B^3 \pi^6} |\overline{\mathcal{M}}|^2\,. \tag{3.72}$$

By integrating the angles in Eq. (3.72), one obtains the doubly-differential decay rate, which can be expressed as

$$\begin{aligned}\frac{\mathrm{d}^2\Gamma}{\mathrm{d}k^2 \mathrm{d}q^2} = \mathcal{N}\Bigg[&\sum_{i=1}^{4} \frac{f_{i,i}}{m_B^2} |\mathcal{F}_i(k^2, q^2)|^2 + 2 \sum_{\substack{i=1 \\ j>i}}^{4} \frac{f_{i,j}}{m_B^2} \mathrm{Re}\left[\mathcal{F}_i(k^2, q^2) \mathcal{F}_j^*(k^2, q^2)\right] \\ &+ 2 f_B \sum_{i=1}^{4} \frac{f_{i,5}}{m_B} \mathrm{Re}[\mathcal{F}_i(k^2, q^2)] + f_{5,5} f_B^2 \Bigg]\,,\end{aligned} \tag{3.73}$$

$$\mathcal{N} = \frac{G_F^2 V_{ub}^2 \alpha_e^2 (4\pi)^2}{2^{16} q^4 m_B^3 \pi^6} \sqrt{1 - \frac{4m_{\ell'}^2}{q^2}} \left(1 - \frac{m_\ell^2}{k^2}\right) \lambda^{1/2}\left(m_B^2, q^2, k^2\right)\,, \tag{3.74}$$

where the functions $f_{i,j}$ are summarized in App. B.1 and $\alpha_e = e^2/(4\pi)$. The absolute values of the form factors used in Eq. (3.73) are shown in Fig. 3.4. The full decay rate is obtained by integrating Eq. (3.73) over k^2 and q^2

$$\Gamma = \int_{4m_{\ell'}^2}^{(m_B - m_\ell)^2} \mathrm{d}q^2 \int_{m_\ell^2}^{\left(m_B - \sqrt{q^2}\right)^2} \mathrm{d}k^2 \frac{\mathrm{d}^2\Gamma}{\mathrm{d}k^2 \mathrm{d}q^2}\,. \tag{3.75}$$

The branching ratio is related to the decay width via

$$\mathcal{BR} = \frac{\Gamma \cdot \tau_B}{\hbar}\,, \tag{3.76}$$

where τ_B is the lifetime of the B meson and we summarize the numerical results for different final states and q^2 cutoffs in Table 3.5. Another observable is the forward–backward asymmetry in the

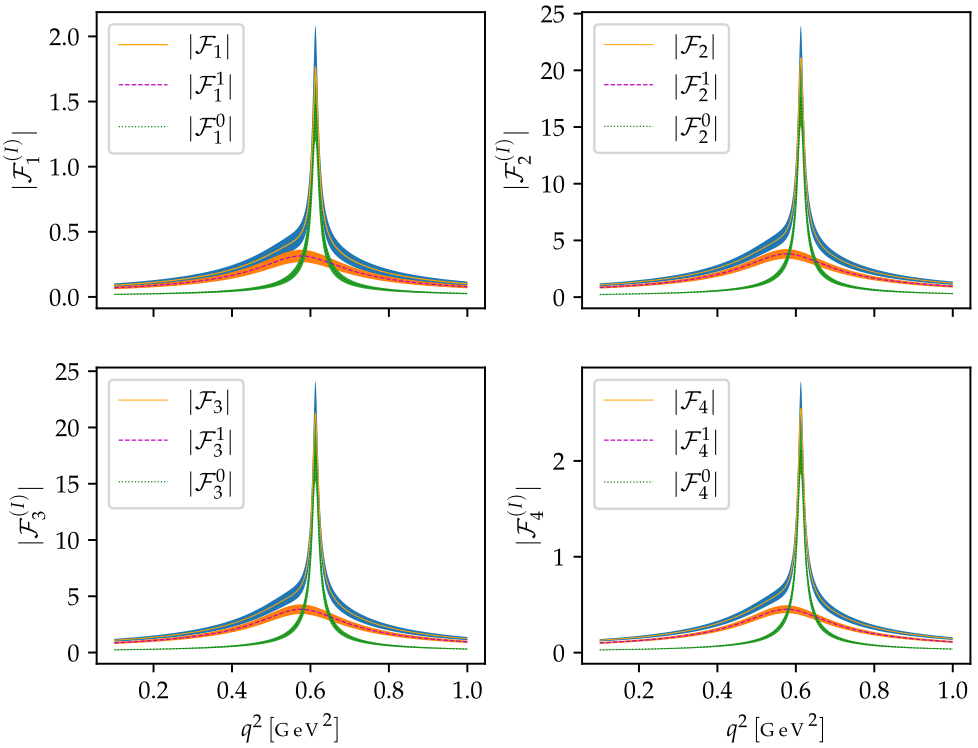

Figure 3.4: Absolute values of the form factors $\mathcal{F}_i(k^2, q^2)$ as functions of q^2 for a fixed value of $k^2 = 1\,\mathrm{GeV}$. The uncertainties are given as 68.27%, 1 σ, intervals from Gaussian sampling of the expansion coefficients in Eq. (3.58) from [33] using 50.000 samples.

angle $\cos_W$ defined by

$$A_{\mathrm{FB}}(k^2, q^2) = \left(\frac{\mathrm{d}^2\Gamma}{\mathrm{d}k^2\mathrm{d}q^2}\right)^{-1} \int \mathrm{d}\cos\theta_W \mathrm{sgn}\left[\cos\theta_W\right] \frac{\mathrm{d}^2\Gamma}{\mathrm{d}k^2\mathrm{d}q^2\mathrm{d}\cos\theta_W}\,, \tag{3.77}$$

where $\mathrm{sgn}[\cos\theta_W]$ defines the forward and backward directions. By integrating the angles, as we did for Eq. (3.73), we obtain the forward–backward asymmetry as

$$A_{\mathrm{FB}}(k^2,q^2) = \left(\frac{\mathrm{d}^2\Gamma}{\mathrm{d}k^2\mathrm{d}q^2}\right)^{-1} \times \mathcal{N}\Bigg[\sum_{i=1}^{4}\frac{g_{i,i}}{m_B^2}|\mathcal{F}_i(k^2,q^2)|^2 + 2\sum_{\substack{i=1\\j>i}}^{4}\frac{g_{i,j}}{m_B^2}\mathrm{Re}\Big[\mathcal{F}_i(k^2,q^2)\mathcal{F}_j^*(k^2,q^2)\Big] + 2f_B\sum_{i=1}^{4}\frac{g_{i,5}}{m_B}\mathrm{Re}[\mathcal{F}_i(k^2,q^2)] + g_{5,5}f_B^2\Bigg], \tag{3.78}$$

where the functions $g_{i,j}$ are summarized in App. B.1. In practice, only the binned asymmetry is experimentally accessible, which is given by

$$\Big\langle A_{\mathrm{FB}}(k^2,q^2)\Big\rangle = \left\langle\frac{\mathrm{d}^2\Gamma}{\mathrm{d}k^2\mathrm{d}q^2}\right\rangle^{-1}\int \mathrm{d}\cos\theta_W \mathrm{sgn}\left[\cos\theta_W\right]\left\langle\frac{\mathrm{d}^2\Gamma}{\mathrm{d}k^2\mathrm{d}q^2\mathrm{d}\cos\theta_W}\right\rangle, \tag{3.79}$$

where the angle brackets indicate the integration over k^2 and q^2 for said bin. The results of the integrated asymmetry for the integration of the complete range of k^2 and different cutoffs in q^2 as well as different final states of $B^- \to \ell^- \bar{\nu}_\ell \ell'^- \ell'^+$ are summarized in Table 3.5.

3.9 Estimation of uncertainties

When predicting observables from our results for the form factors based on the dispersion relation, a large number of parameters from the individual $B \to \rho$ and $B \to \omega$ form factors are incorporated. These parameters are, a priori, distributed as a multivariate Gaussian distribution. According to the central limit theorem, the observables, being sesquilinear functions of the form factors, are expected to converge to Gaussian distributions. Here, we test this assumption on the results of Table 3.5 and determine the uncertainties in a numerical simulation. We computed samples of a size of 50000 for the branching ratio and asymmetry of each final state in Table 3.5. This was done based on the mean values and covariances given by Ref. [33] using the formalism explained in the main part of this chapter. While computing the branching ratio or asymmetry in Eq. (3.75) and Eq. (3.78), the form factors enter the equation as absolute values squared. This is a non-linear transformation of the Gaussian samples of the form factors, which naturally leads to a skewness and kurtosis in the sample. For the sample process we used the Python language [62] in the interactive environment of Jupyter notebooks [63]. The following code produces two samples. Since we split the form factors into their isospin contributions, this code produces one sample for the ω-meson and one sample for the ρ-meson contribution:

Process	Upper cutoff in q^2	$\mathcal{BR}$ $[10^{-8}]$	A_{FB}
$B^- \to e^- \bar{\nu}_e \mu^- \mu^+$	None	$3.20^{+0.54}_{-0.47}$	$-0.358^{+0.031}_{-0.032}$
	1 GeV	$3.13^{+0.53}_{-0.46}$	$-0.361^{+0.031}_{-0.032}$
$B^- \to \mu^- \bar{\nu}_\mu e^- e^+$	None	$3.80^{+0.60}_{-0.53}$	$-0.398^{+0.038}_{-0.037}$
	1 GeV	$3.72^{+0.59}_{-0.54}$	$-0.402^{+0.037}_{-0.037}$
$B^- \to \tau^- \bar{\nu}_\tau e^- e^+$	None	$2.75^{+0.37}_{-0.33}$	$-0.496^{+0.019}_{-0.018}$
	1 GeV	$2.73^{+0.37}_{-0.33}$	$-0.501^{+0.019}_{-0.018}$
$B^- \to \tau^- \bar{\nu}_\tau \mu^- \mu^+$	None	$1.77^{+0.29}_{-0.26}$	$-0.456^{+0.018}_{-0.017}$
	1 GeV	$1.75^{+0.28}_{-0.25}$	$-0.459^{+0.015}_{-0.016}$

Table 3.5: Overview of the branching ratio as defined in Eq. (3.76) and the k^2 and q^2 integrated asymmetry as defined in Eq. (3.79). We give the values for all kinematically allowed final states of the decay $B^- \to \ell^- \bar{\nu}_\ell \ell'^- \ell'^+$ as well as for the full kinematically allowed range and a cutoff in q^2 at 1 GeV^2. The uncertainties are estimated by Gaussian propagation — using 50.000 samples — of the uncertainties of the expansion coefficients in Eq. (3.58) from Ref. [33]. Take note that the uncertainties become asymmetric here, since the Gaussian distributed samples of expansion coefficients are taken in quadrature in the spin-summed value squared amplitude $|\overline{\mathcal{M}}|^2$ and therefore distorted.

```
from scipy.stats import multivariate_normal as mvn

valueListOmega = []
for i in range (numberOfRandomSamples):
    valueListOmega.append(mvn.rvs(mean = rCVOmega,cov = rOmega))
valueListRho = []
for i in range (numberOfRandomSamples):
    valueListRho.append(mvn.rvs(mean = rCVRho,cov = rRho))
```

where first, empty lists are defined, `numberOfRandomSamples` is defined as 50000, `mean` takes the mean value and `cov` takes the covariance matrices given in Ref. [33]. Then, `scipy.stats`' `multivariatenormal` method [64] is used to create samples for Table 3.2, which are used to further compute the values in Table 3.3. Furthermore, for each entry in the sample the branching ratio (or the asymmetry) is computed by numerical integration as described in Eq. (3.75) (or Eq. (3.79)). The resulting sample has a skewness of 0.21 and a kurtosis of 0.16. The uncertainties are determined by taking the lower quantile at 15.865% and upper quantile at 84.135% and computing the difference to the median of the sample, this is equivalent to a 1σ error, since it

contains 68.3% of the sample. To visualize the skewness and kurtosis we also show a normalized Gaussian distribution in the left panel of Fig. 3.5 along the histogram of our sample. Moreover, we compare the CDF of a Gaussian normal distribution with the eCDF of our histogram in the right panel of Fig. 3.5. To create Fig. 3.5, we used matplotlib [65] to create the histogram and scipy's definition of a normal distributed probability density function [64] for the comparison with a normal distribution, with

```
A*scipy.stats.norm.pdf(x, mu, sigma),
```

where `mu` and `sigma` are the median and variance of the distribution shown in Fig. 3.5, the normalization A is

$$A = 5.34721 \cdot 10^{-5} = \sum_i \text{counts\_in\_bin}_i \times \text{bin\_width}\,, \tag{3.80}$$

with a bin_width of $1.06944 \cdot 10^{-9}$ and counts being the sample size of 50000. The normalization is needed here to show an equivalent normal distribution compared to the histogram shown in the left panel of Fig. 3.5.

3.10 Subtracted formalism

A central focus of the study of the $B \to \gamma$ form factors is its dependence on hadronic matrix elements that describe the substructure of the B meson. This dependence arises from a QCD factorization calculation [10]. The factorization formula is complicated by contributions from soft degrees of freedom, even at $q^2 = 0$. It is anticipated that these contributions will diminish as one transitions from $q^2 = 0$ to slightly spacelike values, for instance, $q^2 = s_0 = -2\,\text{GeV}^2$.

Here, we suggest to use the available data at lightlike and timelike q^2 and fit this data using a parametrization that extrapolates to s_0. Given the dispersive framework introduced earlier, we investigate a one-subtracted dispersion relation with subtraction point s_0. The subtraction is introduced as described in Sec. 2.7 according to

$$Q_B \mathcal{F}_i^I(k^2, q^2) = Q_B \mathcal{F}_i^I(k^2, s_0) + \frac{q^2 - s_0}{2\pi \mathrm{i}} \int_{s_\text{thr}}^\infty \mathrm{d}s\, \frac{\text{Disc}_s[Q_B \mathcal{F}_i^I(k^2, s)]}{(s - q^2)(s - s_0)}\,, \tag{3.81}$$

where s_0 is the *a priori* arbitrary subtraction point and $s_\text{thr} = 9M_\pi^2; 4M_\pi^2$ for $I = 0; 1$, respectively. Using the discontinuity Eq. (3.51) and the same procedure as in Sec. 3.6 to set our form factors

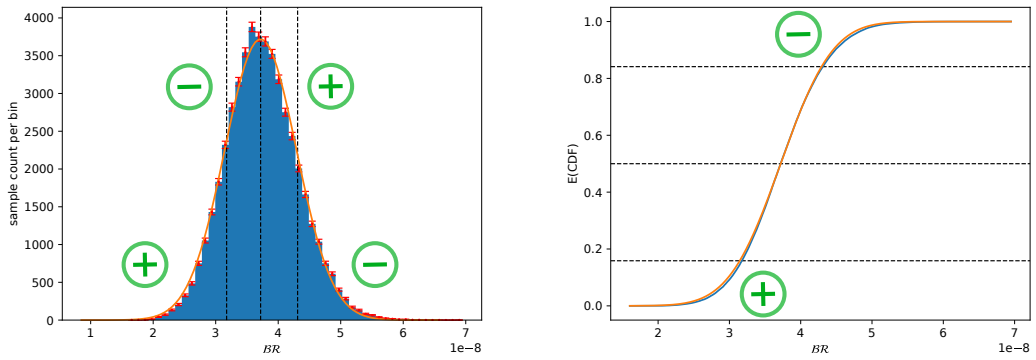

Figure 3.5: *Left:* Histogram of a sample of the branching ratio $B^- \to \mu^- \bar{\nu}_\mu e^- e^+$ without cutoff. The histogram is built from a sample of 50000 data points for the branching ratio and has a skewness of 0.21 and a kurtosis of 0.16. To visualize the estimation of uncertainties the lower quantile, median and upper quantile are shown by the dashed lines. To visualize the skewness and kurtosis of the distribution, a normal Gaussian distribution is shown in orange. In comparison to the histogram itself, one can see that the Gaussian overestimates the histogram on its left flank and underestimates the histogram closer to its peak. On the right flank of the histogram the gaussian overestimates the histogram close to its peak and underestimates it on its flank. For a better visualization the regions of over- and underestimation are marked by + and − signs, respectively. The statistical errors per bin are shown in red error bars in the middle of each bin. Especially at the upper and lower flanks one can see significant discrepancies between the histogram and the Gaussian normal distribution. *Right:* Empirical cumulative distribution function (eCDF) of a sample of the branching ratio $B^- \to \mu^- \bar{\nu}_\mu e^- e^+$ without cutoff is shown in blue. The CDF of a normal Gaussian distribution is shown in orange. The eCDF is built from a sample of 50000 data points for the branching ratio. To better visualize the estimation of uncertainties, the lower, median and upper quantile are shown by the horizontal dashed lines. As in the left panel, one can see a non-negligible deviation of the eCDF of the sample and the CDF of the normal Gaussian. The regions where the CDF over- and underestimates the eCDF are marked with a + and − sign, respectively.

$\mathcal{F}_i(k^2, q^2)$ in relation with the $B \to V$ form factors, we obtain

$$
\begin{aligned}
Q_B \mathcal{F}_1^I(k^2,q^2) &= Q_B \mathcal{F}_1^I(k^2,s_0) - m_B M_V f_V d_V \frac{q^2 - s_0}{M_V^2 - s_0} \\
&\quad \times \frac{16 m_B M_V^2 A_{12}^{B\to V}(k^2) - (m_B + M_V)(m_B^2 - k^2 - M_V^2) A_1^{B\to V}(k^2)}{\lambda_V(k^2)(M_V^2 - q^2)}, \\
Q_B \mathcal{F}_2^I(k^2,q^2) &= Q_B \mathcal{F}_2^I(k^2,s_0) - 2 m_B M_V f_V d_V \frac{q^2 - s_0}{M_V^2 - s_0} \\
&\quad \times \frac{4 m_B (m_B^2 - k^2 - M_V^2) A_{12}^{B\to V}(k^2) - (m_B + M_V) k^2 A_1^{B\to V}(k^2)}{\lambda_V(k^2)(M_V^2 - q^2)}, \\
Q_B \mathcal{F}_3^I(k^2,q^2) &= Q_B \mathcal{F}_3^I(k^2,s_0) - m_B f_V d_V \frac{q^2 - s_0}{M_V^2 - s_0} \frac{A_0^{B\to V}}{M_V^2 - q^2}, \\
Q_B \mathcal{F}_4^I(k^2,q^2) &= Q_B \mathcal{F}_4^I(k^2,s_0) - m_B M_V f_V d_V \frac{q^2 - s_0}{M_V^2 - s_0} \frac{V^{B\to V}(k^2)}{(m_B + M_V)(M_V^2 - q^2)}.
\end{aligned}
\tag{3.82}
$$

For the form factors on the LHS of Eq. (3.82), we make an ansatz using the series expansion

$$\mathcal{F}_i^I(k^2, q^2) = R_{J^P}(k^2) \sum_{j \geq 0} \beta_{i,j}^V(q^2)[z_V(k^2) - z_V(0)]^j, \tag{3.83}$$

where $\beta_{i,j}^V(q^2)$ is our model parameter. In contrast to Sec. 3.6, we now cannot define $\beta_{i,j}^V(q^2)$ as a normalization multiplied by a Breit–Wigner resonance, since the additional summand of $\mathcal{F}_i^I(k^2, s_0)$ in Eq. (3.82) makes this ansatz invalid. Instead we first proceed as far as possible and then introduce a Breit–Wigner ansatz. For the RHS we make a similar series expansion as shown in Eq. (3.83),

$$F^{B\to V}(k^2) = R_{J^P}(k^2) \sum_{j \geq 0} \alpha_j^{F,V}[z_V(k^2) - z_V(0)]^j \,. \tag{3.84}$$

In the following, we choose $Q_B = -1$. Moreover, we explain the procedure of matching the subtracted form factors $\mathcal{F}_i^I$ to the results of Ref. [33] in detail using the example of the longitudinal form factor $\mathcal{F}_3^I(k^2, q^2)$,

$$\mathcal{F}_3^I(k^2, q^2) = R_{J^P}(k^2) \sum_{j \geq 0} \beta_{3,j}^V(q^2)[z_V(k^2) - z_V(0)]^j = \tag{3.85}$$

$$\mathcal{F}_3^I(k^2, s_0) + m_B f_V d_V \frac{q^2 - s_0}{M_V^2 - s_0} \frac{1}{M_V^2 - q^2} R_{J^P}(k^2) \sum_{j \geq 0} \alpha_j^{A_0,V}[z_V(k^2) - z_V(0)]^j \,. \tag{3.86}$$

Redefining the subtraction polynomial by absorbing a factor of $1/R_{J^P}(k^2)$, we find

$$\sum_{j \geq 0} \beta_{3,j}^V(q^2)[z_V(k^2) - z_V(0)]^j = \mathcal{F}_3'^I(k^2, s_0) + m_B f_V d_V \frac{q^2 - s_0}{M_V^2 - s_0} \frac{1}{M_V^2 - q^2} \sum_{j \geq 0} \alpha_j^{A_0,V}[z_V(k^2) - z_V(0)]^j \,. \tag{3.87}$$

Expanding $\mathcal{F}_3'^I(k^2, s_0)$ around $z_V(0)$, we obtain

$$\sum_{j \geq 0} \beta_{3,j}^V(q^2)[z_V(k^2) - z_V(0)]^j = \sum_{j \geq 0} c_j^3(s_0)[z_V(k^2) - z_V(0)]^j + m_B f_V d_V \frac{q^2 - s_0}{M_V^2 - s_0} \frac{1}{M_V^2 - q^2} \sum_{j \geq 0} \alpha_j^{A_0,V}[z_V(k^2) - z_V(0)]^j \,, \tag{3.88}$$

where c_j are the coefficients of the series expansion of the subtraction polynomial. Selecting only

the j-th order of the expansion, we arrive at

$$\beta_{3,j}^{V}(q^2) = c_j^3(s_0) + m_B f_V d_V \frac{q^2 - s_0}{M_V^2 - s_0} \frac{1}{M_V^2 - q^2} \alpha_j^{A_0,V} . \tag{3.89}$$

Here, similar to the unsubtracted scenario in Sec. 3.6, we will assume VMD and use a Breit–Wigner ansatz to replace the factor $1/(M_V^2 - q^2)$ in Eq. (3.89) by the same $P_V^{\mathrm{BW}}(q^2)$ as used in Eq. (3.63). At this point, we can express the model parameter $\beta_{3,j}^{V}(q^2)$ in terms of the results of Ref. [33]

$$\beta_{3,j}^{V}(q^2) = c_j^3(s_0) + m_B f_V d_V \frac{q^2 - s_0}{M_V^2 - s_0} P_V^{\mathrm{BW}}(q^2) \alpha_j^{A_0,V} , \tag{3.90}$$

where every order in j of the expansion in $z_V(k^2) - z_V(0)$ is of the same form. Similarly, the model parameter of the 4$^{\text{th}}$ form factor can be expressed as

$$\beta_{4,j}^{V}(q^2) = c_j^4(s_0) + m_B f_V d_V \frac{q^2 - s_0}{(M_V^2 - s_0)(m_B + M_V^2)} P_V^{\mathrm{BW}}(q^2) \alpha_j^{V^{B\to V},V} . \tag{3.91}$$

For the 1$^{\text{st}}$ and 2$^{\text{nd}}$ model parameters, this is a bit more involved, since in Eq. (3.82) the form factors of Ref. [33] are multiplied by functions of k^2 instead of constant factors in k^2. Thus, one needs to first substitute k^2 with the conformal parameter $z_V(k^2)$ and expand this around $z_V(0)$, leading to a different expression in every order j of the expansion, which leads to very long expressions for these form factors. The unsubtracted and subtracted formalisms are implemented in EOS [40].

3.11 Summary and outlook

In this chapter, we study the $B \to \gamma^*$ form factors associated with the decay $B^- \to \ell^- \bar{\nu}_\ell \ell'^- \ell'^+$ using dispersive methods. We limit our study to different lepton flavors in the final state $\ell \neq \ell'$. We describe the $B^- \to \ell^- \bar{\nu}_\ell \ell'^- \ell'^+$ decay as a non-perturbative hadronic tensor and a perturbative FSR tensor, which allows to investigate the properties of both tensors individually. Throughout our analysis, we treat nonzero lepton masses consistently. The separation into a hadronic and a FSR tensor renders the decomposition into Lorentz structures and form factors ambiguous, which need to be free of kinematic singularities. This leads to a discussion about a further separation of the hadronic tensor into a homogeneous and inhomogeneous part, where we choose the homogeneous part to consist of Lorentz structures and form factors with well-defined angular momentum and parity quantum numbers. Moreover, this set of form factors and Lorentz structures is chosen to be free of kinematic singularities in the photon and the weak momentum, which fundamentally allows for the dispersive treatment. We discuss different parametrizations of the inhomogeneous part, compare those to choices used in literature and investigate the effects on the form factors, especially with regards to the singularity-free property of the form factors. We derive a choice that is preferable under certain assumptions. This choice is fixed for the remainder of our analysis. With this decomposition, we split the form factors into their isospin components and apply a set of

dispersion relation to relate our $B \to \gamma^*$ form factors to the well-established $B \to V$, $V = \omega, \rho$ form factors. The $B \to V$ form factors are expanded in the conformal variable $z(t)$, while the dominant sub-threshold contributions explicitly taken into account by pole factors. Applying the same expansion to the $B \to \gamma^*$ form factors and using a VMD ansatz to describe the virtual photon, we obtain a reasonable parametrization for our form factors. Using our parametrization, we compute numerical predictions for the branching ratio and forward-backward asymmetry, which agree with previous results from the literature. Moreover, we introduce a subtracted formalism by subtracting the dispersion relations relating our $B \to \gamma^*$ form factors to the $B \to V$ form factors once. This allows for the parametrization to be extrapolated to slightly spacelike values of q^2, where soft contributions to the QCD factorization of hadronic matrix elements are anticipated to diminish. Further improvements of our model could include the implementation of the ϕ-meson contribution and refining the VMD ansatz for the ρ meson by a description of the two-pion intermediate state [66]. In a similar way, one would reconstruct the $B \to \gamma^*$ using a dispersion relation to the $\eta^{(\prime)}$ transition form factors from two-pion intermediate states [67, 68].

CHAPTER 4

Analysis of the $\psi(3770)$ resonance in line with unitarity and analyticity constraints

4.1 Prologue

This chapter closely follows the publication

- C. Hanhart, S. Kürten, M. Reboud, and D. van Dyk, "*Analysis of the $\psi(3770)$ resonance in line with unitarity and analyticity constraints*", Eur. Phys. J. C. **84** (2024) 483, DOI: https://doi.org/10.1140/epjc/s10052-024-12785-8.[1]

In search for new physics, an iterative improvement of analyses is a promising method to find deviations from the standard model of particle physics. An important subject of interest throughout the flavor physics community are the $c\bar{c}$ resonances. Those can be observed, for example, in $e^+e^- \to c\bar{c}$ experiments, such as the Belle or BES experiments. Naturally, these resonances have the quantum numbers $J^{pc} = 1^{--}$. The first resonance in this spectrum is the famous J/ψ resonance at $3096.900 \pm 0.006\,\text{MeV}$ [61]. The J/ψ is very well separated from other resonances in this spectrum and is very accurately constrained, but the higher resonances in this spectrum are partly strongly overlapping and not very well constrained.

For the determination of long-distance effects in $b \to s\ell^+\ell^-$ a refined knowledge of the $c\bar{c}$ spectrum is crucial input and requires an analytic and unitary description of these resonances. In this chapter, we focused on the analysis of data from BES [69], BESII [70] and BESIII [71] to accurately determine resonance parameters of the $\psi(3770)$, in accordance with analyticity and unitarity, as a proof of concept for an analysis of the $c\bar{c}$ spectrum including as many resonances of the spectrum as possible.

Based on unitarity of the S-matrix, a K-matrix formalism for the amplitude is derived, which ultimately allows for the explicit implementation of resonances as poles on the closest unphysical Riemann sheet.[2] This formulation of the scattering amplitude is not fully analytic right away. By

[1] see Ref. [9]

[2] For the purpose of this work the closest unphysical Riemann sheet is the second Riemann sheet marked with a roman numeral II. Further Riemann sheets are possible when additional thresholds enter the formalism.

means of Chew–Mandelstam functions [24] as analytic continuation of the phase-space factors occurring within the K-matrix formalism, the author of this thesis has developed a fully analytic coupled-channel K-matrix formalism. Méril Reboud has provided useful cross-checks along with valuable discussions with the collaborators Christoph Hanhart and Danny van Dyk. The formalism uses, model-dependently, different sets of final-state channels and further parameters, such as background constants in the definition of the K-matrix or an effective momentum scale q_0. For each final-state channel, the high-energy behavior is regulated by inclusion of Blatt–Weisskopf factors. The low-energy behavior for each final-state channel is parametrized by the channels' orbital angular momentum and breakup momentum. This ansatz allows for extraction of the renormalized couplings G_k^r, for each resonance r and channel k, by numerical integration of a closed contour around the pole position on the second Riemann sheet. Physical parameters of interest, namely the mass and decay width of each resonance, as well as the cross-section of $e^+e^- \to k$ in the energy region of interest, are extracted. From the framework, detailed in Sec. 4.3, a total of five models are defined in Sec. 4.3.2. These models are primarily different in the number of included parameters. Each model includes the e^+e^- production channel, the exclusive final-state channels D^+D^- and $D^0\bar{D}^0$, the $\psi(3770)$ and $\psi(2S)$ resonances and either one or two effective channels. The number of included effective channels is primarily dependent on the fact whether or not the model allows for interference between the $\psi(3770)$ and $\psi(2S)$ resonances within the effective channels or not. Therefore, when no interference is allowed the model uses one more channel as compared to the interference case. Other considered models include the purely heuristical effective momentum scale q_0 or background constants to the K-matrix as fit parameters to check if a dependence on these parameters is relevant. The author of this thesis lead the fundamental discussions on the topic and implemented an early version of the formalism in the EOS software package [40]. Evaluating this early implementation provided useful knowledge about the coupled-channel analyses leading to the best fit results presented here. The implementation of the work presented here was done by Méril Reboud [72] along with the guidance of useful cross-checks of the author of this thesis. Furthermore, the author of this thesis has numerically evaluated the aforementioned models within the EOS software package [72], where he used the posterior probability density of the models' parameters to formulate statements about the reliability between these models based on Bayesian inference. The models must pass the viability tests defined in Sec. 4.3.2. These viability tests are further checks for the C++ implementation. Conclusions of these analyses are compared to previous literature, especially emphasizing the discrepancies in comparison to the branching ratios in Refs. [73, 74]. Moreover, the extracted mass $M_{\psi(3770)}$ and width $\Gamma_{\psi(3770)}$ of the $\psi(3770)$ is compared to the findings in several publications [61, 74, 75]. Furthermore, a lower $\mathcal{B}(\psi(3770) \to \text{non-}D\bar{D})$ than in other literature is found. Finally, in Sec. 4.5, some possibilities for future work in this field are proposed and the relations to non-local form factors in $b \to s\ell^+\ell^-$ decays are discussed.

4.2 Introduction

Production processes of $e^+e^- \to$ hadrons are of major interest throughout the particle physics community to investigate fundamentals of particle physics; especially the strong interaction. One of those fundamentals is the existence of exactly three strong charges, called colors [76]. Another

fundamental is the evidence of exotic states, which are momentarily not included in the established quark model (cf. Refs. [77–82]). Moreover, a detailed analysis on $e^+e^- \to$ hadrons data could help to improve predictions of hadronic contributions to the anomalous magnetic moment of the muon [83, 84]. In this chapter, we study $e^+e^- \to$ open-charm processes just above the first thresholds of $D^0\bar{D}^0$ and D^+D^- but still below the next $D\bar{D}^*$ + h.c. threshold. Relevant thresholds and resonance properties are listed in Table 4.1 and Table 4.2, respectively. The analysis presented here tackles the following questions:

- Is the experimental data consistent with the $\psi(3770)$ resonance being a pure $c\bar{c}$ state?
- Can a modern analysis properly describe the high-resolution measurement of available $e^+e^- \to$ open-charm data?
- Is there a significant improvement of the description when further resonances of mesonic vector states are added to describe the measurements?
- Is the description of the $e^+e^- \to$ open-charm spectrum of sufficiently high quality to put constraints on the description of non-local contributions in $b \to s\ell^+\ell^-$ processes?

The $e^+e^- \to$ open-charm spectrum has been investigated previously, e.g. Ref. [75], where several data sets — including BES [69], BESII [70] and BESIII [71] data — have been used. For the analysis in Ref. [75] a sum of Breit–Wigner functions has been used, which is known to violate unitarity of the S-matrix for broad resonances (resonances which are too close to one another relative to their widths). This results in the extraction of an $e^+e^- \to$ open-charm line shape, which cannot be applied to different processes, such as $b \to s\ell^+\ell^-$, without indeterminable model uncertainties. Here, we reduce the model uncertainties as much as possible. We use as few assumptions as necessary in our models and compare different types of assumptions. To exclude possible three-hadron final states we keep our analysis to a small phase-space window around the $\psi(3770)$ resonance. Moreover, we base our analysis on a K-matrix model, which respects unitarity by construction. A K-matrix model for analysis of purely exclusive $e^+e^- \to$ open-charm has been proposed in Ref. [85], where solely Belle data has been used. On the one hand, this Belle data covers a wider range of phase space but, on the other hand, the data set has far less resolution compared to the BES data sets used here. To extract more detailed information about the $\psi(3770)$ resonance's properties, the BES data sets should be superior. At first sight, our concepts might look similar to the analysis of Ref. [74], but the fundamental differences are that we explicitly allow for non-$D\bar{D}$ final states and for contributions of the $\psi(2S)$ resonance, which turns out to have a significant influence on the shape of the $\psi(3770)$ resonance. Also, we allow for interference between the $\psi(2S)$ and $\psi(3770)$, which seems to be crucial to describe the high-resolution data correctly.

4.3 Framework

The framework in this chapter follows Sec. 2.3. Here, we define the amplitude using the K-matrix ansatz as

$$\mathcal{M} = n\,[1 - \mathcal{K}\Sigma]^{-1}\,\mathcal{K}n\,. \tag{4.1}$$

$\sqrt{s}$ [MeV]	final state
3729.68	$D^0\bar{D}^0$
3739	D^+D^-
3871.69	$D^{*0}\bar{D}^0$ + c.c.
3879.76	$D^{*+}D^-$ + c.c.

Table 4.1: Relevant two-particle thresholds [61].

resonance	$J/\psi(1S)$	$\psi(2S)$	$\psi(3770)$
mass [MeV]	3096.900 ± 0.006	3686.097 ± 0.010	3773.7 ± 0.7
Γ [MeV]	$(92.6 \pm 1.7) \times 10^{-3}$	$(286 \pm 16) \times 10^{-3}$	27.2 ± 1.0
$\Gamma_{e^+e^-}/\Gamma$	$(5.971 \pm 0.032) \times 10^{-2}$	$(7.94 \pm 0.22) \times 10^{-3}$	$(9.6 \pm 0.7) \times 10^{-6}$

Table 4.2: Masses, total width and branching ratio to e^+e^- [61].

By construction the K-matrix is real-valued and symmetric, which ensures unitarity of the S-matrix and symmetry under time-reversal. To model the different orbital-angular-momentum dependent opening slopes of the phase-space contribution we define the diagonal matrix $n = \mathrm{diag}(n_a, n_b, \dots)$ with

$$n_k = (q_k/q_0)^{l_k} F_{l_k}(q_k/q_0)\,, \tag{4.2}$$

where l_k is the orbital angular momentum and

$$q_k(s) = \frac{\lambda\left(s, M_{k_1}^2, M_{k_2}^2\right)^{1/2}}{2\sqrt{s}} \tag{4.3}$$

is the breakup momentum of channel k. The breakup momentum is expressed in terms of the Källén triangle function λ, where M_{k_1} and M_{k_2} are the masses of both hadrons in channel k. Moreover, the breakup momentum Eq. (4.3) is used to define the available phase space in terms of the center-of-mass energy

$$\rho_k(s) = \frac{q_k(s)}{8\pi\sqrt{s}}\,. \tag{4.4}$$

Furthermore, the momentum scale q_0 is chosen empirically to be between 0.2 GeV and 1 GeV; cf. Refs. [61, 86]. The Blatt–Weisskopf factors [87] are

$$F_0^2(z) = 1\,, \qquad F_1^2(z) = 1/(1+z^2)\,. \tag{4.5}$$

The phase space is modeled by the diagonal self-energy matrix $\Sigma = \mathrm{diag}(\Sigma_a(s), \Sigma_b(s), \dots)$, where the Σ_k are the channel specific Chew–Mandelstam functions. Additionally, the Chew–Mandelstam functions are the analytic continuations of the phase space factors $\mathrm{i}\rho_k(s)n_k(s)^2$ and, therefore, allow for the continuation of the amplitude to the whole complex plane. In the following, we only consider equal masses for the hadrons in the decay channels, such that $M_{k_1} = M_{k_2}$, which leads to

$$\Sigma_k(s) = \frac{1}{8\pi^2}\Pi_0 \tag{4.6}$$

for an S-wave channel and

$$\Sigma_k(s) = \frac{1}{8\pi^2}\frac{s - s_{\mathrm{thr}}}{s_0}(F_1^2(q_k(s)/q_0)\Pi_0(s) + \Pi_1(s)) \tag{4.7}$$

for a P-wave channel. Here, we defined

$$\Pi_0 = -\frac{\sqrt{s - s_{\mathrm{thr}}}}{\sqrt{s}}\arctan\sqrt{\frac{s}{s_{\mathrm{thr}} - s}}\,, \tag{4.8}$$

$$\Pi_1 = \frac{s_0^{3/2}}{\sqrt{s_0 - s_{\mathrm{thr}}}(s + s_0 - s_{\mathrm{thr}})}\mathrm{atanh}\sqrt{1 - \frac{s_{\mathrm{thr}}}{s_0}}\,, \tag{4.9}$$

where $s_{\mathrm{thr}} = 4M_k^2$ and $s_0 = 4q_0^2$. So far we were able to discuss the first Riemann sheet, to analytically continue the aforementioned formulae to the second Riemann sheet we use the analytic continuation of the Chew–Mandelstam functions

$$\Sigma_k^{\mathrm{II}}(s) = \Sigma_k^{\mathrm{I}}(s) + 2\mathrm{i}\left(\rho_k(s^*)n_k^2(s^*)\right)^*\,, \tag{4.10}$$

where the roman literals imply the function being evaluated on their first and second Riemann sheet respectively, cf. Sec. 2.4. The second part on the RHS is the discontinuity along the real axis. The arrangement of complex conjugations evaluates the branch cut term infinitesimally on "the other side", namely the second sheet, such that the function is analytically continued.

The K-matrix is parametrized as:

$$\mathcal{K}_{ij}(s) = \sum_{r=1}^{\mathrm{N_R}}\frac{g_i^r g_j^r}{m_r^2 - s} + c_{ij}\,, \tag{4.11}$$

where the first term on the RHS implements a pole for each resonance R with a bare mass m_r and a bare coupling g_i^r to channel i, both being real-valued parameters. The second term is a background constant modeling non-resonant contributions, for example tails of resonances outside of our represented phase space window. The pole position on the second Riemann sheet is given by

$$\sqrt{s_r} = M_r - \mathrm{i}\frac{\Gamma_r}{2}\,, \tag{4.12}$$

which defines the resonance mass M_r and width Γ_r, cf. Ref. [61]. The amplitude on the second

Riemann sheet reads

$$\mathcal{M}^{\mathrm{II}} = n\left[1 - \mathcal{K}\Sigma^{\mathrm{II}}\right]^{-1}\mathcal{K}n\,, \tag{4.13}$$

where the full self-energy matrix Σ^{II} is evaluated on the second Riemann sheet. To deduce physical quantities, the renormalized couplings G_k^r are necessary [88]. These couplings are calculated by evaluating residues for each resonance. Close to the resonance pole the residues can be defined as

$$\lim_{s\to s_r}(s - s_r)\mathcal{M}^{\mathrm{II}}_{kk} = -\mathcal{R}_k\,, \tag{4.14}$$

where $\mathcal{M}^{\mathrm{II}}_{kk}$ is the diagonal element of the partial-wave amplitude in channel space on the second Riemann sheet. The squared couplings are defined as the residues, which can be calculated from the amplitude using

$$(G_k^r(s))^2 \equiv \mathcal{R}_k = -\frac{1}{2\pi\mathrm{i}}\oint_{C(s_r)}\mathrm{d}s\mathcal{M}^{\mathrm{II}}_{kk}(s)\,, \tag{4.15}$$

where $C(s_r)$ is a contour chosen around the pole s_r and necessarily excludes any other non-analytic structures. Specifically, the chosen contour is a circle around the poles with a radius chosen to avoid the poles of other resonances and the branch cut itself. The physical quantities are related to the renormalized couplings as

$$\Gamma_{r\to k} = \frac{|G_k^r|^2}{M_r}\rho_k(M_r^2) \qquad \text{and} \qquad \mathcal{B}_{r\to k} = \frac{\Gamma_{r\to k}}{\Gamma_r}\,. \tag{4.16}$$

Important to note here is that $\Gamma_r = \sum_k \Gamma_{r\to k}$ is not strictly implied. The cross-section is computed by

$$\sigma_{e^+e^-\to k}(s) = \frac{1}{16\pi s}\frac{\rho_k(s)}{\rho_{e^+e^-}(s)}\frac{\mathcal{N}_k}{4}|\mathcal{M}_{e^+e^-,k}|^2\,, \tag{4.17}$$

where $\mathcal{N}_k = 2l_k + 1$ is a factor taking into account the final-state angular momentum and the factor 4 respects the initial-state spin configurations.

Resonances In this analysis we study the $\psi(3770)$ resonance within the $e^+e^- \to c\bar{c}$ spectrum. Consequently, all occurring resonances have the quantum numbers of the photon, $J^{PC} = 1^{--}$, where J is the total angular momentum, P is the symmetry factor under space inversion and C is the symmetry under charge conjugation. Focusing on the $\psi(3770)$, we restrict the energy range of our investigation to $4M^2_{D^0} < s < (M_D + M_{D^*})^2$, which is slightly above the first two narrow resonances, J/ψ and $\psi(2S)$, and is below most other broad resonances in the spectrum. This region is dominated by the $\psi(3770)$ resonance. Various other studies [75, 85] found that the closest lower-lying resonance has a major effect on the shape of the next higher-lying resonance, such that the $\psi(2S)$ is included into the analysis to improve the description of the shape of the $\psi(3770)$ resonance, resulting in:

$$r \in \{\psi(2S), \psi(3770)\} \qquad \text{and} \qquad N_R = 2\,. \tag{4.18}$$

Channels In the energy range of $4M_{D^0}^2 < s < (M_D + M_{D^*})^2$ the dominant channels for the K-matrix ansatz are:

- $e^+e^- \to \text{non-}D\bar{D}$,
- $e^+e^- \to D^+D^-$,
- $e^+e^- \to D^0\bar{D}^0$.

It is well known [61, 89] that there is a non-negligible contribution of non-two-body states in this energy range, which is problematic since our K-matrix ansatz fundamentally only models two-body final states. In fact, a dominant amount of non-two-body final states only occurs for the decay width of the $\psi(2S)$. Therefore, some assumptions are necessary for this analysis:

- We model the effects of the $\psi(2S)$ on the line shape of the $\psi(3770)$ by an effective P-wave channel within the K-matrix model, $\text{eff}_{\psi(2S)}$, with a threshold of $4M_\pi^2$. At this point, only the rough value of $\text{eff}_{\psi(2S)}$ is of interest, since the line shape of the $\psi(3770)$ resonance is rather unaffected by the exact value of $\text{eff}_{\psi(2S)}$ and we do not aim to describe the line shape of the $\psi(2S)$. Specifically, the interference effects of a lower-lying resonance dominates the effect on the line shape of the $\psi(3770)$ compared to the exact properties of this resonance, as long as this resonance is far below the energy range under investigation.
- The $\psi(3770)$ resonance is allowed to decay to non-$D\bar{D}$ contributions. These non-$D\bar{D}$ contributions are implemented as an effective P-wave channel $\text{eff}_{\psi(3770)}$ within the K-matrix model with a threshold of $4M_\pi^2$.
- The effective channels $\text{eff}_{\psi(2S)}$ and $\text{eff}_{\psi(2S)}$ are either considered to be identical, such that $\text{eff}_\psi = \text{eff}_{\psi(3770)} = \text{eff}_{\psi(2S)}$, allowing them to interfere, or they are treated as distinct and do not interfere.
- In the energy range of interest the data is dominated by D^+D^- and $D^0\bar{D}^0$ states, which will be modeled as two-body P-wave states within the K-matrix.
- In all cross sections in this analysis the resonances couple to e^+e^-. In the K-matrix formalism this is taken into account as an additional S-wave e^+e^- channel, which leads to an intrinsic accounting of the e^+e^- vacuum polarization to the open-charm spectrum. Since the e^+e^- channel is also the production channel of any cross section taken into account, one could also think of using a P-vector approach [23, 61] for this analysis, but it turns out to make no numerically significant difference.

These assumptions result in two different numbers of channels with either interference or no-interference in the non-$D\bar{D}$ final states. One result comes with the number of channels $N_c = 5$

$$k \in \left\{ e^+e^-, D^+D^-, D^0\bar{D}^0, \text{eff}_{\psi(3770)}, \text{eff}_{\psi(2S)} \right\} , \tag{4.19}$$

and the other one comes with $N_c = 4$

$$k \in \left\{ e^+e^-, D^+D^-, D^0\bar{D}^0, \text{eff}_\psi \right\} . \tag{4.20}$$

4.3.1 Data

In the desired energy range different collaborations from different experiments have collected data on $e^+e^- \to$ hadrons, namely BaBar [90], Belle [91], BES [69], BESII [70], BESIII [71], and CLEO [92]. These data sets can be divided by the two fundamentally different methods used to measure the cross sections:

- First, the *energy scan* method is used by BES, BESII, BESIII and CLEO. It consists of an experimental setup using e^+e^- collisions, where the center-of-mass energy $\sqrt{s}$ is set to a certain value. The data is taken for a reasonable long period of time on that energy value such that a high resolution data point is measured. Usually, these data has a bin width of roughly less than 10 MeV uncertainty and is, therefore, treated as data bins with vanishing widths throughout this analysis.
- Second, the method of *initial-state radiation* is used by the BaBar and Belle experiments. Both experiments work with e^+e^- at a center-of-mass energy of roughly 10 GeV and access the energy range of interest by radiating off an energetic photon in a continuous spectrum. By that, they do not gather as much data at a certain energy but integrate the data over a reasonable energy range.

Here, only the measurements of BES, BESII, BESIII are used. This is, because on the one hand, these measurements are based on far larger data sets than the CLEO measurement. On the other hand, the BES, BESII, BESIII measurements have a far better quality — in the sense of energy resolution — than the BaBar and Belle measurements. Moreover, this analysis differentiates between *inclusive* and *exclusive* data, where *inclusive* refers to the ratio $R = \sigma(e^+e^- \to \text{hadrons})/\sigma(e^+e^- \to \mu^+\mu^-)$ and *exclusive* refers to data on an explicit final state $e^+e^- \to D^0\bar{D}^0$ or $e^+e^- \to D^+D^-$. A crucial point of this analysis is that taking the exclusive data into account makes the results sensitive to isospin symmetry breaking. To reduce the influence of the spectrum of higher-lying resonances than the energy range of interest, the data taken into account is limited to data points up to 3.83 GeV. Therefore in this analysis the following data is included:

- *inclusive.* There are 12 and 60 + 1 data points from BES [69] and BESII [70, 93], respectively, which are referred to as BES 2002, BESII 2006A and BESII 2006B in this analysis.
- *exclusive.* There are 26 and 27 data points from a preliminary BESIII analysis [94] that is referred to as BESIII 2017. This analysis is not accounting for small systematic correlations between both $D\bar{D}$ final states. Moreover, the data points are given as an observed cross section σ^{obs} and needs to be converted to the born cross section σ^{B} to be comparable to the *inclusive* data. This can be done via [95]

$$\sigma^{\text{B}}(E) = \sigma^{\text{obs}}(E)\frac{|1-\Pi(E)|^2}{1+\delta(E)}\,, \tag{4.21}$$

  which depends on the vacuum polarization $\Pi(E)$ and a radiative correction which accounts for the initial-state radiation $\delta(E)$. Final-state radiation effects are neglected in Eq. (4.21) since the final-state D-mesons are far heavier than the initial e^+e^- state.

In total this sums up to 126 data points taken at different times of the experiments such that the data sets are statistically independent of one another. The systematic uncertainties are given in the corresponding publications such that in this analysis the full correlation matrix can be used by separating the energy independent from the energy dependent systematic uncertainties.

In this analysis, by the large amount of free parameters, it is necessary to ensure convergence of the fit by adding additional constraints. On the one hand, the value of the inclusive cross section, the R-ratio, below the $c\bar{c}$-threshold is kept fixed at a value of $R_{uds} = 2.171$ [96]. On the other hand, the R-ratio above — sufficiently enough to be saturated — the $c\bar{c}$-threshold is limited to $R_{udsc} = 3.55$ [96]. The fit implements the upper threshold by a penalty function

$$-2 \log P \supseteq \frac{(r - 3.55)^2}{\sigma^2} \theta(r - 3.55) \,, \tag{4.22}$$

where $r = R(\sqrt{s} = 9\,\text{GeV})$ represents the R-ratio value below the first $b\bar{b}$ resonance. Here, $\sigma = 10\,\%$ accounts for the theoretical uncertainty of the R-ratio and θ is the Heaviside function. Moreover, as the $\psi(2S)$ resonance is not included in the region of interest but brings a valuable constraint to improve on the convergence of the fit to data, the width $\Gamma_{\psi(2S)\to e^+e^-}$ is constrained to $\Gamma_{\psi(2S)\to e^+e^-} = (2.33 \pm 0.04)\,\text{keV}$, cf. Ref. [61]. In total, the fit does not aim to describe these parameters and it is not necessary for these parameters to be exact, rather they are included to keep the fit model on physical terms.

4.3.2 Analysis

In this analysis, Bayesian inference is extensively used, which is introduced in Sec. 2.8. Here, the posterior probability density function (PDF) is

$$P(\vartheta|D, M) = \frac{P(D, M|\vartheta) P_0(\vartheta|M)}{Z(D, M)} \,, \tag{4.23}$$

where $Z(D, M)$ is called the evidence, $P_0(\vartheta|M)$ is the prior PDF, and the likelihood is $P(D, M|\vartheta)$. D refers to the various data sets as described in Sec. 4.3.1 and M refers to the different fit models, which are explained in the following. The different models consist of sets of fit parameters, as introduced in Sec. 4.3, namely:

masses. The mass of the $\psi(2S)$ is fixed at the value of the world average at $M_{\psi(2S)} = 3.6861\,\text{GeV}$ [61]. The mass of the $\psi(3770)$ is a fit parameter.

couplings. The bare couplings, introduced in Eq. (4.11), of the resonances $\psi(2S)$ and $\psi(3770)$ to the channels in Eq. (4.19) or Eq. (4.20). In the first case the resonances couple to their distinct effective decay channel. In the second case the resonances couple to the same effective decay channel and, thus, might interfere. In both cases the amount of free fit parameters is eight.

background terms. The background terms in Eq. (4.11) are fit parameters, where only the background terms for the process $e^+e^- \to \{D^+D^-, D^0\bar{D}^0\}$ are taken into account, which amounts to two fit parameters.

momentum scale. Another fit parameter is the momentum scale introduced in Eq. (4.2). Even though it is introduced as a channel-dependent quantity, it turns out that an overall momentum scale suffices to obtain good fits.

In total, all fit parameters are purely real-valued quantities by construction of the K-matrix, cf. Sec. 4.3. The likelihood and, therefore, the posterior PDF, defined in Eq. (4.23), as well as the prior ranges, are dependent on some symmetries of the aforementioned parameters:

- When the effective channel is made specific for one resonance only and there is no background constant involved in the model, then the posterior PDF is independent on the sign of the effective couplings to these channels. When the resonances couple to a single effective channel instead of resonance specific ones, then the posterior PDF is dependent of the sign of the effective couplings. By convenience for this analysis a positive sign for the effective coupling of the $\psi(3770)$ resonance is chosen.
- The posterior PDF is independent of the overall sign of the full set of couplings of a certain resonance r. This implies that one can fix a single coupling of the g_k^r for each resonance r. Here, it is chosen that all $g^r_{e^+e^-}$ shall be positive.
- Changing the overall sign of all bare couplings to a certain channel k does not affect the posterior PDF. This implies that the sign for a single coupling g_k^r for each channel k can be fixed. Here, all the couplings $g_k^{\psi(3770)}$ are chosen to be positive.

Ultimately, the prior PDF in Eq. (4.23) is built up by a product of uniformly distributed PDFs for each parameter. In this analysis, the following fit models are compared with each other:

minimal. The $\psi(3770)$ bare mass parameter and 7 bare couplings for the channels in Eq. (4.19), where the effective coupling $\text{eff}_{\psi(3770)}$ is fixed to zero. By that, in this model, there is no contribution of the $\psi(3770)$ to non-$D\bar{D}$. In total this accounts for 8 fit parameters.

no background. Additionally to the minimal fit model $\text{eff}_{\psi(3770)}$ is a fit parameter and contributions of the $\psi(3770)$ to non-$D\bar{D}$ are allowed. In total this accounts for 9 fit parameters.

background. Additionally to the no background fit model the constant background parameter in each off-diagonal K-Matrix entries for the processes $e^+e^- \to D\bar{D}$ are allowed. In total this accounts for 11 fit parameters.

q_0 *variation.* Additionally to the background fit model the *momentum scale* q_0 is a fit parameter. In total this accounts for 12 fit parameters.

interference. Analogous to the background model, but the resonances $\psi(2S)$ and $\psi(3770)$ are allowed to interfere by coupling to the same effective channel as introduced in Eq. (4.20). In total this accounts 11 fit parameters.

This analysis uses the EOS software package [40] in version 1.0.11 [72] to optimize the posterior PDF, cf. Eq. (4.23), and deduce a best-fit point or several best-fit points. All experimental data enters the fit as a Gaussian likelihood, which makes the global χ^2 value a useful and valid statistic.

Using importance samples, posterior-predictive distributions of observables can be computed, where the fit can either depend on the observable in the likelihood or the observable can be fully predicted by the distribution. To produce the importance samples, EOS uses the dynamical nested sampling algorithm [97] by interfacing with the dynesty software package [98, 99]. By using dynamical nested sampling, one can achieve a direct comparison of two models, M_1 and M_2, for the same data set D by the Bayes factor

$$B(M_2, M_1) \equiv \frac{Z(D|M_2)}{Z(D|M_1)}\,. \tag{4.24}$$

When the Bayes factor is larger than 1, model M_2 is favored over model M_1. A more intuitive interpretation of the Bayes factor is given by Jeffreys [38].

The pole position of the $\psi(3770)$ in the complex plane is a crucial result of the K-matrix formalism. To determine this pole position, a root finding procedure is used for $\det[1 - \mathcal{K}\Sigma^{\mathrm{II}}]$. The uncertainty of the pole position is estimated by finding the root for each sample created by the nested sampling algorithm. To test the viability of the numerical implementation of this analysis three cross-checks are performed:

- The K-matrix formalism used for this analysis respects the unitarity of the S-matrix. Therefore, the partial decay widths ought to sum up to the total decay width within the obtained uncertainties.
- The residues of the resonance poles are dominated by short-distance interactions, therefore they are expected to factorize according to

$$-\frac{1}{2\pi\mathrm{i}} \oint_{C(s_r)} \mathcal{M}^{\mathrm{II}}_{ab}(s)\mathrm{d}s = G^r_a \times G^r_b\,, \tag{4.25}$$

  where the G^r_i are extracted from $\mathcal{M}^{\mathrm{II}}_{ij}(s)$ using Eq. (4.15).
- The spectral function of the $\psi(3770)$ as in Ref. [100, chapter 10.7]

$$\mathrm{spect}_{\psi(3770)}(s) = -\frac{1}{\pi} \times \mathrm{Im}\left[\frac{1}{s - m^2_{\psi(3770)} + \Sigma\left(g_k^{\psi(3770)}\right)^2 \Sigma_k(s)}\right] \tag{4.26}$$

  must fulfill

$$\int_{s_{\mathrm{th}}}^{\infty} \mathrm{spect}_{\psi(3770)}(s)\mathrm{d}s = 1\,, \tag{4.27}$$

  where s_{th} is the first threshold occurring in the spectrum.

These tests are meant as causal cross-checks for the numerical implementation of this analysis. They can only be applied after the full analysis is done since any modification in between could implicitly implement the checks themselves. Furthermore, only after the analysis is done all the information is available to truthfully check the above conditions. Any strong violation of these tests indicates an error during the implementation.

Model	χ^2	d.o.f.	p [%]	log(Z)	M [MeV]	Γ [MeV]	$\mathcal{B}_{\text{non}-D\bar{D}}$ [%]
minimal	120	119	46.0	82.0	3779.0 ± 0.3	23.5 ± 0.4	—
no backgr.	120	118	44.0	79.0	3778.9 ± 0.3	23.6 ± 0.4	< 6.1
backgr.	107	116	71.8	81.7	3778.8 ± 0.3	25.0 ± 0.5	< 5.8
q_0 variation	106	115	71.8	69.3	3778.8 ± 0.3	24.6 ± 0.6	< 5.0
interference	107	116	71.5	80.5	3778.8 ± 0.3	25.0 ± 0.5	< 6.1

Table 4.3: Results of the analysis for each model as named in the main text. The resulting χ^2, the total degrees of freedom, the p-value and the logarithmic evidence are given, as well as the estimated mass and width of the $\psi(3770)$ resonance. The branching ratio to non-$D\bar{D}$ states is given at 90 % probability.

4.4 Results

In total five analyses are performed for the five different models. All five analyses under investigation do fulfill the checks described at the end of Sec. 4.3.2 and the fits reach a p-value of above 3 %. In Table 4.3 the results of the analyses are given, namely the total χ^2, the p-value and the $\psi(3770)$ resonance mass and width.

Already the minimal fit model gives an outstanding p-value of 46 %. The analyses with distinct effective channels for the $\psi(3770)$ resonance are compared. After that, the resulting nominal fit model is compared to the "interference" model. The "no background" model is of similar quality as the "minimal" model in terms of χ^2 and p-value. Though, the Bayes factor excludes the "no background" model as a good model as it results in $\approx 1/20$, which according to Jeffrey's interpretation of the Bayes factor *strongly* disfavors the "no background" model over the "minimal" model. As Table 4.3 shows, the "background" model improves the χ^2 by 13 using 3 more parameters. Therefore, the "background" model is as efficient in describing the data as the "minimal" model with a Bayes factor of ≈ 0.7 and increases the likelihood-ratio test result by 3σ in contrast to the "no background" model. For the "q_0 variation" model one sees a similar decrease in χ^2 value as compared to the "no background" model. However, the "q_0 variation" model is disfavored *decisively* in terms of Jeffrey's interpretation of the Bayes factor with a factor of $3 \cdot 10^{-6}$ with respect to the "minimal" model.

Thus, the "background" model is considered as the "nominal" fit model, in case of no interference, in the following. The "interference" model is of similar fit quality as the "background" model, as can be seen from Table 4.3. In terms of the Bayes factor it is slightly less efficient in describing the data compared to the "background" model. The Bayes factor of the two results in ≈ 3.3 is favoring the "background" model over the "interference" model. According to Jeffrey's interpretation of the Bayes factor this favor is *barely worth mentioning*. Both models give an equivalent description of the data, even though they differentiate drastically in the physics they describe. On the one hand, the "no background" model describing the case where the non-$D\bar{D}$ decay channels are all distinct and the interference between both resonances is non-existent. On the other hand, the "interference" model describing the case where the non-$D\bar{D}$ decay channels are all the same channel and the interference between both resonances is allowed. To further investigate the matter — if the difference in fit quality could be even more distinct — one would need to fit to each of the non-$D\bar{D}$ decay channels individually instead of only one collected effective channel for the non-$D\bar{D}$

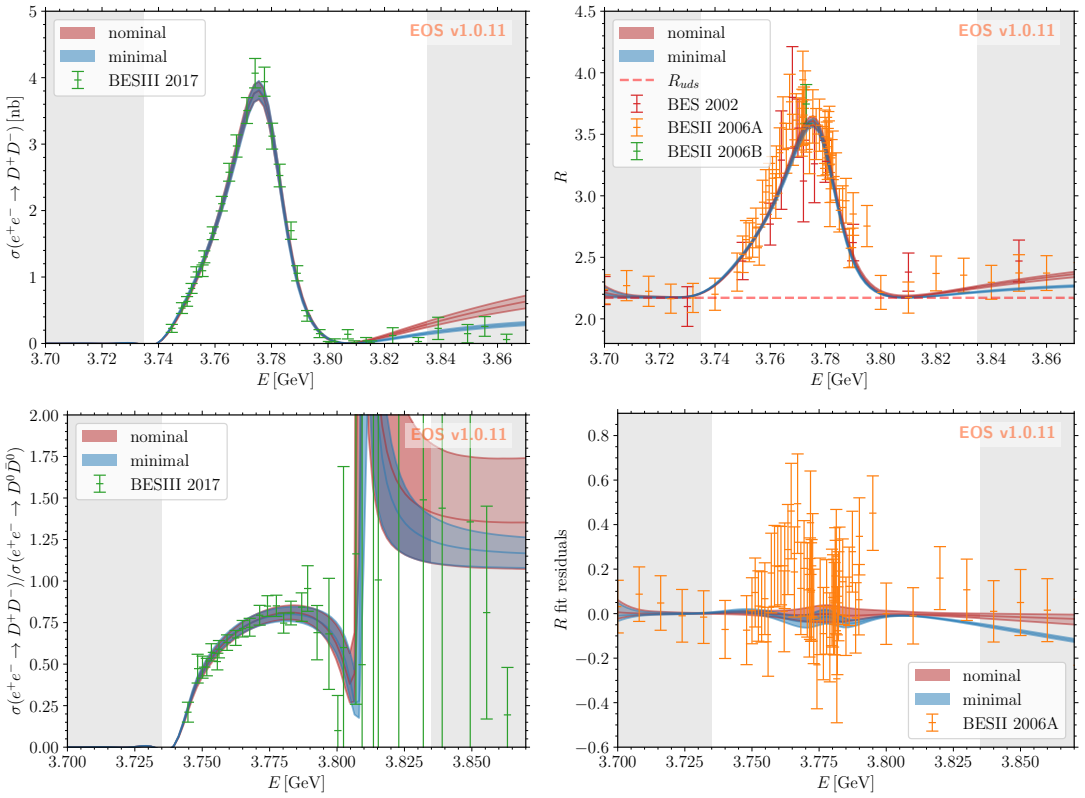

Figure 4.1: Results for some of the observables within the minimal and nominal fit models. The background and interference models are not shown here, since they have visually indistinguishable results. The used data is shown in the plots for comparison. Data in the grayed areas is not used in the fit.
Top left: Cross-section of $e^+e^- \to D^+D^-$ scattering; compared to the BESIII 2017 exclusive data. *Top right:* R-ratio; compared to the BES 2002, BESII 2006A and BESII 2006B data sets. The dashed line shows R_{uds}, which serves as a baseline in this context. *Bottom left:* Ratio of the cross-sections of $e^+e^- \to D^+D^-$ and $e^+e^- \to D^0\bar{D}^0$; compared to the BESIII 2017 data. The data points and uncertainties shown here are derived from the actual BESIII 2017 data; they neglect the correlations between the D^+D^- and $D^0\bar{D}^0$ data, as those originate from the same experimental runs. Therefore, the data serves purely illustrative purposes here. *Bottom right:* Residuals of the fit of the R-ratio to BESII 2006A data. The R-ratio from the nominal fit result is subtracted from the data, the R-ratio from the minimal model and from itself (which equals 0 within its uncertainties).

contributions. For both models the posterior samples result in a nearly Gaussian distribution and pass all viability tests discussed in Sec. 4.3.2.

The predictions for the "minimal" and "nominal/background" model are presented in Fig. 4.1. The first row of figures in Fig. 4.1 shows a comparison of the fit results with the experimental data. On the upper-left panel the cross section and on the upper-right panel the R-ratio is shown. The data in the grayed zone lies outside the fit region and is not included in the fit. The bottom-left panel shows the ratio of the cross-sections of $e^+e^- \to D^+D^-$ and $e^+e^- \to D^0\bar{D}^0$. The bottom-right

panel shows the residuals of the R-ratio, which is produced by subtracting the R-ratio line shape, resulting from the "nominal/background" fit, from the data as well as the predictions of the models, in the region of the $\psi(3770)$ resonance. These residuals have previously lead to the interpretation of the $\psi(3770)$ resonance as a double pole in [73]. In contrast, this analysis can fully explain the data by the interference of the $\psi(2S)$ and $\psi(3770)$. In contrast to [74], the results of this analysis are drastically different. In [74] the results are strongly dependent on a vertex function introducing a cutoff Λ, where it is stated that *the parameter is as important as any other parameter of the fit model*. The cutoff Λ is given with an accuracy of $< 1\%$ in the final result. In the analysis presented here, a similar parameter is introduced in the q_0 model. However, for our model the importance of the parameter q_0 is negligible. Moreover, [74] finds an accompanying pole to their result for the $\psi(3770)$, which is, as stated there, quite surprising. In our analysis, no further pole is needed, as the $\psi(2S)$ fully explains the line shape of the $\psi(3770)$ resonance in relation to the available data.

In case of both the "nominal/background" model and the "interference" model the same mass and width for the $\psi(3770)$ are obtained:

$$\begin{aligned} M_{\psi(3770)} &= 3778.8 \pm 0.3\,\text{MeV}\,, \\ \Gamma_{\psi(3770)} &= 25.0 \pm 0.5\,\text{MeV}\,. \end{aligned} \tag{4.28}$$

These resonance parameters are compatible with the results of [74]:

$$\begin{aligned} M^{[74]}_{\psi(3770)} &= 3777.0 \pm 1.0\,\text{MeV}\,, \\ \Gamma^{[74]}_{\psi(3770)} &= 24.6 \pm 1.0\,\text{MeV}\,. \end{aligned} \tag{4.29}$$

Considering the different approaches to model the physics beyond the $\psi(3770)$ resonance of this analysis and the analysis performed in [74] — as explained previously — it is a good validation for both results that they coincide within their uncertainties. Moreover, the models used in [61, 74, 75] are vastly different in their underlying approaches. While here, the K-matrix approach is used, most analyses use the Breit–Wigner approach. Therefore, the models should not be expected to extract identical information about the physical observables. Still, the results presented here are compatible with most literature as:

$$\begin{aligned} M^{[75]}_{\psi(3770)} &= 3779.8 \pm 0.6\,\text{MeV}\,, \\ \Gamma^{[75]}_{\psi(3770)} &= 25.8 \pm 1.3\,\text{MeV}\,, \end{aligned} \tag{4.30}$$

and

$$\begin{aligned} M^{[61]}_{\psi(3770)} &= 3778.1 \pm 0.7\,\text{MeV}\,, \\ \Gamma^{[61]}_{\psi(3770)} &= 27.5 \pm 0.9\,\text{MeV}\,. \end{aligned} \tag{4.31}$$

The simultaneous analysis of exclusive and inclusive data, as done here, is of great interest throughout the literature [75, 101–104]. It allows to estimate the branching ratio of non-$D\bar{D}$ in $\psi(3770)$ final states. The results of this analysis are summarized in the last row of Table 4.3. The

"nominal/background" and "interference" models are quite similar and roughly

$$\mathcal{B}(\psi(3770)\to\text{non-}D\bar{D}) < 6\% \text{ at } 90\% \text{ probability}\,. \tag{4.32}$$

In Fig. 4.2 this result is compared to the results of [75, 101–104]. It shows that Eq. (4.32) is systematically lower than most other results with the exception of [104]. Interestingly, exchanging the exclusive Born cross section for the exclusive observed cross section seems to enhance the non-$D\bar{D}$ contribution to levels of about $\approx 20\%$. As mentioned before, this analysis is also sensitive to isospin symmetry breaking. Since the $\psi(3770)$ resonance lies just slightly above the thresholds of $D^0\bar{D}^0$ at $\approx 3.730\,\text{GeV}$ center-of-mass energy and D^+D^- at $\approx 3.739\,\text{GeV}$, the rapid increase in phase space volume for both channels, just above the threshold region, plays a crucial role for the shape of the close-by resonance. At first sight, this leads to a sizable difference in cross sections, which is depicted in the bottom left panel of Fig. 4.1 as a ratio of both cross sections. Looking at parameters free of distortions by different phase space volumes one can compare the bare couplings of the $\psi(3770)$ resonance to both channels, as both are available in the K-matrix approach. The ratio of the bare couplings results in

$$g^{\psi(3770)}_{D^0\bar{D}^0}/g^{\psi(3770)}_{D^+D^-} = 0.99 \pm 0.03\,, \tag{4.33}$$

which agrees with unity within its uncertainties. This is interpreted as an unbroken isospin symmetry. Moreover, any deviation from isospin symmetry could only appear suppressed by orders of α_e or the mass difference $(m_u - m_d)/m_s$, which is not seen here. There is a sizable discrepancy of Eq. (4.33) to previous literature [94, 105], although it is compatible with the prediction of [74]. Moreover, within this analysis it is possible to predict the ratio of the $\psi(2S)$ resonance coupling to the $D\bar{D}$ channels, which results in a ratio of 1.02 ± 0.10. This ratio is again compatible with isospin symmetry, however, the uncertainty is notably larger since the $\psi(2S)$ resonance is not fully included in the models applied here.

4.5 Relations to non-local form factors in $b \to s\ell^+\ell^-$

One of the motivations for studying the $e^+e^- \to c\bar{c}$ process is to extract information regarding the 1^{--} charmonium resonances. This information is crucial for enhancing our understanding of the $b \to s\ell^+\ell^-$ transition. Moreover, non-local hadronic matrix elements in $b \to s\ell^+\ell^-$ are of great interest throughout the flavor physics community [106–112], since the relatively large uncertainties allow for significant improvements in their theoretical predictions [113]. As a prime example for such a transition the $\bar{B} \to \bar{K}\ell^+\ell^-$ process comes to mind. The dominant non-local contribution to the amplitude is

$$\mathcal{H}^\mu = \mathrm{i}\int d^4x\, e^{\mathrm{i}q\cdot x}\,\langle \bar{K}(k)|\,T\left\{\bar{c}\gamma^\mu c(x), \sum_i C_i O_i(0)\right\}|\bar{B}(q+k)\rangle\,, \tag{4.34}$$

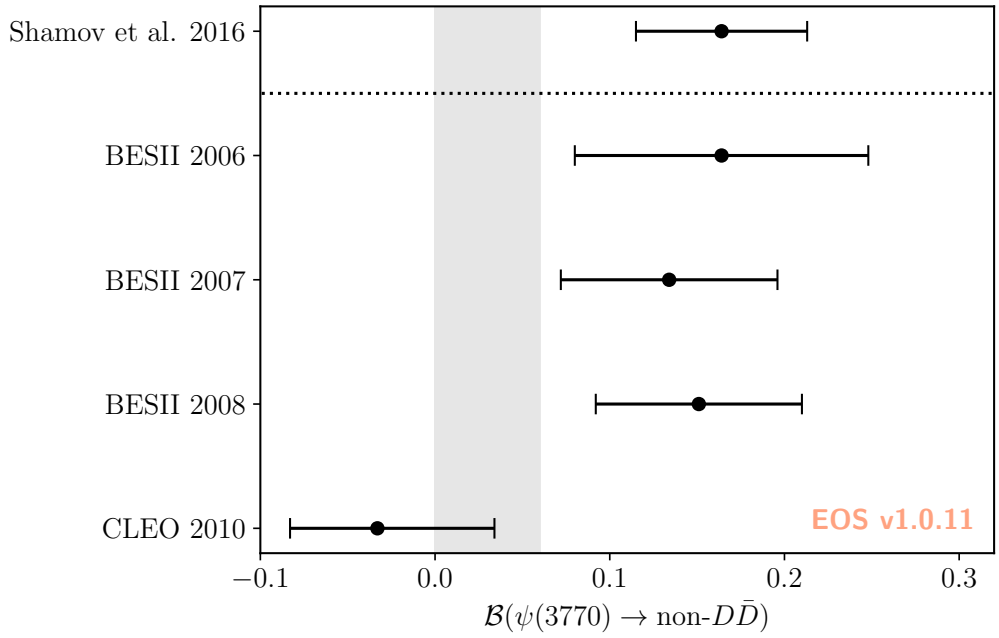

Figure 4.2: Comparison of our nominal result on the branching ratio $\mathcal{BR}(\psi(3770) \to \text{non-}D\bar{D})$. The grey band shows our nominal result at 90% probability. Above the dashed line the comparison between our result and the phenomenological literature [75] and below the dashed line to the experimental literature [101–104] is shown. Note here, that the 3 BESII results are not statistically independent.

where C_i are the Wilson coefficients and O_i are a set of dimension-six operators with

$$O_i = \left[\bar{s}\Gamma_i b\right]\left[\bar{c}\tilde{\Gamma}_i c\right] , \tag{4.35}$$

where Γ_i and $\tilde{\Gamma}_i$ are the combined Dirac and color structures. Usually, these hadronic matrix elements are discussed in terms of their scalar-valued non-local form factors

$$\mathcal{H}_\lambda(q^2) = P^\mu_\lambda \mathcal{H}_\mu(q) , \tag{4.36}$$

where $\lambda = 0, \pm 1$ are the polarizations of the virtual photon and P^μ_λ are suitable projectors, cf. Ref. [112]. Note here that the $\mathcal{H}_\lambda(q^2)$ are complex valued functions even below threshold, since the $\bar{B}$ meson decay can produce on-shell hadronic states through the four-quark operators, cf. Ref. [106]. The amplitudes $\mathcal{H}_\lambda(q^2)$ are well described in Refs. [110–112] for $q^2 < 4M_D^2$. In this work, we focus on the open-charm region in $q^2 \geq 4M_D^2$. In this phase-space region of open-charm spectrum, an OPE ansatz for the time-ordered product is common, see Refs. [114, 115]. Also, a Breit–Wigner model of the broad resonances in the charmonium spectrum of this energy region is a commonly used description, cf. Refs. [116–118]. Here, we use a more analytic approach. Starting with crossing symmetry, the decay amplitude can be related to the scattering amplitude

$\bar{B}K \to e^+e^-$

$$\mathcal{A}_{\bar{B}K,e^+e^-} \propto \sum_{\lambda} L_\mu P_\lambda^{\mu *} \mathcal{H}_\lambda(q^2)\,, \tag{4.37}$$

where $L_\mu = \bar{u}_\ell \gamma_\mu v_\ell$ is the leptonic current. Equivalently, the amplitude for $\bar{B} \to \bar{K} D\bar{D}$ decays can be related to the scattering amplitudes $\bar{B}K \to D\bar{D}$. Note here that the $D\bar{D}$ final state couples to e^+e^- predominantly in a P-wave configuration. To describe such production amplitudes of $\bar{B}K \to D\bar{D}$ the P-vector approach is conveniently chosen [23, 119, 120], which is based on the results of the K-matrix model from the main part of this chapter. The amplitude in the P-vector approach is parametrized as

$$\mathcal{A}_{\bar{B}K,a} = n_a \left[1 - K\Sigma\right]^{-1} P_{\bar{B}K}(s)\,, \tag{4.38}$$

where n_a are the same phase-space contributions as in Eq. (4.2) and $P_{\bar{B}K}(s)$ is referred to as the source term, with

$$P_{\bar{B}K}(s) = \sum_{r}^{N_R} \frac{\alpha^r g^r_{\bar{B}K}}{m_r^2 - s} + b_{\bar{B}K}\,. \tag{4.39}$$

Here, the first part is a sum over the resonances — the same resonances as used in the K-matrix model — and the second part is a background term $b_{\bar{B}K}$, which accounts for the non-resonant transitions from the source term to the final-state channel. Moreover, the coupling to each of the resonances is accompanied by a strength factor α^r. When combined with a successful K-matrix description of the complete $e^+e^- \to$ open-charm spectrum the physical quantities can be extracted similarly to the K-matrix approach using Eq. (4.15) and Eq. (4.16).

4.6 Summary and outlook

In this chapter, a coupled-channel analysis of the $e^+e^- \to c\bar{c}$ spectrum in the region of the $\psi(3770)$ resonance was performed. For this purpose, five models based on the K-matrix formalism were used. In the end, the available data of BES, BESII and BESIII are well described within these models. There are no signs of a significant branching ratio of the $\psi(3770)$ resonance to non-$D\bar{D}$ final states. In the model allowing for interference between the $\psi(2S)$ and the $\psi(3770)$ resonance the upper bound for the branching ratio to non-$D\bar{D}$ final states is found to be

$$\mathcal{B}(\psi(3770) \to \text{non-}D\bar{D}) < 6\% \text{ at } 90\% \text{ probability}\,. \tag{4.40}$$

This is systematically smaller but compatible with almost all other analyses of this observable. There have been suggestions of various exotic states beyond the quark model in the vector resonance spectrum; see for example, Refs. [77–82]. The results presented here emphasize the $c\bar{c}$ nature and give no implications about further exotic qualities of the $\psi(3770)$ resonance. In this near-threshold analysis, hadronic loops, which might give rise to hadronic molecules [80], are suppressed due to their P-wave nature.

Although, hadronic loops, which e.g. might induce the existence of hadronic molecules [80], are suppressed in this analysis. Here, we work close to threshold, where possible hadronic loops would

be suppressed by their P-wave nature.

Throughout this analysis, external determinations of the partial branching ratio $\Gamma(\psi(2S) \to e^+e^-)$ were used. A more consistent analysis could be performed with more data of $e^+e^- \to \mu^+\mu^-$ in the region of interest around the $\psi(3770)$ resonance. Currently, this is not available at a useful precision.

Future work in this field would include the extension to higher center-of-mass energies $\sqrt{s}$ to include more resonances and final-state channels. Ultimately, the extracted line shape of the $e^+e^- \to$ hadrons cross section will be valuable input for theoretical predictions of the exclusive decay $b \to s\ell^+\ell^-$. However, wether an application of this matter will be useful strongly depends on future data released.

CHAPTER 5

Summary

In this thesis we have applied different analyticity and unitarity constraints in context of two major projects, which aim to deepen our understanding of the flavor sector of modern particle physics.

First, we used a fully dispersive ansatz to relate the $B \to \gamma^*$ form factors, occurring in $B^- \to \ell^- \bar{\nu}_\ell \ell'^- \ell'^+$ decays, to the well-established $B \to \rho$ and $B \to \omega$ form factors within a VMD model. To achieve this relation we have carefully revisited the parametrization of the $B \to \gamma^*$ form factors by developing a parametrization completely free of kinematic singularities. Furthermore, we give explicit predictions for the branching ratios and forward–backward asymmetries of the different possible final states in Table 3.5.

Moreover, we have provided a version of the formalism with a subtraction in the dispersive integrals relating the $B \to \gamma^*$ to $B \to \rho$ and $B \to \omega$ form factors. This additional subtraction is not strictly necessary but extrapolates the formalism from the region of timelike photon momentum to the spacelike region. By suppressing soft contributions close to $q^2 \gtrsim 0$, the predictive power can be further improved. This new subtracted formulation will be beneficial for future analyses of this process.

Second, we have successfully described the $\psi(3770)$ resonance by developing a fully analytic K-matrix formalism based on analyticity and unitarity of the S-matrix. By analytically continuing the occurring phase-space volumes, we were able to compute the resonance parameters based on the extraction of the pole parameters on the second Riemann sheet of the S-matrix amplitudes. We find a branching ratio of

$$\mathcal{B}(\psi(3770) \to \text{non-}D\bar{D}) < 6\% \text{ at } 90\% \text{ probability}$$

and resonance parameters of

$$\begin{aligned} M_{\psi(3770)} &= 3778.8 \pm 0.3\,\text{MeV}\,, \\ \Gamma_{\psi(3770)} &= 25.0 \pm 0.5\,\text{MeV}\,. \end{aligned}$$

While our findings implement unitarity on a fundamental level, they are widely compatible with results of previous literature. Our ansatz can be systematically extended to include further

resonances with presumably higher masses and possibly greater widths, as well as more final-state channels; an ansatz that is of great interest to better describe the open charm spectrum. Moreover, the inclusion of more resonances and final-state channels would naturally influence the resonance parameters of the $\psi(3770)$ resonance within this coupled-channel approach.

The analytic results discussed in this thesis are fully implemented and have been published within the EOS software package [72]. Furthermore, the numerical analyses throughout this research were performed using the EOS software package.

Both projects within this thesis provide crucial initial steps toward further analyses on the subjects of B anomalies. In $B^- \to \ell^- \bar{\nu}_\ell \ell'^- \ell'^+$ decays, important corrections to former analyses were performed and a well-founded parametrization for the relevant matrix elements was provided to the community, cf. Section 3.11. The fundamental $\psi(3770)$ resonance was well-described within a coupled-channel formalism, which leads to essential insights on the complex $e^+e^- \to c\bar{c}$ spectrum. In context of $b \to s\ell^+\ell^-$ this analysis provides a foundation to build further analyses upon, cf. Section 4.6, especially by providing an easy-to-use implementation within the EOS software package.

APPENDIX A

Kinematics of the decay $B^- \to \ell^- \bar{\nu}_\ell \ell'^- \ell'^+$

A.1 Cascade-like interpretation of decays

In this chapter, we explain how to approach a multi-body final-state decay and how to compute the physical observable of a decay. To calculate observables in flavor physics the Lorentz invariant phase space (LIPS) is a crucial input. How to compute LIPS is discussed in more detail in App. A.3. For that, one can think about a multi-body final-state decay in a cascade way, in case of Ch. 3, the cascade is given as $B^-(P) \to \gamma^*(q)[\to \ell'^+(q_1)\ell'^-(q_2)]\, W(k)[\to \ell^-(k_2)\bar{\nu}(k_1)]$, which is pictured in Fig. A.1. This decay is commonly described by 5 independent variables, namely

- q^2, the invariant momentum squared of the virtual photon, in the ranges of $4m_{\ell'}^2 \leq q^2 \leq (M_B - m_\ell)^2$;
- k^2, the invariant momentum squared of the virtual W boson, in the ranges of $m_\ell^2 \leq k^2 \leq \left(M_B - \sqrt{q^2}\right)^2$;
- θ_W the angle between the charged lepton and the negative photon direction of flight, in the W-boson rest frame, in the ranges of $0 \leq \theta_W \leq \pi$;
- θ_γ the angle between the negatively charged lepton and the negative W-boson direction of flight, in the photon rest frame, in $0 \leq \theta_\gamma \leq \pi$;
- φ, the angle between the q^2-plane and k^2-plane, in the ranges of $0 \leq \varphi \leq 2\pi$.

As depicted in Fig. A.1 this chapter is formulated in terms of a B meson at rest. To compute any Lorentz-invariant quantity the input vectors ought to be in the same reference frame, cf. App. A.2. The 4-momenta of the intermediate particles, q for the virtual γ^* and k for the virtual W boson, in

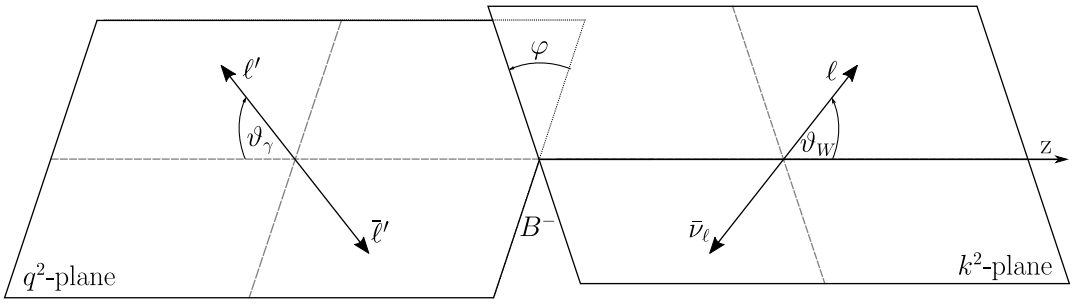

Figure A.1: Visualization of the cascade-like decay $B^- \to \ell^- \bar{\nu}_\ell \ell'^- \ell'^+$. The B meson is depicted at rest at the intersection point of both planes. The B-meson decays back-to-back into a W boson in positive z-direction and the photon in negative z-direction, which further decay back-to-back in their respective final state particles. The kinematics are described by 5 kinematic variables $\varphi, \theta_\gamma, \theta_W, q^2$ and k^2.

the B-meson rest frame are — aligned with the z-axis in Fig. A.1 — given as

$$q_{\text{BRF}} = \begin{pmatrix} q_{0,\text{BRF}} \\ 0 \\ 0 \\ q_{z,\text{BRF}} \end{pmatrix}, \qquad k_{\text{BRF}} = \begin{pmatrix} k_{0,\text{BRF}} \\ 0 \\ 0 \\ k_{z,\text{BRF}} \end{pmatrix}, \tag{A.1}$$

where

$$\begin{aligned} q_{0,\text{BRF}} &= \frac{M_B^2 + q^2 - k^2}{2M_B}, \\ q_{z,\text{BRF}} &= \frac{\sqrt{\lambda(k^2, q^2, M_B^2)}}{2M_B}, \\ k_{0,\text{BRF}} &= \frac{M_B^2 + k^2 - q^2}{2M_B}, \\ k_{z,\text{BRF}} &= -\frac{\sqrt{\lambda(k^2, q^2, M_B^2)}}{2M_B}, \end{aligned} \tag{A.2}$$

where $\lambda(k^2, q^2, M_B^2) = (k^2 - q^2 - M_B^2)^2 - 4M_B^2 q^2$ is the Källén triangle function. Notice here that $q_{z,\text{BRF}} = -k_{z,\text{BRF}}$ indicating the opposite directions of flight of both intermediate particles in the B-meson rest frame. The 4-momenta of the leptons can be conveniently defined in the rest frames

of the photon and the W boson, respectively, as

$$q_{1,\gamma\mathrm{RF}} = \begin{pmatrix} E_{\ell',\gamma\mathrm{RF}} \\ -|\vec{q}_{\gamma\mathrm{RF}}| \sin\theta_\gamma \cos\phi \\ -|\vec{q}_{\gamma\mathrm{RF}}| \sin\theta_\gamma \sin\phi \\ +|\vec{q}_{\gamma\mathrm{RF}}| \cos\theta_\gamma \end{pmatrix}, \quad q_{2,\gamma\mathrm{RF}} = \begin{pmatrix} E_{\ell',\gamma\mathrm{RF}} \\ +|\vec{q}_{\gamma\mathrm{RF}}| \sin\theta_\gamma \cos\phi \\ +|\vec{q}_{\gamma\mathrm{RF}}| \sin\theta_\gamma \sin\phi \\ -|\vec{q}_{\gamma\mathrm{RF}}| \cos\theta_\gamma \end{pmatrix}, \tag{A.3}$$

as well as

$$k_{1,\mathrm{WRF}} = \begin{pmatrix} E_{\ell,\mathrm{WRF}} \\ -|\vec{k}_{\mathrm{WRF}}| \sin\theta_W \\ 0 \\ -|\vec{k}_{\mathrm{WRF}}| \cos\theta_W \end{pmatrix}, \quad k_{2,\mathrm{WRF}} = \begin{pmatrix} E_{\nu_\ell,\mathrm{WRF}} \\ +|\vec{k}_{\mathrm{WRF}}| \sin\theta_W \\ 0 \\ +|\vec{k}_{\mathrm{WRF}}| \cos\theta_W \end{pmatrix}. \tag{A.4}$$

Here, the variables are

$$\begin{aligned} E_{\ell',\gamma\mathrm{RF}} &= \frac{\sqrt{q^2}}{2}, \quad E_{\ell,\mathrm{WRF}} = \frac{k^2 + M_\ell^2}{2\sqrt{k^2}}, \quad E_{\nu_\ell,\mathrm{WRF}} = \frac{k^2 - M_\ell^2}{2\sqrt{k^2}}, \\ |\vec{q}_{\gamma\mathrm{RF}}| &= \frac{\sqrt{q^2 - 4M_{\ell'}^2}}{2}, \quad |\vec{k}_{\mathrm{WRF}}| = \frac{k^2 - M_\ell^2}{2\sqrt{k^2}}. \end{aligned} \tag{A.5}$$

To compute the squared amplitude as in Eq. (3.43) all open Lorentz indices need to be contracted resulting in numerous scalar products of 4-vectors. Naturally, we need to find the representation of the 4-vectors in the same rest frame by applying Lorentz transformations up to twice in this case, as described in App. A.2. Here, we chose the rest frame of the W boson, which results for the vectors of the intermediate particles in

$$q_{\mathrm{WRF}} = \frac{1}{\sqrt{k^2}} \begin{pmatrix} A_{\mathrm{BRF}} \\ 0 \\ 0 \\ B_{\mathrm{BRF}} \end{pmatrix}, \quad k_{\mathrm{WRF}} = \begin{pmatrix} \sqrt{k^2} \\ 0 \\ 0 \\ 0 \end{pmatrix}, \tag{A.6}$$

where we defined $A_{\mathrm{BRF}} = k_{0,\mathrm{BRF}} \cdot q_{0,\mathrm{BRF}} - k_{z,\mathrm{BRF}} \cdot q_{z,\mathrm{BRF}}$ and $B_{\mathrm{BRF}} = k_{0,\mathrm{BRF}} \cdot q_{z,\mathrm{BRF}} - k_{z,\mathrm{BRF}} \cdot q_{0,\mathrm{BRF}}$ The vectors of the final-state particles from the photon read

$$q_{1,\mathrm{WRF}} = \frac{1}{\sqrt{k^2}\sqrt{q^2}} \times \begin{pmatrix} E_{\ell',\gamma\mathrm{RF}} A_{\mathrm{BRF}} + B_{\mathrm{BRF}} |\vec{q}_{\gamma\mathrm{RF}}| \cos\theta_\gamma \\ -\sqrt{k^2}\sqrt{q^2} |\vec{q}_{\gamma\mathrm{RF}}| \sin\theta_\gamma \cos\phi \\ -\sqrt{k^2}\sqrt{q^2} |\vec{q}_{\gamma\mathrm{RF}}| \sin\theta_\gamma \sin\phi \\ E_{\ell',\gamma\mathrm{RF}} B_{\mathrm{BRF}} + A_{\mathrm{BRF}} |\vec{q}_{\gamma\mathrm{RF}}| \cos\theta_\gamma \end{pmatrix} \tag{A.7}$$

and

$$q_{2,\mathrm{WRF}} = \frac{1}{\sqrt{k^2}\sqrt{q^2}} \times \begin{pmatrix} E_{\ell',\gamma\mathrm{RF}} A_{\mathrm{BRF}} - B_{\mathrm{BRF}} |\vec{q}_{\gamma\mathrm{RF}}| \cos\theta_\gamma \\ +\sqrt{k^2}\sqrt{q^2} |\vec{q}_{\gamma\mathrm{RF}}| \sin\theta_\gamma \cos\phi \\ +\sqrt{k^2}\sqrt{q^2} |\vec{q}_{\gamma\mathrm{RF}}| \sin\theta_\gamma \sin\phi \\ E_{\ell',\gamma\mathrm{RF}} B_{\mathrm{BRF}} - A_{\mathrm{BRF}} |\vec{q}_{\gamma\mathrm{RF}}| \cos\theta_\gamma \end{pmatrix}. \tag{A.8}$$

A.2 Lorentz boost in z-direction

Here, we discuss in detail how to perform a 4-momentum vector of a particle into its rest frame. This is needed to compute the different scalar products occurring in the computation of the $B^- \to \ell^- \bar{\nu}_\ell \ell'^- \ell'^+$ amplitude. To illustrate this we start with the 4-momentum vector of a general particle:

$$p_{\mathrm{lab}} = \begin{pmatrix} p_0 \\ 0 \\ 0 \\ p_z \end{pmatrix}, \tag{A.9}$$

where p_0 is the energy and p_z the absolute value of the 3-momentum of the particle in z-direction in some lab frame. In its rest frame this ought to be:

$$p_{\mathrm{rest}} = \begin{pmatrix} \sqrt{p^2} \\ 0 \\ 0 \\ 0 \end{pmatrix}, \tag{A.10}$$

where p^2 is its rest mass. To boost the particle from the lab frame in its rest frame we make a general ansatz for a Lorentz boost in z-direction:

$$\Lambda_{\mathrm{lab}\to\mathrm{rest}} = \begin{pmatrix} a & 0 & 0 & -b \\ 0 & 1 & 0 & 0 \\ 0 & 0 & 1 & 0 \\ -b & 0 & 0 & a \end{pmatrix}, \tag{A.11}$$

where a and b are to be determined. Using the condition:

$$\Lambda_{\mathrm{lab}\to\mathrm{rest}} \cdot p_{\mathrm{lab}} \stackrel{!}{=} p_{\mathrm{rest}}\,, \tag{A.12}$$

we get a system of equations

$$\begin{aligned} a \cdot p_0 - b \cdot p_z &= \sqrt{p^2} \\ -b \cdot p_0 + a \cdot p_z &= 0\,. \end{aligned} \tag{A.13}$$

Solving this, gives us the z-boost transformation matrix from one reference frame to another with

$$\Lambda_{\text{lab}\to\text{rest}} = \frac{\sqrt{p_0^2 - p_z^2}}{p_0^2 - p_z^2} \begin{pmatrix} p_0 & 0 & 0 & -p_z \\ 0 & 1 & 0 & 0 \\ 0 & 0 & 1 & 0 \\ -p_z & 0 & 0 & p_0 \end{pmatrix}. \tag{A.14}$$

Note that Eq. (A.14), and Lorentz transformations in general, are invertible, such that

$$\Lambda_{\text{lab}\to\text{rest}}^{-1} = \Lambda_{\text{rest}\to\text{lab}} \tag{A.15}$$

holds for any Lorentz transformation Λ.

A.3 Calculation of Lorentz-invariant phase space

Here, more details on how to obtain Eq. (A.35) and Eq. (A.36) are given. Starting with Eq. (A.32) it is clear that it is necessary to compute the 2-body LIPS three times for the cascade-like decay $B^-(P) \to \gamma^*(q)[\to \ell'^+(q_1)\ell'^-(q_2)]\, W(k)[\to \ell^-(k_2)\bar{\nu}(k_1)]$. It is convenient to start with the definition of the 2-body LIPS:

$$\mathrm{d}\Phi_2(P;q,k) = \frac{\mathrm{d}^4 q}{(2\pi)^4}\frac{\mathrm{d}^4 k}{(2\pi)^4}\delta^4(P-q-k)\Theta(q^0)\Theta(k^0)\,, \tag{A.16}$$

where the RHS shows the normalized differentials for both final state momenta. Two Θ functions ensure positive energies of the final-states, and an overall delta distribution ensure energy conservation. Integrated over the zeroth component of both momenta this expression is equivalent to

$$\mathrm{d}\Phi_2(P;q,k) = \frac{1}{(2\pi)^6}\frac{\mathrm{d}^3 q}{2E_q}\frac{\mathrm{d}^3 k}{2E_k}\delta(E-E_q-E_k)\delta^3(\vec{p}-\vec{q}-\vec{k})\,. \tag{A.17}$$

Using the kinematic properties of a B meson at rest

$$\vec{p} = 0\,, \qquad E = \sqrt{p^2 - |\vec{p}|^2} = \sqrt{p^2} = m \tag{A.18}$$

and intrinsic symmetry of the delta distribution the expression becomes

$$\mathrm{d}\Phi_2(P;q,k) = \frac{1}{(2\pi)^6}\frac{\mathrm{d}^3 q}{2\sqrt{q^2+|\vec{q}|^2}}\frac{\mathrm{d}^3 k}{2\sqrt{k^2+|\vec{k}|^2}} \times \delta\left(M_B - \sqrt{q^2+|\vec{q}|^2} - \sqrt{k^2+|\vec{k}|^2}\right)\delta^3\left(\vec{q}+\vec{k}\right)\,. \tag{A.19}$$

Exploiting the last delta distribution in Eq. (A.19) while integrating over $\mathrm{d}^3 q$ the two-body phase space can be expressed as

$$\mathrm{d}\Phi_2(P;q,k) = \frac{1}{(2\pi)^6}\frac{4\pi}{2\sqrt{q^2+|\vec{k}|^2}}\frac{\mathrm{d}|k||\vec{k}|^2}{2\sqrt{k^2+|\vec{k}|^2}}\delta\left(M_B - \sqrt{q^2+|\vec{k}|^2} - \sqrt{k^2+|\vec{k}|^2}\right)\,. \tag{A.20}$$

In Eq. (A.20) the delta distribution yields no contribution to integration unless the argument is equal to zero. Defining the argument of the delta distribution in Eq. (A.20) as $f(|\vec{k}|)$ its zeroes are

determined by:

$$\begin{aligned} f(|\vec{k}|) &= M_B - \sqrt{q^2 + |\vec{k}|^2} - \sqrt{k^2 + |\vec{k}|^2} \stackrel{!}{=} 0 \\ &\Leftrightarrow M_B^2 - 2M_B\sqrt{q^2 + |\vec{k}|^2} + q^2 + |\vec{k}|^2 = k^2 + |\vec{k}|^2 \\ &\Leftrightarrow -2M_B\sqrt{q^2 + |\vec{k}|^2} = k^2 - q^2 - M_B^2 \\ &\Rightarrow |\vec{k}|^2 = \frac{(k^2 - q^2 - M_B^2)^2 - 4M_B^2 q^2}{4M_B^2} \\ &\Rightarrow |\vec{k}| = \pm\frac{\lambda^{1/2}(k^2, q^2, M_B^2)}{2M_B}\,, \end{aligned} \tag{A.21}$$

where the Källén triangle function $\lambda(k^2, q^2, M_B^2) = (k^2 - q^2 - M_B^2)^2 - 4M_B^2 q^2$ naturally arises. Furthermore, we use for a generic function $g(x)$:

$$\delta(g(x)) = \sum_i \frac{\delta(x - a_i)}{|g'(a_i)|}\,, \tag{A.22}$$

which is a property of the delta distribution, where a_i are the zeroes of the function $g(x)$. The derivative of Eq. (A.21) reads

$$\begin{aligned} f'(|\vec{k}|) &= -\frac{1}{2}(q^2 + |\vec{k}|^2)^{-1/2} 2|\vec{k}| - \frac{1}{2}(k^2 + |\vec{k}|^2)^{-1/2} 2|\vec{k}| \\ &= -|\vec{k}|((q^2 + |\vec{k}|^2)^{-1/2} + (k^2 + |\vec{k}|^2)^{-1/2})\,. \end{aligned} \tag{A.23}$$

Having everything at hand, the delta distribution in Eq. (A.20) can be reformulated as

$$\begin{aligned} \mathrm{d}\Phi_2(P; q, k) &= \frac{1}{(2\pi)^6} \frac{4\pi}{2\sqrt{q^2 + |\vec{k}|^2}} \frac{\mathrm{d}|k||\vec{k}|^2}{2\sqrt{k^2 + |\vec{k}|^2}} \\ &\times \left(\frac{1}{|f'(|\vec{k}|)|} \delta\left(|\vec{k}| + \frac{\lambda^{1/2}(k^2, q^2, M_B^2)}{2M_B} \right) + \frac{1}{|f'(|\vec{k}|)|} \delta\left(|\vec{k}| - \frac{\lambda^{1/2}(k^2, q^2, M_B^2)}{2M_B} \right) \right), \end{aligned} \tag{A.24}$$

where Eq. (A.22) was used. Since the Källén function is strictly positive throughout the physical phase space of its arguments the first term does not contribute

$$\mathrm{d}\Phi_2(P; q, k) = \frac{1}{(2\pi)^6} \frac{4\pi}{2\sqrt{q^2 + |\vec{k}|^2}} \frac{\mathrm{d}|k||\vec{k}|^2}{2\sqrt{k^2 + |\vec{k}|^2}} \frac{1}{|f'(|\vec{k}|)|} \delta\left(|\vec{k}| - \frac{\lambda^{1/2}(k^2, q^2, M_B^2)}{2M_B} \right). \tag{A.25}$$

Using Eq. (A.23) the differential phase space volume reads

$$\begin{aligned} \mathrm{d}\Phi_2(P;q,k) = &\frac{1}{(2\pi)^6}\frac{4\pi}{2\sqrt{q^2+|\vec{k}|^2}} \\ &\times \frac{\mathrm{d}|k||\vec{k}|}{2\sqrt{k^2+|\vec{k}|^2}}\frac{1}{(q^2+|\vec{k}|^2)^{-1/2}+(k^2+|\vec{k}|^2)^{-1/2}}\delta\left(|\vec{k}|-\frac{\lambda^{1/2}(k^2,q^2,M_B^2)}{2M_B}\right). \end{aligned} \tag{A.26}$$

Performing the last integration over $|\vec{k}|$ while using the remaining delta distribution results in

$$\begin{aligned} \mathrm{d}\Phi_2(P;q,k) = &\frac{1}{(2\pi)^6}\frac{4\pi}{4\sqrt{q^2+\frac{\lambda(k^2,q^2,M_B^2)}{4M_B^2}}} \\ &\times \frac{\lambda^{1/2}(k^2,q^2,M_B^2)}{2M_B\sqrt{k^2+\frac{\lambda(k^2,q^2,M_B^2)}{4M_B^2}}}\frac{1}{\left(q^2+\frac{\lambda(k^2,q^2,M_B^2)}{4M_B^2}\right)^{-1/2}+\left(k^2+\frac{\lambda(k^2,q^2,M_B^2)}{4M_B^2}\right)^{-1/2}}. \end{aligned} \tag{A.27}$$

With further simplifications the final results becomes

$$\begin{aligned} \mathrm{d}\Phi_2(P;q,k) &= \frac{1}{4M_B(2\pi)^5}\frac{\lambda^{1/2}(k^2,q^2,M_B^2)}{\left(q^2+\frac{\lambda(M_B^2,q^2,k^2)}{4M_B^2}\right)^{1/2}+\left(k^2+\frac{\lambda(M_B^2,k^2,q^2)}{4M_B^2}\right)^{1/2}} \\ &= \frac{1}{4M_B(2\pi)^5}\frac{\lambda^{1/2}(k^2,q^2,M_B^2)}{\left(q^2+\frac{(M_B^2+q^2-k^2)^2-4M_B^2q^2}{4M_B^2}\right)^{1/2}+\left(k^2+\frac{(M_B^2+k^2-q^2)^2-4M_B^2k^2}{4M_B^2}\right)^{1/2}} \\ &= \frac{\lambda^{1/2}(k^2,q^2,M_B^2)}{4M_B(2\pi)^5}\frac{1}{\left(\frac{(M_B^2+q^2-k^2)}{2M_B}\right)+\left(\frac{(M_B^2+k^2-q^2)}{2M_B}\right)} \\ &= \frac{\lambda^{1/2}(k^2,q^2,M_B^2)}{4M_B^2(2\pi)^5}. \end{aligned} \tag{A.28}$$

Similarly, $\mathrm{d}\Phi_2(k;k_1,k_2)$ and $\mathrm{d}\Phi_2(q;q_1,q_2)$ can be calculated in their respective rest frames:

$$\mathrm{d}\Phi_2(k;k_1,k_2) = \frac{\lambda^{1/2}(k_1^2,k_2^2,k^2)}{8k^2(2\pi)^6}\mathrm{d}\phi\,\mathrm{d}\cos\theta_V\,, \tag{A.29}$$

and

$$\mathrm{d}\Phi_2(q;q_1,q_2) = \frac{\lambda^{1/2}(q_1^2,q_2^2,q^2)}{8q^2(2\pi)^5}\mathrm{d}\cos\theta_W\,. \tag{A.30}$$

Note that the different denominators occur due to the different rest frames. For example, compare Eq. (A.3) and Eq. (A.4) with Eq. (A.18).

A.4 Decay width

The partial decay width of an initial particle in its rest frame into n final-state particles is given by, cf. Ref. [61],

$$\mathrm{d}\Gamma = \frac{(2\pi)^4}{2M}|\mathcal{M}|^2\mathrm{d}\Phi_n(P;p_1,...,p_n)\,, \tag{A.31}$$

where M is the rest mass, $\mathcal{M}$ is the invariant matrix element, and P is the four momentum of the decaying particle. Furthermore $p_1,...,p_n$ are the four momenta of the n final-state particles and $\mathrm{d}\Phi_n(P;p_1,...,p_n)$ is the n-body phase space. The n-body phase space can be reduced to a multiplication of 2-body phase space volumes by recursively applying

$$\mathrm{d}\Phi_n(P;p_1,...,p_n) = \mathrm{d}\Phi_j(p;p_1,...,p_j)\times\mathrm{d}\Phi_{n-j+1}(P;p,p_{j+1},...,p_n)(2\pi)^3\mathrm{d}p^2, \tag{A.32}$$

where $p = p_1,...,p_j$ is the four momentum of an intermediate particle which further decays into j particles. For the particular case of interest the 4-particle phase space takes the form

$$\begin{aligned}\mathrm{d}\Phi_4(P;q_1,q_2,k_1,k_2) &= \mathrm{d}\Phi_2(q;q_1,q_2)\mathrm{d}\Phi_3(P;q,k_1,k_2)(2\pi)^3\mathrm{d}q^2\\ &= \mathrm{d}\Phi_2(q;q_1,q_2)\mathrm{d}\Phi_2(k;k_1,k_2)\mathrm{d}\Phi_2(P;k,q)(2\pi)^6\mathrm{d}q^2\mathrm{d}k^2\,,\end{aligned} \tag{A.33}$$

with the 3-particle phase space given as

$$\mathrm{d}\Phi_3(P;q,k_1,k_2) = \mathrm{d}\Phi_2(k;k_1,k_2)\mathrm{d}\Phi_2(P;k,q)(2\pi)^3\mathrm{d}k^2\,. \tag{A.34}$$

Using the results from App. A and App. A.3 the invariant phase space for $B^-(P)\to\gamma^*(q)[\to \ell'^+(q_1)\ell'^-(q_2)]\,W(k)[\to\ell^-(k_2)\bar{\nu}(k_1)]$ results in

$$\begin{aligned}&\mathrm{d}\Phi_4(P;q_1,q_2,k_1,k_2)\\ &= \frac{\lambda^{1/2}(q^2,q_1^2,q_2^2)\lambda^{1/2}(k^2,k_1^2,k_2^2)\lambda^{1/2}(M_B^2,q^2,k^2)}{2^8(2\pi)^{10}q^2\,k^2\,M_B^2}\mathrm{d}\cos\theta_W\mathrm{d}\phi\mathrm{d}\cos\theta_\gamma\mathrm{d}q^2\mathrm{d}k^2\,.\end{aligned} \tag{A.35}$$

The invariant phase space for $B^-(P)\to\gamma(q)W^*(k)[\to\ell^-(k_2)\bar{\nu}(k_1)]$ is

$$\mathrm{d}\Phi_3(P;k,q_1,q_2) = \frac{\lambda^{1/2}(M_B^2,k^2,q^2)\lambda^{1/2}(q^2,q_1^2,q_2^2)}{32(2\pi)^7M_B^2q^2}\mathrm{d}\cos\theta_W\mathrm{d}q^2\,. \tag{A.36}$$

Using Eq. (A.36) and Eq. (A.35) the differential decay width can be expressed as

$$\begin{aligned}
&\mathrm{d}\Gamma\left(B^-(P) \to \gamma^*(q)[\to \ell'^+(q_1)\ell'^-(q_2)]\, W(k)[\to \ell^-(k_2)\bar{\nu}(k_1)]\right) \\
&= |\mathcal{M}|^2 \frac{\lambda^{1/2}(q^2, q_1^2, q_2^2)\lambda^{1/2}(k^2, k_1^2, k_2^2)\lambda^{1/2}(M_B^2, q^2, k^2)}{2^9(2\pi)^6 M_B^3 q^2 k^2} \mathrm{d}\cos\theta_W \mathrm{d}\phi \mathrm{d}\cos\theta_\gamma \mathrm{d}q^2 \mathrm{d}k^2 \\
&= |\mathcal{M}|^2 \frac{\lambda^{1/2}(M_B^2, q^2, k^2)}{2^9(2\pi)^6 M_B^3} \sqrt{\left(1 - \frac{4m_{\ell'}^2}{k^2}\right)} \left(1 - \frac{4m_\ell^2}{q^2}\right) \mathrm{d}\cos\theta_W \mathrm{d}\phi \mathrm{d}\cos\theta_\gamma \mathrm{d}q^2 \mathrm{d}k^2 .
\end{aligned} \tag{A.37}$$

APPENDIX B

Details on the computation of the amplitude $B^- \to \ell^- \bar{\nu}_\ell \ell'^- \ell'^+$

Here we show how to generally compute the BSM amplitude given from the operator basis given in Eq. (3.2) and we show results for the specific case of the SM. Since the effective Hamiltonian decomposes into a sum of products of Wilson coefficients and operators we start by denoting the amplitude with a subscript X selecting the Wilson coefficient of choice:

$$\begin{aligned}
&\mathcal{A}_X\left(B_q^- \to \ell' \bar{\ell}' \ell \bar{\nu}_\ell\right) \\
&= \langle \ell'(q_1) \bar{\ell}'(q_2) \ell(p_\ell) \bar{\nu}_\ell(p_{\bar{\nu}_\ell}) | \, \mathcal{H}^{\text{eff}} \, | B_q^-(p) \rangle \\
&= \frac{4\tilde{G}_F}{\sqrt{2}} \tilde{V}_{qb} C_X \, \langle \ell' \bar{\ell}' \ell \bar{\nu}_\ell | \, \bar{q} \Gamma_h^{\tilde{\nu}} b \bar{\ell} \Gamma_{l\tilde{\nu}} \nu_\ell \, | B_q^- \rangle \\
&= \frac{4\tilde{G}_F}{\sqrt{2}} \tilde{V}_{qb} C_X \left(\langle \ell' \bar{\ell}' | \, \bar{q} \Gamma_h^{\tilde{\nu}} b \, | B_q^- \rangle \, \langle \ell \bar{\nu}_\ell | \, \bar{\ell} \Gamma_{l\tilde{\nu}} \nu_\ell \, | 0 \rangle + \langle \ell' \bar{\ell}' \ell \bar{\nu}_\ell | \, \bar{\ell} \Gamma_{l\tilde{\nu}} \nu_\ell \, | 0 \rangle \, \langle 0 | \, \bar{q} \Gamma_h^{\tilde{\nu}} b \, | B_q^- \rangle \right) ,
\end{aligned} \tag{B.1}$$

here the subscript q in B_q^- indicates the light quark flavor content of the negatively charged B meson, which is either up or strange. The $\tilde{G}_F$ and $\tilde{V}_{qb}$ are generalized redefinitions of the SM Fermi's constant and CKM matrix elements. The subscript $\tilde{\nu}$ is a multi-index to allow for either zero, one or two contractions in that position. The last line in Eq. (B.1) is obtained by taking into account all possible configurations of how the decay $B^- \to \ell^- \bar{\nu}_\ell \ell'^- \ell'^+$ can happen. Adhering to the same ordering one ends up with three possibilities shown in Fig. B.1.

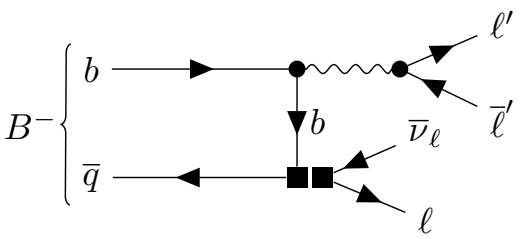

(a) The b quark first radiates off a photon then changes flavor via a charged weak interaction.

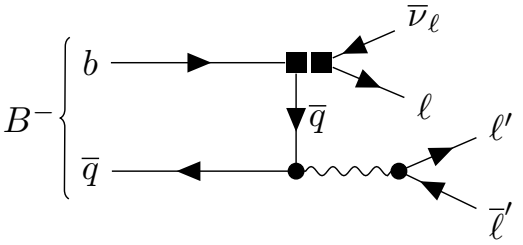

(b) The b quark first changes flavor via a charged weak interaction then the q-quark radiates off a photon.

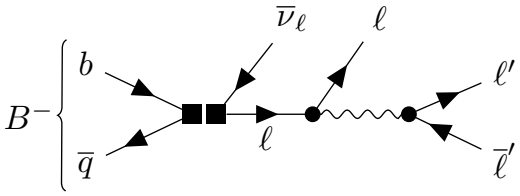

(c) The left part of the graph depicts the B-to-vacuum matrix element. The right part depicts the vacuum to 4 lepton matrix element. This graph corresponds to the final-state radiation (FSR) term.

Figure B.1: Diagrams depicting the quark content of the B meson in the decay $B^- \to \ell^- \bar{\nu}_\ell \ell'^- \ell'^+$. The 2 dots with an interpolating wavy line depict the electromagnetic interactions with a propagating virtual photon. The 2 boxes close to each other depict the electroweak current with an integrated-out W boson.

After the matrix elements in the last line of Eq. (B.1) are computed the amplitude reads

$$
\begin{aligned}
&\mathcal{A}_X\left(B_q^- \to \ell' \bar{\ell}' \ell \bar{\nu}_\ell\right) \\
&= \frac{4\tilde{G}_F}{\sqrt{2}} \tilde{V}_{qb} C_X \Bigg(\frac{ie^2 Q_{\ell'}}{q^2} \bar{u}^s(q_1) \gamma_\mu v^{s'}(q_2) T^{\mu\tilde{\nu}} \bar{u}^{s''}(p_\ell) \Gamma_{l\tilde{\nu}} v^{s'''}(p_{\bar{\nu}_\ell}) \\
&- \frac{e^2 Q_{\ell'} Q_\ell}{q^2} \bar{u}^s(q_1) \gamma_\mu v^{s'}(q_2) \bar{u}^{s''}(p_\ell) \gamma^\mu \frac{\not{q} + \not{p}_\ell + m_\ell}{(q+p_\ell)^2 - m_\ell^2} \Gamma_{l\tilde{\nu}} v^{s'''}(p_{\bar{\nu}_\ell}) \langle 0 | \, \bar{q} \Gamma_h^{\tilde{\nu}} b \, | B_q^- \rangle \Bigg) \\
&= \frac{4\tilde{G}_F}{\sqrt{2}} \frac{e^2 Q_{\ell'}}{q^2} \bar{u}^s(q_1) \gamma_\mu v^{s'}(q_2) \tilde{V}_{qb} C_X \Bigg(\mathrm{i} T^{\mu\tilde{\nu}} \bar{u}^{s''}(p_\ell) \Gamma_{l\tilde{\nu}} v^{s'''}(p_{\bar{\nu}_\ell}) \\
&- Q_\ell \bar{u}^{s''}(p_\ell) \gamma^\mu \frac{\not{q} + \not{p}_\ell + m_\ell}{(q+p_\ell)^2 - m_\ell^2} \Gamma_{l\tilde{\nu}} v^{s'''}(p_{\bar{\nu}_\ell}) \langle 0 | \, \bar{q} \Gamma_h^{\tilde{\nu}} b \, | B_q^- \rangle \Bigg),
\end{aligned}
\tag{B.2}
$$

where the different primed spinor-indices are contracted when computing the squared amplitude. For the evaluation of the individual matrix elements in the last line of Eq. (B.1) Wick contractions are helpful. In fact, the field operators within the matrix elements of Eq. (B.1) are implied to be

time-ordered. When necessary, this is emphasized by the time-ordering operator $\mathcal{T}$, for example, in Eq. (B.3). In time-ordered products of fields, Wick contractions help to evaluate Wick's theorem and give either the respective spinor when a field is contracted with its corresponding initial- or final-state or gives rise to a particle propagator as combinatorial factor when contracted with another particle field at another spacetime point.

We refer the reader to a standard quantum field theory text book for more details on Wick's theorem, e.g. [17, 18]. Next, it is shown how to compute each matrix element in Eq. (B.1).

Vacuum to lepton-neutrino Here, both fields are contracted with their respective final-states

$$\begin{aligned}\langle \ell(p_\ell)\bar{\nu}_\ell(p_{\bar{\nu}_\ell})|\,\bar{\ell}\Gamma_{l\tilde{\nu}}\bar{\nu}_\ell\,|0\rangle &= \langle \overbrace{\ell\bar{\nu}_\ell}|\overbrace{\bar{\ell}\Gamma_{l\tilde{\nu}}\nu_\ell}(0)\,|0\rangle \\ &= \bar{u}^{s''}(p_\ell)\Gamma_{l\tilde{\nu}}v^{s'''}(p_{\bar{\nu}_\ell})\,,\end{aligned} \tag{B.3}$$

where $\bar{u}^{s''}$ and $v^{s'''}$ are the resulting spinors. The index convention matches the one of Eq. (B.2).

Vacuum to 4 leptons In this case, four leptons are produced from the vacuum. As shown in Fig. B.1(c), two electromagnetic interactions are inserted in the matrix element. The electromagnetic interactions are inserted in the form of a factor of $(-ieQ_\ell\bar{\ell}A^\mu\ell(x))$ integrated over all space-time positions x and give rise to a photon propagator:

$$\begin{aligned}&\langle \ell'(q_1)\bar{\ell}'(q_2)\ell(p_\ell)\bar{\nu}_\ell(p_{\bar{\nu}_\ell})|\,\bar{\ell}\Gamma_{l\tilde{\nu}}\nu_\ell\,|0\rangle = \\ &= \int d^4x \int d^4y\,\langle \ell'\bar{\ell}'\ell\bar{\nu}_\ell|\,\mathcal{T}\left\{(-ieQ_{\ell'}\bar{\ell}'\overbrace{\not{A}\ell'(y))(-ieQ_\ell\bar{\ell}\not{A}\ell(x))}\,(\bar{\ell}\Gamma_{l\tilde{\nu}}\bar{\nu}_\ell(0))\right\}|0\rangle\,,\end{aligned} \tag{B.4}$$

where $\mathcal{T}$ stands for the time ordered product.

$$\begin{aligned}&\langle \ell'(q_1)\bar{\ell}'(q_2)\ell(p_\ell)\bar{\nu}_\ell(p_{\bar{\nu}_\ell})|\,\bar{\ell}\Gamma_{l\tilde{\nu}}\nu_\ell\,|0\rangle = \\ &= -e^2Q_{\ell'}Q_\ell\int \mathrm{d}^4x\int \mathrm{d}^4y\int\frac{\mathrm{d}r_1^4}{(2\pi)^4}\int\frac{\mathrm{d}r_2^4}{(2\pi)^4}e^{\mathrm{i}r_2(0-x)}e^{\mathrm{i}r_1(x-y)} \\ &\times\langle \ell'\bar{\ell}'\ell\bar{\nu}_\ell|\,\bar{\ell}'\gamma_\mu\ell'(y)\bar{\ell}\gamma_\nu\frac{\mathrm{i}(\not{r}_2+m_\ell)}{r_2^2-m_\ell^2+\mathrm{i}\epsilon}\Gamma_{l\tilde{\nu}}\nu_\ell(0)\,|0\rangle\,\frac{-\mathrm{i}g^{\mu\nu}}{r_1^2+\mathrm{i}\epsilon}\,.\end{aligned} \tag{B.5}$$

Take note here that along with the contraction of both photon fields as well as leptonic fields not only a propagator but also an exponential factor with integration over the inserted propagator

momentum arises, which ultimately ensures 4-momentum conservation. Furthermore, we find

$$\begin{aligned}
&\langle \ell'(q_1)\bar{\ell}'(q_2)\ell(p_\ell)\bar{\nu}_\ell(p_{\bar{\nu}_\ell})|\,\bar{\ell}\Gamma_{l\tilde{\nu}}\nu_\ell\,|0\rangle = \\
&= -e^2 Q_{\ell'} Q_\ell \int \mathrm{d}^4x \int \mathrm{d}^4y \int \frac{\mathrm{d}r_1^4}{(2\pi)^4} \int \frac{\mathrm{d}r_2^4}{(2\pi)^4} e^{\mathrm{i}(r_1-r_2)x} e^{-\mathrm{i}r_1 y} \\
&\langle \ell'\bar{\ell}'\ell\bar{\nu}_\ell|\bar{\ell}'\gamma_\mu\ell'(y)\bar{\ell}\gamma^\mu \frac{\not{r}_2 + m_\ell}{r_2^2 - m_\ell^2 + \mathrm{i}\epsilon}\Gamma_{l\tilde{\nu}}\nu_\ell(0)\,|0\rangle \frac{1}{r_1^2+\mathrm{i}\epsilon} \\
&= -e^2 Q_{\ell'} Q_\ell \int \mathrm{d}^4r_1 \int \mathrm{d}^4r_2 \int \frac{\mathrm{d}x^4}{(2\pi)^4} \int \frac{\mathrm{d}y^4}{(2\pi)^4} e^{\mathrm{i}(r_1-r_2+p_\ell)x} e^{\mathrm{i}(-r_1+q_1+q_2)y} \\
&\bar{u}^s(q_1)\gamma_\mu v^{s'}(q_2)\bar{u}^{s''}(p_\ell)\gamma^\mu \frac{\not{r}_2 + m_\ell}{r_2^2 - m_\ell^2 + \mathrm{i}\epsilon}\Gamma_{l\tilde{\nu}} v^{s'''}(p_{\bar{\nu}_\ell}) \frac{1}{r_1^2+\mathrm{i}\epsilon}\,. \qquad \text{(B.6)}
\end{aligned}$$

The integration over spacetime positions in combination with the exponential factor gives rise to the 4-momentum conserving delta function. Overall, the result reads

$$\begin{aligned}
&\langle \ell'(q_1)\bar{\ell}'(q_2)\ell(p_\ell)\bar{\nu}_\ell(p_{\bar{\nu}_\ell})|\,\bar{\ell}\Gamma_{l\tilde{\nu}}\nu_\ell\,|0\rangle = \\
&= -e^2 Q_{\ell'} Q_\ell \int \mathrm{d}^4r_1 \int \mathrm{d}^4r_2 \\
&\delta(r_2 - r_1 - p_\ell)\delta(r_1 - q)\bar{u}^s(q_1)\gamma_\mu v^{s'}(q_2)\bar{u}^{s''}(p_\ell)\gamma^\mu \frac{\not{r}_2 + m_\ell}{r_2^2 - m_\ell^2 + \mathrm{i}\epsilon}\Gamma_{l\tilde{\nu}} v^{s'''}(p_{\bar{\nu}_\ell}) \frac{1}{r_1^2+\mathrm{i}\epsilon} \\
&= -\frac{e^2 Q_{\ell'} Q_\ell}{q^2} \int \mathrm{d}^4r_2 \delta(r_2 - q - p_\ell)\bar{u}^s(q_1)\gamma_\mu v^{s'}(q_2)\bar{u}^{s''}(p_\ell)\gamma^\mu \frac{\not{r}_2 + m_\ell}{r_2^2 - m_\ell^2 + \mathrm{i}\epsilon}\Gamma_{l\tilde{\nu}} v^{s'''}(p_{\bar{\nu}_\ell}) \\
&= -\frac{e^2 Q_{\ell'} Q_\ell}{q^2}\bar{u}^s(q_1)\gamma_\mu v^{s'}(q_2)\bar{u}^{s''}(p_\ell)\gamma^\mu \frac{\not{q} + \not{p}_\ell + m_\ell}{(q+p_\ell)^2 - m_\ell^2}\Gamma_{l\tilde{\nu}} v^{s'''}(p_{\bar{\nu}_\ell})\,. \qquad \text{(B.7)}
\end{aligned}$$

***B* meson to 2 leptons** Here, we discuss the transition matrix element of a B meson into two charged leptons. As above we start by inserting two electromagnetic interactions. We start by denoting the time-ordered product

$$\begin{aligned}
&\langle \ell'(q_1)\bar{\ell}'(q_2)|\,\bar{q}\Gamma_h^{\tilde{\nu}} b\,|B_q^-\rangle = \\
&= \int \mathrm{d}^4x \int \mathrm{d}^4y\, \langle \ell'\bar{\ell}'|\,\mathcal{T}\left\{(-\mathrm{i}eQ_{\ell'}\bar{\ell}'\overbrace{\not{A}\ell'(y))(-\mathrm{i}eQ_q\bar{q}\not{A}}q(x))\left(\bar{q}\Gamma_h^{\tilde{\nu}} b(0)\right)\right\}|B_q^-\rangle\,, \qquad \text{(B.8)}
\end{aligned}$$

where the photon propagator is obtained by contracting both photon fields A:

$$
\begin{aligned}
&\langle \ell'(q_1)\bar{\ell}'(q_2)|\, \bar{q}\Gamma_h^{\tilde{\nu}} b\, |B_q^-\rangle = \\
&= -e^2 Q_{\ell'} \int \mathrm{d}^4x \int \mathrm{d}^4y \int \frac{\mathrm{d}^4 r_1}{(2\pi)^4} e^{\mathrm{i}r_1(x-y)} \\
&\langle \ell'\bar{\ell}'|\, \mathcal{T}\left\{\bar{\ell}'\gamma_\mu \ell'(y) Q_q \bar{q}\gamma_\nu q(x)\bar{q}\Gamma_h^{\tilde{\nu}} b(0)\right\} |B_q^-\rangle \, \frac{-\mathrm{i}g^{\mu\nu}}{r_1^2 + \mathrm{i}\epsilon} \\
&= \mathrm{i}e^2 Q_{\ell'} \int \mathrm{d}^4x \int \mathrm{d}^4y \int \frac{\mathrm{d}^4 r_1}{(2\pi)^4} e^{\mathrm{i}r_1(x-y)} \\
&\overbrace{\langle \ell'\bar{\ell}'|\bar{\ell}'\gamma_\mu \ell'(y)}\, |0\rangle \, \langle 0|\, \mathcal{T}\left\{Q_q \bar{q}\gamma^\mu q(x)\bar{q}\Gamma_h^{\tilde{\nu}} b(0)\right\} |B_q^-\rangle \, \frac{1}{r_1^2 + \mathrm{i}\epsilon} \\
&= \mathrm{i}e^2 Q_{\ell'} \bar{u}^s(q_1)\gamma_\mu v^{s'}(q_2) \int \mathrm{d}^4x \int \frac{\mathrm{d}^4 y}{(2\pi)^4} \int \mathrm{d}^4 r_1 e^{ir_1 x} e^{iy(q_1+q_2-r_1)} \\
&\langle 0|\, \mathcal{T}\left\{Q_q \bar{q}\gamma^\mu q(x)\bar{q}\Gamma_h^{\tilde{\nu}} b(0)\right\} |B_q^-\rangle \, \frac{1}{r_1^2 + \mathrm{i}\epsilon} \\
&= \mathrm{i}e^2 Q_{\ell'} \bar{u}^s(q_1)\gamma_\mu v^{s'}(q_2) \int \mathrm{d}^4x \int \mathrm{d}^4 r_1 e^{\mathrm{i}r_1 x} \delta(r_1 - q) \\
&\langle 0|\, \mathcal{T}\left\{Q_q \bar{q}\gamma^\mu q(x)\bar{q}\Gamma_h^{\tilde{\nu}} b(0)\right\} |B_q^-\rangle \, \frac{1}{r_1^2 + \mathrm{i}\epsilon} \\
&= \frac{\mathrm{i}e^2 Q_{\ell'}}{q^2} \bar{u}^s(q_1)\gamma_\mu v^{s'}(q_2) \int \mathrm{d}^4x e^{\mathrm{i}qx} \, \langle 0|\, \mathcal{T}\left\{Q_q \bar{q}\gamma^\mu q(x)\bar{q}\Gamma_h^{\tilde{\nu}} b(0)\right\} |B_q^-\rangle \\
&= \frac{\mathrm{i}e^2 Q_{\ell'}}{q^2} \bar{u}^s(q_1)\gamma_\mu v^{s'}(q_2) T^{\mu\tilde{\nu}}\,,
\end{aligned}
\tag{B.9}
$$

where $T^{\mu\tilde{\nu}} = \int \mathrm{d}^4x e^{\mathrm{i}qx} \, \langle 0|\, \mathcal{T}\left\{Q_q \bar{q}\gamma^\mu q(x)\bar{q}\Gamma_h^{\tilde{\nu}} b(0)\right\} |B_q^-\rangle$ is a non-perturbative object called the hadronic tensor.

***B* meson to vacuum** The local matrix element $\langle 0|\, \bar{q}\Gamma_h^{\tilde{\nu}} b\, |B_q^-\rangle$ is related to the B-meson decay constant often defined as

$$
\langle 0|\, \bar{q}\gamma^\nu\gamma_5 b\, |B_q^-\rangle = \mathrm{i}f_B p^\nu\,. \tag{B.10}
$$

In the vector current case of the operator basis Eq. (3.2) one can relate this matrix element in a rather straightforward way as

$$
\begin{aligned}
\langle 0|\, \bar{q}\gamma^\nu \frac{(\mathbb{1} \mp \gamma_5)}{2} b\, |B_q^-\rangle &= \frac{1}{2}\left(\langle 0|\, \bar{q}\gamma^\nu b\, |B_q^-\rangle \mp \langle 0|\, \bar{q}\gamma^\nu\gamma_5 b\, |B_q^-\rangle\right) \\
&= \mp\mathrm{i}\frac{f_B}{2} p^\nu\,,
\end{aligned}
\tag{B.11}
$$

where the first term in the first line vanishes by parity. The vector and pseudoscalar current are related via an additional derivative

$$\begin{aligned}\partial_\nu \langle 0|\, \bar{q}\gamma^\nu \frac{(\mathbb{1} \mp \gamma_5)}{2} b\, |B_q^-\rangle &= \mathrm{i}(m_q + m_b) \langle 0|\, \bar{q} \frac{(\mathbb{1} \mp \gamma_5)}{2} b\, |B_q^-\rangle \\ &= \mathrm{i} p_\nu \langle 0|\, \bar{q}\gamma^\nu \frac{(\mathbb{1} \mp \gamma_5)}{2} b\, |B_q^-\rangle = \pm \frac{f_B}{2} p^2 \,. \end{aligned} \tag{B.12}$$

With $p^2 = M_B^2$ the pseudoscalar-like matrix element reads

$$\langle 0|\, \bar{q} \frac{(\mathbb{1} \mp \gamma_5)}{2} b\, |B_q^-\rangle = \mp \mathrm{i} \frac{f_B}{2} \frac{M_B^2}{m_q + m_b} \,. \tag{B.13}$$

Furthermore, the tensor current case vanishes by Lorentz symmetry

$$\begin{aligned}&\langle 0|\, \bar{q}\sigma^{\nu\rho} \frac{(\mathbb{1} \mp \gamma_5)}{2} b\, |B_q^-\rangle = \frac{\mathrm{i}}{4} \langle 0|\, \bar{q} \left(\gamma^\nu\gamma^\rho - \gamma^\rho\gamma^\nu\right) (\mathbb{1} \mp \gamma_5)\, b\, |B_q^-\rangle \\ &= \frac{\mathrm{i}}{4} \langle 0|\, \bar{q} \left(\gamma^\nu\gamma^\rho - \gamma^\rho\gamma^\nu\right) b\, |B_q^-\rangle \mp \frac{\mathrm{i}}{4} \langle 0|\, \bar{q} \left(\gamma^\nu\gamma^\rho - \gamma^\rho\gamma^\nu\right) \gamma_5 b\, |B_q^-\rangle = 0 \,, \end{aligned} \tag{B.14}$$

since there can be no Lorentz structure constructed with only one independent momentum p_ν and $g_{\nu\rho}$ or $\epsilon_{\nu\rho\alpha\beta}$ which can recover the antisymmetry between $\nu \leftrightarrow \rho$ on the right hand side.

B.1 Functions $f_{i,j}$ and $g_{i,j}$

To shorten the rather lengthy expressions used in Eq. (3.73) and Eq. (3.78) we introduce the abbreviations

$$k_B^2 = m_B^2 - k^2\,, \quad k_\pm^2 = k^2 \pm m_\ell^2\,, \quad q_+^2 = q^2 + 2m_{\ell'}^2\,, \tag{B.15}$$

to substitute some of the reoccurring expressions for masses and momenta. We further define the short-hand notation

$$\Delta(k^2, q^2) = k_B^2 - q^2\,, \quad L_D = \frac{L_+(k^2, q^2) - L_-(k^2, q^2)}{\sqrt{\lambda(m_B^2, k^2, q^2)}}\,, \tag{B.16}$$

$$L_\pm(k^2, q^2) = \log\left(1 \pm \frac{k_-^2\sqrt{\lambda(m_B^2, k^2, q^2)}}{k_B^2 k_+^2 + k_-^2 q^2}\right), \tag{B.17}$$

for substitution in the functions $f_{i,j}$ of Eq. (3.73) and

$$\tilde{L}_D = \frac{1}{\sqrt{\lambda(m_B^2, k^2, q^2)}}\log\left(\frac{4k_-^2 k^2 q^2(k_B^2 + k_-^2) + 4m_\ell^2 k_B^4 k^2}{\left(k_+^2\Delta(k^2, q^2) + 2k^2 q^2\right)^2}\right), \tag{B.18}$$

for substitution in the functions $g_{i,j}$ in Eq. (3.78). The non-vanishing functions $f_{i,j}$ in Eq. (3.73) are:

$$f_{1,1} = \frac{64\pi k_-^2 q_+^2 (k_+^2 + k^2)[\lambda(m_B^2, k^2, q^2) + 6k^2 q^2]}{9k^2}\,, \tag{B.19}$$

$$f_{2,2} = \frac{32\pi k_-^2 q_+^2 q^2 (k_+^2 + k^2)[\lambda(m_B^2, k^2, q^2) + 12k^2 q^2]}{9k^4}\,, \tag{B.20}$$

$$f_{3,3} = m_\ell^2 \frac{32\pi k_-^2 q_+^2 q^2 \lambda(m_B^2, k^2, q^2)}{3k^4}\,, \tag{B.21}$$

$$f_{4,4} = \frac{64\pi k_-^2 q_+^2 (k_+^2 + k^2)\lambda(m_B^2, k^2, q^2)}{9k^2}\,, \tag{B.22}$$

$$f_{1,2} = -\frac{64\pi k_-^2 q_+^2 q^2 (k_+^2 + k^2)\Delta(k^2, q^2)}{3k^2}\,, \tag{B.23}$$

$$f_{1,5} = m_\ell^2 \frac{128\pi q_+^2}{3k_-^2} \left(k_-^2 \left(\Delta(k^2,q^2) - k_+^2 \right) - k_B^2 k^2 \left(\Delta(k^2,q^2) - 2m_\ell^2 \right) L_D(k^2,q^2) \right) , \tag{B.24}$$

$$f_{2,5} = -m_\ell^2 \frac{128\pi q_+^2 q^2}{3k_-^2} \left(3k_-^2 - \left(3k_B^2 k^2 + k_-^2 \right) L_D(k^2,q^2) \right) , \tag{B.25}$$

$$f_{3,5} = -m_\ell^2 \frac{64\pi q_+^2 q^2}{3k_B^2 k_-^2 k^2} \left(k_-^2 \left(k_-^2 \Delta(k^2,q^2) + 2k^2 \left(k_B^2 + 2k_-^2 \right) \right) - 2k_B^2 k^2 \left(k_B^2 k^2 + k_-^2 k_+^2 \right) L_D(k^2,q^2) \right) , \tag{B.26}$$

$$f_{4,5} = -m_\ell^2 \frac{128\pi q_+^2}{3k_-^2} \left(k_-^2 \Delta(k^2,q^2) - k^2 \left(k_B^2 \Delta(k^2,q^2) - 2k_-^2 q^2 \right) L_D(k^2,q^2) \right) , \tag{B.27}$$

$$\begin{aligned} f_{5,5} = & -m_\ell^2 \frac{128\pi q_+^2}{3k_B^4 k_-^2 \left(k_-^2 q^2 (k_B^2 + k_-^2) + m_\ell^2 k_B^4 \right)} \\ & \times \Bigg(k_-^2 \Big(k_-^2 (k_B^2 + k_-^2) \left(k_B^2 - \Delta(k^2,q^2) \right) \left(4k_-^4 + k_-^2 \left(3k_B^2 + \Delta(k^2,q^2) \right) + 4k_B^4 \right) \\ & + m_\ell^2 \Big(4k_-^6 \left(k_B^2 - \Delta(k^2,q^2) \right) + 8k_B^2 k_-^4 \left(2k_B^2 - \Delta(k^2,q^2) \right) + k_B^4 k_-^2 \left(13k_B^2 - 5\Delta(k^2,q^2) \right) \\ & + 2k_B^6 \left(2k_B^2 - \Delta(k^2,q^2) \right) \Big) + 8m_\ell^4 k_B^4 (k_B^2 + k_-^2) \Big) \\ & + 2k_B^2 k^2 \left(k_B^2 \left(\Delta(k^2,q^2) - 2k_B^2 \right) - 2k_-^2 (k_B^2 + k_-^2) - 4m_\ell^2 (k_B^2 + k_-^2) \right) \\ & \times \left(k_-^2 q^2 (k_B^2 + k_-^2) + m_\ell^2 k_B^4 \right) L_D(k^2,q^2) \Bigg) . \end{aligned} \tag{B.28}$$

The non-vanishing functions $g_{i,j}$ in Eq. (3.78) are:

$$g_{1,3} = m_\ell^2 \frac{32\pi k_-^2 q_+^2 q^2 \sqrt{\lambda(m_B^2, k^2, q^2)}}{3k^2}\,, \tag{B.29}$$

$$g_{1,4} = \frac{32\pi k_-^2 q_+^2 \Delta(k^2, q^2) \sqrt{\lambda(m_B^2, k^2, q^2)}}{3}\,, \tag{B.30}$$

$$g_{2,3} = -m_\ell^2 \frac{16\pi k_-^2 q_+^2 q^2 \Delta(k^2, q^2) \sqrt{\lambda(m_B^2, k^2, q^2)}}{3k^4}\,, \tag{B.31}$$

$$g_{2,4} = -\frac{64\pi k_-^2 q_+^2 q^2 \sqrt{\lambda(m_B^2, k^2, q^2)}}{3}\,, \tag{B.32}$$

$$g_{1,5} = m_\ell^2 \frac{32\pi q_+^2}{3k_B^2 k_-^2} \left(2k_-^4 \sqrt{\lambda(m_B^2, k^2, q^2)} - 4k_B^4 k^2 \left(\Delta(k^2, q^2) - 2m_\ell^2 \right) \tilde{L}_D(k^2, q^2) \right)\,, \tag{B.33}$$

$$g_{2,5} = m_\ell^2 \frac{32\pi q_+^2 q^2}{3k_B^2 k_-^2 k^2} \left(k_-^4 \sqrt{\lambda(m_B^2, k^2, q^2)} + 4k_B^2 k^2 \left(3k_B^2 k^2 + k_-^4 \right) \tilde{L}_D(k^2, q^2) \right)\,, \tag{B.34}$$

$$g_{3,5} = m_\ell^2 \frac{128\pi q_+^2 q^2}{3k_-^2} \left(k_B^2 k^2 + k_+^2 k_-^2 \right) \tilde{L}_D(k^2, q^2)\,, \tag{B.35}$$

$$g_{4,5} = m_\ell^2 \frac{128\pi k^2 q_+^2}{3k_-^2} \left(2k_-^2 \left(\Delta(k^2, q^2) - k_B^2 \right) + k_B^2 \Delta(k^2, q^2) \right) \tilde{L}_D(k^2, q^2)\,,$$

$$g_{5,5} = m_\ell^2 \frac{256\pi k^2 q_+^2}{3k_B^2 k_-^2 \left(k_-^2 q^2 (k_B^2 + k_-^2) + m_\ell^2 k_B^4 \right) \left(k_+^2 \Delta(k^2, q^2) + 2k^2 q^2 \right)}$$

$$\times \left(k_B^2 k_-^4 (k_B^2 + k_-^2)(q^2 + 2m_\ell^2) \sqrt{\lambda(m_B^2, k^2, q^2)} + \left(k_+^2 \Delta(k^2, q^2) + 2k^2 q^2 \right) \left(m_\ell^2 k_B^4 + k_-^2 q^2 (k_B^2 + k_-^2) \right) \right. \tag{B.36}$$

$$\left. \times \left(4m_\ell^2 (k_B^2 + k_-^2) + 2 \left(k_B^4 + k_-^4 + k_B^2 k_-^2 \right) - k_B^2 \Delta(k^2, q^2) \right) \tilde{L}_D(k^2, q^2) \right). \tag{B.37}$$

B.2 Projectors on form factors

Here, we give the projectors of a general Lorentz tensor on our form factor basis as defined in Eq. (3.47). The six form factors used in the main text are

$$
\begin{aligned}
\frac{1}{m_B}\mathcal{P}_1^{\mu\nu}(k,q) &= \frac{k\cdot q}{2\left((k\cdot q)^2-k^2q^2\right)}g^{\mu\nu} + \frac{3q^2k\cdot q}{2\left((k\cdot q)^2-k^2q^2\right)^2}k^\mu k^\nu \\
&\quad - \frac{(k\cdot q)^2+2k^2q^2}{2\left((k\cdot q)^2-k^2q^2\right)^2}k^\mu q^\nu - \frac{3(k\cdot q)^2}{2\left((k\cdot q)^2-k^2q^2\right)^2}q^\mu k^\nu \\
&\quad + \frac{3k^2k\cdot q}{2\left((k\cdot q)^2-k^2q^2\right)^2}q^\mu q^\nu\,, \\
\frac{1}{m_B}\mathcal{P}_2^{\mu\nu}(k,q) &= \frac{k^2}{2\left((k\cdot q)^2-k^2q^2\right)}g^{\mu\nu} + \frac{2(k\cdot q)^2+k^2q^2}{2\left((k\cdot q)^2-k^2q^2\right)^2}k^\mu k^\nu \\
&\quad - \frac{3k^2k\cdot q}{2\left((k\cdot q)^2-k^2q^2\right)^2}k^\mu q^\nu - \frac{3k^2k\cdot q}{2\left((k\cdot q)^2-k^2q^2\right)^2}q^\mu k^\nu \\
&\quad + \frac{3k^4}{2\left((k\cdot q)^2-k^2q^2\right)^2}q^\mu q^\nu\,, \\
\frac{1}{m_B}\mathcal{P}_3^{\mu\nu}(k,q) &= \frac{1}{(k\cdot q)^2-k^2q^2}k^\mu k^\nu - \frac{2k^2}{\left((k\cdot q)^2-k^2q^2\right)\left(2k\cdot q+q^2\right)}q^\mu k^\nu \\
&\quad - \frac{k^2}{\left((k\cdot q)^2-k^2q^2\right)\left(2k\cdot q+q^2\right)}q^\mu q^\nu\,, \\
\frac{1}{m_B}\mathcal{P}_4^{\mu\nu}(k,q) &= -\frac{\mathrm{i}}{\left((k\cdot q)^2-k^2q^2\right)}\epsilon^{\mu\nu\rho\sigma}k_\rho q_\sigma\,, \\
m_B\mathcal{P}_5^{\mu\nu}(k,q) &= -\frac{k\cdot q}{(k\cdot q)^2-k^2q^2}q^\mu k^\nu + \frac{k^2}{(k\cdot q)^2-k^2q^2}q^\mu q^\nu\,, \\
m_B\mathcal{P}_6^{\mu\nu}(k,q) &= \frac{q^2}{(k\cdot q)^2-k^2q^2}q^\mu k^\nu - \frac{k\cdot q}{(k\cdot q)^2-k^2q^2}q^\mu q^\nu\,.
\end{aligned}
\tag{B.38}
$$

Bibliography

[1] S. Weinberg, *A Model of Leptons*, Phys. Rev. Lett. **19** (1967) 1264 (cit. on p. 1).

[2] S. L. Glashow, *Partial Symmetries of Weak Interactions*, Nucl. Phys. **22** (1961) 579 (cit. on p. 1).

[3] A. Salam, "Weak and Electromagnetic Interactions", *Selected Papers of Abdus Salam*, World Scientific, 1968 367, ISBN: 9789810216627 (cit. on p. 1).

[4] P. W. Higgs, *Broken Symmetries and the Masses of Gauge Bosons*, Phys. Rev. Lett. **13** (1964) 508, ed. by J. C. Taylor (cit. on p. 1).

[5] F. Englert and R. Brout, *Broken Symmetry and the Mass of Gauge Vector Mesons*, Phys. Rev. Lett. **13** (1964) 321, ed. by J. C. Taylor (cit. on p. 1).

[6] A. Collaboration, *Observation of a new particle in the search for the Standard Model Higgs boson with the ATLAS detector at the LHC*, Phys. Lett. B **716** (2012) 1 (cit. on p. 1).

[7] CMS Collaboration, *Observation of a new boson at a mass of 125 GeV with the CMS experiment at the LHC*, Phys. Lett. B **716** (2012) 30 (cit. on p. 1).

[8] S. Kürten, M. Zanke, B. Kubis and D. van Dyk, *Dispersion relations for $B^- \to \ell^- \bar{\nu}_\ell \ell'^- \ell'^+$ form factors*, Phys. Rev. D **107** (2023) 053006 (cit. on pp. 1, 23).

[9] C. Hanhart, S. Kürten, M. Reboud and D. van Dyk, *Analysis of the $\psi(3770)$ resonance in line with unitarity and analyticity constraints*, Eur. Phys. J. C **84** (2024) 483 (cit. on pp. 1, 49).

[10] M. Beneke and J. Rohrwild, *B meson distribution amplitude from $B \to \gamma \ell \nu$*, Eur. Phys. J. C **71** (2011) 1818 (cit. on pp. 1, 24, 32, 44).

[11] V. M. Braun and A. Khodjamirian, *Soft contribution to $B \to \gamma \ell \nu_\ell$ and the B-meson distribution amplitude*, Phys. Lett. B **718** (2013) 1014 (cit. on p. 1).

[12] M. Beneke, V. M. Braun, Y. Ji and Y.-B. Wei, *Radiative leptonic decay $B \to \gamma \ell \nu_\ell$ with subleading power corrections*, JHEP **07** (2018) 154 (cit. on pp. 1, 24, 25).

[13] M. Beneke, P. Böer, P. Rigatos and K. K. Vos,
QCD factorization of the four-lepton decay $B^- \to \ell\bar{\nu}_\ell \ell^{(\prime)} \bar{\ell}^{(\prime)}$,
Eur. Phys. J. C **81** (2021) 638 (cit. on pp. 2, 24, 29, 32).

[14] M. A. Ivanov and D. Melikhov, *Theoretical analysis of the leptonic decays* $B \to \ell\ell\ell' \nu_{\ell'}$,
Phys. Rev. D **105** (2022) 014028 (cit. on pp. 2, 24, 32).

[15] J. Albrecht, E. Stamou, R. Ziegler and R. Zwicky,
Flavoured axions in the tail of $B_q \to \mu^+\mu^-$ *and* $B \to \gamma^*$ *form factors*, JHEP **09** (2021) 139
(cit. on pp. 2, 24).

[16] C. Wang, Y.-M. Wang and Y.-B. Wei,
QCD factorization for the four-body leptonic B-meson decays, JHEP **02** (2022) 141
(cit. on pp. 2, 24).

[17] M. D. Schwartz, *Quantum Field Theory and the Standard Model*,
Cambridge University Press, 2014, ISBN: 9781107034730 (cit. on pp. 3, 12, 81).

[18] M. E. Peskin and D. V. Schroeder, *An Introduction to quantum field theory*,
Addison-Wesley, 1995, ISBN: 9780201503975 (cit. on pp. 3, 81).

[19] A. Zee, *Quantum field theory in a nutshell*, Princeton University Press, 2003,
ISBN: 9780691140346 (cit. on p. 3).

[20] L. Wolfenstein, *Parametrization of the Kobayashi-Maskawa Matrix*,
Phys. Rev. Lett. **51** (1983) 1945 (cit. on p. 6).

[21] J. Charles et al.,
Current status of the standard model CKM fit and constraints on $\Delta F = 2$ *new physics*,
Phys. Rev. D **91** (2015) 073007 (cit. on pp. 6, 7).

[22] A. V. Manohar and M. B. Wise, *Heavy quark physics*, Cambridge University Press, 2000,
ISBN: 9780521037570 (cit. on p. 7).

[23] S. U. Chung et al., *Partial wave analysis in K matrix formalism*,
Annalen Phys. **4** (1995) 404 (cit. on pp. 9, 55, 65).

[24] G. F. Chew and S. Mandelstam, *Theory of the Low-Energy Pion-Pion Interaction*,
Phys. Rev. **119** (1960) 467 (cit. on pp. 11, 50).

[25] J. H. Reid and N. N. Trofimenkoff, *A generating function for Chew–Mandelstam functions*,
Journal of Mathematical Physics **25** (1984) 3540 (cit. on p. 11).

[26] J. C. Ward, *An Identity in Quantum Electrodynamics*, Phys. Rev. **78** (1950) 182
(cit. on p. 13).

[27] Y. Takahashi and H. Umezawa, *A general treatment of expanding systems*,
Il Nuovo Cimento (1955-1965) **6** (1957) 1324, I. Formulation (cit. on p. 13).

[28] Y. Takahashi and H. Umezawa, *A general treatment of expanding systems*, Il Nuovo
Cimento (1955-1965) **6** (1957) 1382, II. - Application to multiple meson processes
(cit. on p. 13).

[29] W. A. Bardeen and W. K. Tung, *Invariant amplitudes for photon processes*, Phys. Rev. **173** (1968) 1423, [Erratum: Phys. Rev. D **4**, 3229 (1971)] (cit. on pp. 16, 24, 25).

[30] R. Tarrach, *Invariant Amplitudes for Virtual Compton Scattering Off Polarized Nucleons Free from Kinematical Singularities, Zeros and Constraints*, Nuovo Cim. A **28** (1975) 409 (cit. on pp. 16, 24, 25).

[31] G. Colangelo, M. Hoferichter, M. Procura and P. Stoffer, *Dispersion relation for hadronic light-by-light scattering: theoretical foundations*, JHEP **09** (2015) 074 (cit. on p. 16).

[32] G. Colangelo, M. Hoferichter, M. Procura and P. Stoffer, *Dispersion relation for hadronic light-by-light scattering: two-pion contributions*, JHEP **04** (2017) 161 (cit. on p. 16).

[33] A. Bharucha, D. M. Straub and R. Zwicky, *$B \to V\ell^+\ell^-$ in the Standard Model from light-cone sum rules*, JHEP **08** (2016) 098 (cit. on pp. 18, 25, 28, 34–36, 38, 41–43, 46, 47).

[34] G. D'Agostini, *Bayesian Reasoning in Data Analysis*, World Scientific, 2003, ISBN: 9789812383563 (cit. on p. 20).

[35] F. O'Hagan, *Kendall's Advanced Theory of Statistics, Volume 2B: Bayesian Inference*, Wiley, 2003, ISBN: 9780470685693 (cit. on p. 20).

[36] S. Sivia, *Data Analysis: A Bayesian Tutorial*, Oxford University Press, 2006, ISBN: 9780198568315 (cit. on p. 20).

[37] E. T. Jaynes, *Probability Theory: The Logic of Science*, ed. by G. L. Bretthorst, Cambridge University Press, 2003, ISBN: 9780511790423 (cit. on p. 20).

[38] H. Jeffreys, *The Theory of Probability*, Oxford University Press, 1939, ISBN: 9780198503682 (cit. on pp. 21, 59).

[39] T. Janowski, B. Pullin and R. Zwicky, *Charged and neutral $\bar{B}_{u,d,s} \to \gamma$ form factors from light cone sum rules at NLO*, JHEP **12** (2021) 008 (cit. on pp. 24, 32, 38).

[40] D. van Dyk et al., *EOS: a software for flavor physics phenomenology*, Eur. Phys. J. C **82** (2022) 569 (cit. on pp. 24, 47, 50, 58).

[41] Y.-M. Wang, *Factorization and dispersion relations for radiative leptonic B decay*, JHEP **09** (2016) 159 (cit. on p. 24).

[42] G. Colangelo, M. Hoferichter and P. Stoffer, *Two-pion contribution to hadronic vacuum polarization*, JHEP **02** (2019) 006 (cit. on p. 24).

[43] M. Hoferichter, B.-L. Hoid, B. Kubis, S. Leupold and S. Schneider, *Pion-pole contribution to hadronic light-by-light scattering in the anomalous magnetic moment of the muon*, Phys. Rev. Lett. **121** (2018) 112002 (cit. on p. 24).

[44] B.-L. Hoid, M. Hoferichter, B. Kubis, S. Leupold and S. Schneider, *Pion-pole contribution to hadronic light-by-light scattering*, PoS **CD2018** (2019) 052 (cit. on p. 24).

[45] S. Holz et al., *Towards an improved understanding of $\eta \to \gamma^*\gamma^*$*, Eur. Phys. J. C **81** (2021) 1002 (cit. on p. 24).

[46] C. Hanhart et al., *The branching ratio $\omega \to \pi^+\pi^-$ revisited*, Eur. Phys. J. C **77** (2017) 98 (cit. on p. 24).

[47] S. Holz, M. Hoferichter, B.-L. Hoid and B. Kubis, *Precision Evaluation of the η- and η'-Pole Contributions to Hadronic Light-by-Light Scattering in the Anomalous Magnetic Moment of the Muon*, Phys. Rev. Lett. **134** (2025) 171902 (cit. on p. 24).

[48] S. Holz, M. Hoferichter, B.-L. Hoid and B. Kubis, *Dispersion relation for hadronic light-by-light scattering: η and η' poles*, JHEP **04** (2025) 147 (cit. on p. 24).

[49] D. Stamen, D. Hariharan, M. Hoferichter, B. Kubis and P. Stoffer, *Kaon electromagnetic form factors in dispersion theory*, Eur. Phys. J. C **82** (2022) 432 (cit. on p. 24).

[50] P. B. Pal, *Representation-independent manipulations with Dirac matrices and spinors*, 2015, arXiv: physics/0703214 [physics.ed-ph] (cit. on p. 27).

[51] M. A. Ivanov and D. Melikhov, *Theoretical analysis of the leptonic decays $B \to \ell\ell\ell\bar{\nu}_\ell$: Identical leptons in the final state*, Phys. Rev. D **105** (2022) 094038 (cit. on p. 29).

[52] D. Y. Bardin and E. A. Ivanov, *Weak Electromagnetic Decays*, Sov. J. Part. Nucl. **7** (1976) 286 (cit. on p. 32).

[53] J. Bijnens, G. Ecker and J. Gasser, *Radiative semileptonic kaon decays*, Nucl. Phys. B **396** (1993) 81 (cit. on pp. 32, 33).

[54] J. Bijnens, G. Colangelo, G. Ecker and J. Gasser, *Semileptonic kaon decays*, 1994, arXiv: hep-ph/9411311 (cit. on pp. 32, 33).

[55] A. Khodjamirian and D. Wyler, *Counting contact terms in $B \to V\gamma$ decays*, 2001, arXiv: hep-ph/0111249 (cit. on p. 32).

[56] S. Okubo, *Phi meson and unitary symmetry model*, Phys. Lett. **5** (1963) 165 (cit. on p. 34).

[57] G. Zweig, *An SU(3) model for strong interaction symmetry and its breaking. Version 1*, (1964) (cit. on p. 34).

[58] G. Zweig, *An SU(3) model for strong interaction symmetry and its breaking. Version 2*, (1964) 22 (cit. on p. 34).

[59] J. Iizuka, *Systematics and phenomenology of meson family*, Prog. Theor. Phys. Suppl. **37** (1966) 21 (cit. on p. 34).

[60] R. R. Horgan, Z. Liu, S. Meinel and M. Wingate, *Lattice QCD calculation of form factors describing the rare decays $B \to K^* \ell^+ \ell^-$ and $B_s \to \phi \ell^+ \ell^-$*, Phys. Rev. D **89** (2014) 094501 (cit. on p. 35).

[61] S. Navas et al., *Review of particle physics*, Phys. Rev. D **110** (2024) 030001 (cit. on pp. 36, 38, 49, 50, 52, 53, 55, 57, 62, 77).

[62] G. Van Rossum and F. L. Drake, *Python 3 Reference Manual*, CreateSpace, 2009, ISBN: 1441412697 (cit. on p. 42).

[63] T. Kluyver et al., "Jupyter Notebooks – a publishing format for reproducible computational workflows", *Positioning and Power in Academic Publishing: Players, Agents and Agendas*, ed. by F. Loizides and B. Schmidt, IOS Press, 2016, ISBN: 9781614996484 (cit. on p. 42).

[64] P. Virtanen et al., *SciPy 1.0: Fundamental Algorithms for Scientific Computing in Python*, Nature Methods **17** (2020) 261 (cit. on pp. 43, 44).

[65] J. D. Hunter, *Matplotlib: A 2D graphics environment*, Computing in Science & Engineering **9** (2007) 90 (cit. on p. 44).

[66] X.-W. Kang, B. Kubis, C. Hanhart and U.-G. Meißner, *B_{l4} decays and the extraction of $|V_{ub}|$*, Phys. Rev. D **89** (2014) 053015 (cit. on p. 48).

[67] C. Hanhart, A. Kupść, U.-G. Meißner, F. Stollenwerk and A. Wirzba, *Dispersive analysis for $\eta \to \gamma\gamma^*$*, Eur. Phys. J. C **73** (2013) 2668, [Erratum: Eur.Phys.J.C 75, 242 (2015)] (cit. on p. 48).

[68] S. Holz, C. Hanhart, M. Hoferichter and B. Kubis, *A dispersive analysis of $\eta' \to \pi^+\pi^-\gamma$ and $\eta' \to \ell^+\ell^-\gamma$*, Eur. Phys. J. C **82** (2022) 434, [Addendum: Eur.Phys.J.C 82, 1159 (2022)] (cit. on p. 48).

[69] J. Z. Bai et al., *Measurements of the cross-section for $e^+e^- \to$ hadrons at center-of-mass energies from 2 GeV to 5 GeV*, Phys. Rev. Lett. **88** (2002) 101802 (cit. on pp. 49, 51, 56).

[70] M. Ablikim et al., *Measurements of the continuum R(uds) and R values in e^+e^- annihilation in the energy region between 3.650 and 3.872 GeV*, Phys. Rev. Lett. **97** (2006) 262001 (cit. on pp. 49, 51, 56).

[71] M. Ablikim et al., *Measurement of the Cross Section for $e^+e^- \to$ Hadrons at Energies from 2.2324 to 3.6710 GeV*, Phys. Rev. Lett. **128** (2022) 062004 (cit. on pp. 49, 51, 56).

[72] D. van Dyk et al., *EOS version 1.0.11*, 2024, URL: https://doi.org/10.5281/zenodo.10600399 (cit. on pp. 50, 58, 68).

[73] M. Ablikim et al., *Anomalous Line Shape of the Cross Section for $e^+e^- \to$ Hadrons in the Center-of-Mass Energy Region between 3.650 and 3.872 GeV*, Phys. Rev. Lett. **101** (2008) 102004 (cit. on pp. 50, 62).

[74] S. Coito and F. Giacosa, *Line-shape and poles of the $\psi(3770)$*, Nucl. Phys. A **981** (2019) 38 (cit. on pp. 50, 51, 62, 63).

[75] A. G. Shamov and K. Y. Todyshev, *Analysis of BaBar, Belle, BES-II, CLEO and KEDR data on $\psi(3770)$ line shape and determination of the resonance parameters*, Phys. Lett. B **769** (2017) 187 (cit. on pp. 50, 51, 54, 62–64).

[76] O. Bär and U. J. Wiese, *Can one see the number of colors?*, Nucl. Phys. B **609** (2001) 225 (cit. on p. 50).

[77] R. F. Lebed, R. E. Mitchell and E. S. Swanson, *Heavy-Quark QCD Exotica*, Prog. Part. Nucl. Phys. **93** (2017) 143 (cit. on pp. 51, 65).

[78] A. Esposito, A. Pilloni and A. D. Polosa, *Multiquark Resonances*, Phys. Rept. **668** (2017) 1 (cit. on pp. 51, 65).

[79] S. L. Olsen, T. Skwarnicki and D. Zieminska, *Nonstandard heavy mesons and baryons: Experimental evidence*, Rev. Mod. Phys. **90** (2018) 015003 (cit. on pp. 51, 65).

[80] F.-K. Guo et al., *Hadronic molecules*, Rev. Mod. Phys. **90** (2018) 015004 (cit. on pp. 51, 65).

[81] N. Brambilla et al., *The XYZ states: experimental and theoretical status and perspectives*, Phys. Rept. **873** (2020) 1 (cit. on pp. 51, 65).

[82] H.-X. Chen, W. Chen, X. Liu, Y.-R. Liu and S.-L. Zhu, *An updated review of the new hadron states*, Rept. Prog. Phys. **86** (2023) 026201 (cit. on pp. 51, 65).

[83] T. Aoyama et al., *The anomalous magnetic moment of the muon in the Standard Model*, Phys. Rept. **887** (2020) 1 (cit. on p. 51).

[84] R. Aliberti et al., *The anomalous magnetic moment of the muon in the Standard Model: an update*, (2025), arXiv: 2505.21476 [hep-ph] (cit. on p. 51).

[85] T. V. Uglov, Y. S. Kalashnikova, A. V. Nefediev, G. V. Pakhlova and P. N. Pakhlov, *Exclusive open-charm near-threshold cross sections in a coupled-channel approach*, JETP Lett. **105** (2017) 1 (cit. on pp. 51, 54).

[86] N. N. Achasov and G. N. Shestakov, *Electronic width of the $\psi(3770)$ resonance interfering with the background*, Phys. Rev. D **103** (2021) 076017 (cit. on p. 52).

[87] J. M. Blatt and V. F. Weisskopf, *Theoretical nuclear physics*, Springer, 1952, ISBN: 9780471080190 (cit. on p. 52).

[88] L. A. Heuser et al., *From pole parameters to line shapes and branching ratios*, Eur. Phys. J. C **84** (2024) 599 (cit. on p. 54).

[89] S. U. Chung, *Spin formalisms*, 1971, URL: http://dx.doi.org/10.5170/CERN-1971-008 (cit. on p. 55).

[90] The BaBar Collaboration and B. Aubert, *Study of the Exclusive Initial-State-Radiation Production of the $D\bar{D}$ System*, 2008, arXiv: 0710.1371 [hep-ex] (cit. on p. 56).

[91] The Belle Collaboration and G. Pakhlova,
Measurement of the near-threshold $e^+e^- \to D\bar{D}$ cross section using initial-state radiation,
Phys. Rev. D **77** (2008) 011103 (cit. on p. 56).

[92] The CLEO Collaboration and D. Cronin-Hennessy, *Measurement of Charm Production Cross Sections in e^+e^- Annihilation at Energies between 3.97 and 4.26 GeV*,
Phys. Rev. D **80** (2009) 072001 (cit. on p. 56).

[93] The BES Collaboration and M. Ablikim,
Measurements of the cross-sections for $e^+e^- \to$ hadrons at 3.650 GeV, 3.6648 GeV, 3.773 GeV and the branching fraction for $\psi(3770) \to$ non-$D\bar{D}$, Phys. Lett. B **641** (2006) 145 (cit. on p. 56).

[94] A. J. Julin, *Measurement of $D\bar{D}$ Decays from the $\psi(3770)$ Resonance*,
PhD thesis: Minnesota U., 2017, URL: https://hdl.handle.net/11299/199064 (cit. on pp. 56, 63).

[95] N. Hüsken et al., *Poles and poltergeists in $e^+e^- \to D\bar{D}$ data*,
Phys. Rev. D **109** (2024) 114010 (cit. on p. 56).

[96] R. V. Harlander and M. Steinhauser, *rhad: A Program for the evaluation of the hadronic R ratio in the perturbative regime of QCD*, Comput. Phys. Commun. **153** (2003) 244 (cit. on p. 57).

[97] E. Higson, W. Handley, M. Hobson and A. Lasenby, *Dynamic nested sampling: an improved algorithm for parameter estimation and evidence calculation*,
Statistics and Computing **29** (2018) 891 (cit. on p. 59).

[98] S. Koposov et al., *dynesty version 2.0.3*, 2022,
URL: https://doi.org/10.5281/zenodo.7388523 (cit. on p. 59).

[99] J. S. Speagle, *dynesty: a dynamic nested sampling package for estimating Bayesian posteriors and evidences*,
Monthly Notices of the Royal Astronomical Society **493** (2020) 3132 (cit. on p. 59).

[100] S. Weinberg, *The Quantum theory of fields. Vol. 1: Foundations*,
Cambridge University Press, 2005, ISBN: 9780521670531 (cit. on p. 59).

[101] The BES Collaboration and M. Ablikim,
Direct measurements of the cross sections for $e^+e^- \to$ hadrons (non-$D\bar{D}$) in the range from 3.65 GeV to 3.87 GeV and the branching fraction for $\psi(3770) \to$ non-$D\bar{D}$,
Phys. Lett. B **659** (2008) 74 (cit. on pp. 62–64).

[102] The BES Collaboration and M. Ablikim,
Direct measurements of the non-$D\bar{D}$ cross section $\sigma_{\psi(3770)\to\text{non-}D\bar{D}}$ at $E_{cm} = 3.773$ GeV and the branching fraction for $\psi(3770) \to$ non-$D\bar{D}$, Phys. Rev. D **76** (2007) 122002 (cit. on pp. 62–64).

[103] The BES Collaboration and M. Ablikim, *Measurements of the branching fractions for $\psi(3770) \to D^0\bar{D}^0$, D^+D^-, $D\bar{D}$ and the resonance parameters of $\psi(3770)$ and $\psi(2S)$*,
Phys. Rev. Lett. **97** (2006) 121801 (cit. on pp. 62–64).

[104] T. C. Collaboration and D. Besson,
Measurement of $\sigma(e^+e^- \to \psi(3770) \to hadrons)$ at $E_{c.m.} = 3773$ MeV,
Phys. Rev. Lett. **96** (2006) 092002, [Erratum: Phys.Rev.Lett. 104, 159901 (2010)]
(cit. on pp. 62–64).

[105] K. Ishikawa, O. Jinnouchi, K. Nishiwaki and K. Oda,
Wave-packet effects: a solution for isospin anomalies in vector-meson decay,
Eur. Phys. J. C **83** (2023) 978 (cit. on p. 63).

[106] A. Khodjamirian, T. Mannel, A. A. Pivovarov and Y. M. Wang,
Charm-loop effect in $B \to K^{(*)}\ell^+\ell^-$ and $B \to K^*\gamma$, JHEP **09** (2010) 089
(cit. on pp. 63, 64).

[107] A. Khodjamirian, T. Mannel and Y. M. Wang, *$B \to K\ell^+\ell^-$ decay at large hadronic recoil*,
JHEP **02** (2013) 010 (cit. on p. 63).

[108] S. Jäger and J. M. Camalich,
On $B \to V\ell\ell$ at small dilepton invariant mass, power corrections, and new physics,
JHEP **05** (2013) 043 (cit. on p. 63).

[109] M. Ciuchini et al.,
$B \to K^*\ell^+\ell^-$ decays at large recoil in the Standard Model: a theoretical reappraisal,
JHEP **06** (2016) 116 (cit. on p. 63).

[110] C. Bobeth, M. Chrzaszcz, D. van Dyk and J. Virto,
Long-distance effects in $B \to K^*\ell\ell$ from analyticity, Eur. Phys. J. C **78** (2018) 451
(cit. on pp. 63, 64).

[111] N. Gubernari, D. van Dyk and J. Virto,
Non-local matrix elements in $B_{(s)} \to \{K^{(*)}, \phi\}\ell^+\ell^-$, JHEP **02** (2021) 088
(cit. on pp. 63, 64).

[112] N. Gubernari, M. Reboud, D. van Dyk and J. Virto,
Improved theory predictions and global analysis of exclusive $b \to s\mu^+\mu^-$ processes,
JHEP **09** (2022) 133 (cit. on pp. 63, 64).

[113] F. Gross et al., *50 Years of Quantum Chromodynamics*, Eur. Phys. J. C **83** (2023) 1125
(cit. on p. 63).

[114] B. Grinstein and D. Pirjol,
Exclusive rare $B \to K^*\ell^+\ell^-$ decays at low recoil: Controlling the long-distance effects,
Phys. Rev. D **70** (2004) 114005 (cit. on p. 64).

[115] M. Beylich, G. Buchalla and T. Feldmann,
Theory of $B \to K^{(*)}\ell^+\ell^-$ decays at high q^2: OPE and quark-hadron duality,
Eur. Phys. J. C **71** (2011) 1635 (cit. on p. 64).

[116] F. Kruger and L. M. Sehgal,
Lepton polarization in the decays $B \to X(s)\mu^+\mu^-$ and $B \to X(s)\tau^+\tau^-$,
Phys. Lett. B **380** (1996) 199 (cit. on p. 64).

[117] J. Lyon and R. Zwicky,
Resonances gone topsy turvy - the charm of QCD or new physics in $b \to s\ell^+\ell^-$?, (2014),
arXiv: 1406.0566 [hep-ph] (cit. on p. 64).

[118] S. Braß, G. Hiller and I. Nisandzic, *Zooming in on $B \to K^*\ell\ell$ decays at low recoil*,
Eur. Phys. J. C **77** (2017) 16 (cit. on p. 64).

[119] I. Aitchison, *The K-matrix formalism for overlapping resonances*,
Nucl. Phys. A **189** (1972) 417 (cit. on p. 65).

[120] I. J. R. Aitchison, *Unitarity, Analyticity and Crossing Symmetry in Two- and Three-hadron Final State Interactions*, (2015), arXiv: 1507.02697 [hep-ph] (cit. on p. 65).

[121] D. Adams, *The Hitchhiker's Guide to the Galaxy*, Pan Books, 1979 (cit. on p. 103).

List of Figures

List of Tables

Acknowledgements

First of all I would like to thank both my supervisors Danny van Dyk and Bastian Kubis for a lot of opportunities and constant support and encouragement throughout my thesis.

Next, I want to thank my further collaborators Marvin Zanke, Méril Reboud and Christoph Hanhart for fruitful collaborations, nice discussions, much fun and some laughs and facepalms during work.

At this point, I especially want to thank Méril for putting up some pressure and keeping my motivation high with quite some motivational tips, without this support I would've been lost on my way to finish.

Furthermore, I would like to thank my colleagues at TUM, especially, Philip, Peter and Patrick as well as the complete working group van Dyk throughout the years for a nice time in Munich. I also want to thank my close friends Stefan Ropertz and Philip Hauer for hour long discussions during video games and anime sessions. As well as — yet again — Philip Lüghausen, Méril Reboud and Peter van der Griend for discussions during coffee and beers.

Last but not least I want to thank all the friends I met on my way whose names didn't find the direct way into this paragraph. As the last line I want to put my all-time favorite quote:

"so long, and thanks for all the fish." [121]